

HELIUM ISOTOPE AND RARE GAS OCEANOLOGY

HELIUM ISOTOPE AND RARE GAS OCEANOLOGY

By

WILLIAM JOHN JENKINS, B.Sc.

A Thesis

Submitted to the School of Graduate Studies

in Partial Fulfilment of the Requirements

for the Degree

Doctor of Philosophy

McMaster University

May 1974

DOCTOR OF PHILOSOPHY (1974)  
(Physics)

McMASTER UNIVERSITY  
Hamilton, Ontario.

TITLE: Helium Isotope and Rare Gas Oceanology

AUTHOR: William John Jenkins, B.Sc. (McMaster University)

SUPERVISOR: Professor W. B. Clarke

NUMBER OF PAGES: (xiv), 171

## ABSTRACT

The isotopic composition and concentration of the dissolved helium have been measured in over 250 samples of Atlantic and Pacific seawater. The helium isotope ratios were measured using a double collection "static" mass spectrometer specifically designed and constructed for this purpose. The helium and neon contents of 118 of these samples were determined using the isotope dilution technique, and the helium contents of the remaining samples were determined by peak-height comparison with standard air aliquots. Krypton and xenon concentrations were measured by isotope dilution for the Pacific samples.

Two sources of excess nonatmospheric  $^3\text{He}$  are discerned in the Atlantic Ocean: a primordial component and a component produced by in situ decay of bomb-produced tritium. The former component occurs in three distinct features; two emanating from the south at 1000 m and greater than 4000 m depths, and one emanating from the north at about 3000 m depth. The spatial properties of these features are studied in the framework of simple models. The latter, or "tritiogenic" component is coupled with tritium concentrations measured by others to obtain Tritium-helium Ages, the characteristics of which are compared with

hydrographic features. For example, the spreading velocity of the Mediterranean Water is determined to be  $\approx 1.5 \text{ cm sec}^{-1}$  in the North-Western Atlantic.

The helium and neon concentrations measured in Atlantic Waters indicate that significant variations occur for helium contents, both as a function of depth and latitude. The Antarctic Bottom Water appears to be a source of excess helium.

In the Pacific, the distribution of excess  $^3\text{He}$  is shown to be consistent with injection of primordial  $^3\text{He}$  into the Deep and Bottom Waters from the East Pacific Rise. The characteristic mid-depth maximum seen in the helium isotope ratio anomaly profiles is shown to be a circulatory feature. Upper and lower limits on the amount of excess nonatmospheric  $^4\text{He}$  are set at 5.5 and 2.6% respectively. Application of a simple one-dimensional diffusive-advective model indicate an upward flux of  $6 \pm 2$  and  $1.1 \pm 0.5 \times 10^6$  atoms/cm<sup>2</sup>/sec for  $^3\text{He}$  and  $^4\text{He}$  respectively.

Pacific seawater is, on the average, 16 and 31% supersaturated in krypton and xenon respectively. Although there is no known process that is capable of such enrichments, the spatial distribution of the krypton and xenon concentrations indicate that a significant amount of the enrichment occurs in situ in Pacific Deep Waters.

## ACKNOWLEDGEMENTS

I wish to thank Dr. W. B. Clarke for his patience, guidance and advice over the past years, and for the enormous amount of time and effort he has given to this research. Many hours of discussions with him have profoundly affected my views of scientific research, and I have learned much from his expertise in the laboratory. I would also like to thank Dr. C. E. Rees and Mr. A. Teitsma for many interesting discussions and Drs. H. G. Thode, T. J. Kennett and W. V. Prestwich for valuable suggestions.

I am indebted to Professor H. Craig of Scripps Institution of Oceanography and Professor P. J. Wangersky of Dalhousie University for procuring the samples, and to Dr. H. G. Östlund for making this tritium data available. Special thanks are due to Mr. E. M. Beaver, whose technical advice and assistance proved invaluable, and to Miss Erie Long for the arduous task of typing this manuscript.

Most of all, I would like to express my gratitude to my wife for her patience, encouragement and stoicism during this endeavour. I thank my parents for their kindness and generosity and especially my father, who kindled my interest in science.

This work was made possible through grants from the National Research Council and assistantships and scholarships from McMaster University.

## TABLE OF CONTENTS

CHAPTER		PAGE
1	<u>INTRODUCTION</u>	1
	A. Factors Affecting Rare Gas Concentrations	3
	B. Previous Measurements	8
	C. Helium Isotope Measurements	12
	D. Tritium in the Oceans and Tritium-Helium Dating	14
	E. The Present Approach	15
2	<u>EXPERIMENTAL TECHNIQUES</u>	16
	A. Introduction	16
	B. Sample Collection and Storage	16
	C. Extraction of the Rare Gases from Sea Water	17
	(i) The basic procedure	17
	(ii) The GEOSECS II extractions	18
	(iii) The HUDSON 70 extractions	20
	(iv) The GEOSECS Leg I and Leg III extractions	21
	(v) Blanks	22

TABLE OF CONTENTS - continued

CHAPTER		PAGE
2	D. Helium Isotope Measurements	26
	(i) The GEOSECS II analyses	26
	(ii) The branch-tube mass spectrometer	26
	(iii) Sample measurement using the branch-tube spectrometer	29
	E. Spike Preparations	30
	(i) Helium and neon	30
	(ii) Krypton and xenon standards	32
	(iii) Volume calibrations	33
	(iv) Spike size calculations and uncertainties	33
	F. Isotope Dilution Mass Spectrometry	36
	(i) Helium and neon	36
	(ii) Krypton and xenon	37
3	<u>THE ATLANTIC: RESULTS AND DISCUSSION</u>	40
	A. Results	40
	B. Discussion	55
	(i) Helium and neon saturation anomalies	55
	(ii) The distribution of $\delta(^3\text{He})$	64
	(iii) Tritium-helium dating: concepts	84
	(iv) Tritium-helium age dating: results	89
	(v) Summary of Atlantic results	100

TABLE OF CONTENTS - continued

CHAPTER		PAGE
4	<u>THE PACIFIC: RESULTS AND DISCUSSION</u>	103
	A. Results	103
	B. Discussion	105
	1. The Data in Relation to Hydrographic Structure	110
	(i) Station 227: 62.9°S × 150.0°W	110
	(ii) Station 230: 49.9°S × 150.0°W	112
	(iii) Station 234: 30.0°S × 150.0°W	115
	(iv) Station 243: 16.0°N × 150.0°W	119
	(v) Station 247: 42.8°N × 149.9°W	122
	2. General Trends	124
	(i) Krypton and xenon concentrations	124
	(ii) The saturation anomalies of helium and neon	125
	(iii) Helium isotope ratio anomalies and primordial helium	135
	(iv) The helium flux	142
APPENDIX		
1	<u>VARIOUS MATHEMATICAL DERIVATIONS</u>	146
	A. Two-Dimensional Fickian Diffusion from a Point Source in an Anisotropic Medium	146
	B. The Flux Balance Model	147
	C. Tritium-Helium Age Calculation	148

TABLE OF CONTENTS - continued

APPENDIX		PAGE
1	D. The One-Dimensional Advective Diffusive Model	149
	E. Derivation of the Non-Atmospheric <sup>3</sup> He Component	152
2	<u>GLOSSARY</u>	156
	A. Symbols and Terms	156
	B. Acronyms	159
	<u>REFERENCES</u>	161

LIST OF TABLES

TABLE		PAGE
1	MECHANISMS AFFECTING RARE GAS SATURATION ANOMALIES	5
2	PUBLISHED RARE GAS CONCENTRATIONS	9
3	EXTRACTION BLANK RESULTS	25
4	ABSOLUTE AND RELATIVE MEASUREMENT UNCERTAINTIES	35
5	KRYPTON AND XENON ISOTOPES	39
6	HELIUM AND TRITIUM-HELIUM AGE DATA FOR ATLANTIC STATIONS	44
7	HELIUM DATA FOR ATLANTIC STATIONS	47
8	ATLANTIC NEON DATA	50
9	$\Delta\text{He}$ AVERAGES IN THE ATLANTIC OCEAN	56
10	AVERAGE SCATTER OF PEAK-HEIGHT VALUES OVER DIFFERENT DEPTH RANGES	57
11	AVERAGE SCATTER OF ISOTOPE DILUTION VALUES OVER DIFFERENT DEPTH RANGES	58
12	$\Delta\text{Ne}$ AVERAGES IN THE ATLANTIC OCEAN	61
13	$\Delta'\text{He}$ AVERAGES IN THE ATLANTIC OCEAN	63
14	D/v CALCULATIONS FOR THE LDW	73

LIST OF TABLES - continued

TABLE		PAGE
15	INTEGRATED EXCESS $^3\text{He}$ IN THE SOUTH ATLANTIC	77
16	D/v CALCULATIONS FOR SOUTH ATLANTIC INTERMEDIATE WATERS	82
17	AN ILLUSTRATION OF T-He AGE MIXING	87
18	THE PACIFIC DATA	104
19	PACIFIC ANOMALY TRENDS	128
20	$\Delta\text{Ne}$ COMPARISONS	138
21	$\Delta(^4\text{He})$ AND $\Delta(^3\text{He})$ AVERAGES FROM THE DATA OF BEG (1971)	140
22	ONE-DIMENSIONAL ADVECTIVE-DIFFUSIVE MODEL PARAMETERS	143

LIST OF FIGURES

FIGURE		PAGE
1	The extraction line used for the GEOSECS-II samples	19
2	Extraction line for the GEOSECS Leg I series	23
3	Leg III modifications to the GEOSECS extraction line	24
4	The branch-tube mass spectrometer and sample inlet system	27
5	The spike preparation line	31
6	The Kr-Xe sample line	38
7	Station positions in the Atlantic	41
8	Helium saturation anomaly profiles for four North Atlantic stations	52
9	Neon saturation anomaly profiles for four North Atlantic stations	53
10	"Excess" helium anomaly profiles for four North Atlantic stations	54
11	Latitudinal distribution of $\Delta\text{He}$ in the NADW	60
12a	Helium isotope ratio anomaly profiles in the Atlantic	66

LIST OF FIGURES - continued

FIGURE		PAGE
12b	Helium isotope ratio anomaly profiles in the Atlantic	67
12c	Helium isotope ratio anomaly profiles in the Atlantic	68
13	A comparison of experimental results with calculated curves for the 3 km maximum in the Atlantic	74
14	The vertical distribution of $\delta(^3\text{He})$ in the South Atlantic	80
15a	Tritium-helium age as a function of $\delta'(^3\text{He})$ and Tritium	88
15b	The effect of mixing on the tritium-helium age	88
16a	Tritium-helium age profiles in the North Atlantic	90
16b	Tritium-helium age profile in the North Atlantic	91
17	Helium isotope ratio anomaly profiles along 150°W	106
18	Helium and neon saturation anomaly profiles along 150°W	107

LIST OF FIGURES - continued

FIGURE		PAGE
19	Krypton and xenon concentration profiles along 150°W	108
20	Excess helium profiles along 150°W	109
21	$\delta(^3\text{He})$ vs salinity for Deep Pacific Waters	117
22	$\Delta\text{He}$ vs salinity for Pacific Bottom Waters	130
23	Pacific Deep and Bottom Water $\Delta(^3\text{He})$	131

## CHAPTER 1

### INTRODUCTION

In a very general and qualitative way, the circulation of the oceans is understood. It consists of an almost linear superposition of two circulations: that induced by wind stress at the sea surface and that driven by density differences. The ultimate source of energy for both motions is insolation, but the scales and mechanics of these circulations differ considerably.

Wind induced circulations are generally restricted to the top few tens of meters of the sea, and have characteristic time scales from a few weeks to a few years. Examples of this type of circulation include the Gulf Stream in the Atlantic, the Kuroshio in the Pacific and the Equatorial Current Systems in both oceans. These currents are rapid (of the order of  $1 \text{ m sec}^{-1}$ ) and are amenable to direct measurement, for example by ship drift and GEK\*.

The density driven or "thermohaline" circulations involve the entire depths of the oceans, are mainly meridional, and have characteristic time scales of centuries. The predominant mode of motion consists of sinking in polar

---

\* geomagnetic electro-kinetrograph

regions balanced by general non-localized upwelling in the interior. These motions are difficult to measure directly due to inaccessibility and low velocities (of the order of  $1 \text{ cm sec}^{-1}$ ). Consequently virtually all knowledge of these circulations derive from the study of distributions of properties.

Until recently, only temperature, salinity and dissolved oxygen have been systematically measured; but oceanographic expeditions of the past decade have extended measurements to include other properties, such as dissolved silica, nutrients and  $^{14}\text{C}$ .

Recently dissolved rare gas contents have been determined, largely with Pacific Ocean water samples. Rare gas concentration measurements appear promising because the rare gases are conservative tracers: once out of contact with the atmosphere, their respective concentrations are altered only by mixing and turbulent exchange. Because of the importance of oxygen as an indicator of bio-activity, it may prove profitable to use the rare gas concentrations to determine the nature and extent of the physical processes that partly determine the oxygen distribution. As well, a study of the rare gas concentrations may lead to a quantitative understanding of the air-sea interface processes that fix dissolved gas concentrations.

Helium is of particular interest since it is not strictly conserved in the deep waters. It has been

established that there is a flux of helium through the ocean floor (e.g., Bieri et al., 1964, 1966, 1967, 1968; Craig and Weiss, 1971) presumably due to radioactive decay of uranium and thorium in the crust and upper mantle. The determination of the magnitude and geographical distribution of this flux has bearing on geophysical as well as oceanographic considerations. Unfortunately, a large fraction of the excess (above solubility) helium is of atmospheric origin (Craig and Weiss, 1971). It is therefore necessary that the concentrations of the other rare gases be determined to establish precisely the atmospheric component of the excess helium.

#### A. Factors Affecting Rare Gas Concentrations

The processes that affect rare gas concentrations, or rather their saturation anomalies, defined by

$$\Delta(\%) = (C/C^*(\theta, S) - 1) \times 100 \quad (1)$$

have been discussed elsewhere (e.g., Benson, 1965; Weiss, 1970a; Bieri, 1971; Craig and Weiss, 1971). In Eq. (1),  $C$  is the measured gas concentration and  $C^*(\theta, S)$  is the solubility equilibrium concentration at the potential

temperature<sup>†</sup> ( $\theta$ ) and salinity ( $S$ ) of the sample. The factors affecting the saturation anomalies are described below and are summarized in Table 1. These five processes fall into two categories: those that occur at the sea surface and those that occur after the water "parcel" has left the sea surface. As can be seen in Table 1, the former type of process tends to affect the less soluble gases (He and Ne) most, while the latter largely affects the more soluble gases.

(1) Ambient atmospheric pressure variations result in Henry's Law variations in all rare gas concentrations. The saturation anomalies generated will be the same for all gases.

(2) Air injection occurs when wave action produces and drives down bubbles (Medwin, 1970; Kanwisher, 1963). Most of the bubbles, due to rapidly increasing hydrostatic pressure with depth, are forced to totally dissolve, injecting gases into the dissolved phase according to their atmospheric abundances. This results in enrichment of the less soluble gases (He and Ne) relative to the more soluble ones.

---

<sup>†</sup> the temperature of a water parcel that has been raised adiabatically to the surface, hereafter referred to as the "temperature".

TABLE 1  
MECHANISMS AFFECTING RARE GAS SATURATION ANOMALIES

Mechanism*		Saturation Anomalies (in %)†				
		$\Delta\text{He}$	$\Delta\text{Ne}$	$\Delta\text{Ar}$	$\Delta\text{Kr}$	$\Delta\text{Xe}$
1. Atmospheric pressure variations	max	0.8	0.8	0.8	0.8	0.8
	min	-2.3	-2.3	-2.3	-2.3	-2.3
2. Air injection of 1 cc air/Kg	at 20°C	14.0	12.0	3.8	2.2	1.3
	at 2°C	13.3	10.5	2.6	1.5	0.8
4. A temperature change of 2°C	at 20°C	0.4	1.3	3.6	5.1	5.6
	at 2°C	0.9	1.8	5.0	5.3	7.6
5. Mixing (50%-50%) between water types	0°C and 20°C	0.8	1.0	4.4	5.0	5.5
	0°C and 4°C	0.1	0.1	0.2	0.6	0.8

\* assuming a salinity of 35 % in all cases.

† calculations using the atmospheric abundances of Glueckauf, 1951; the solubilities of Weiss (1971) for He and Ne, Weiss (1970) for Ar and König (1963) for Kr and Xe.

(3) Diffusive transfer of gases between the atmosphere and the sea will tend to differentiate between gases. This transfer occurs when dis-equilibrium arises due to either of the above processes. Since molecular diffusion across the laminar boundary layer at the air-sea interface is the rate controlling process (Kanwisher, 1963), and since the molecular diffusivities of the rare gases vary over a factor of three (Boerboom and Kleyn, 1969) some form of discrimination may occur. While it is not possible to estimate quantitatively the extent of this discrimination, it is of interest to note that this process tends to enrich the more soluble (lower diffusivity) gases, a discrimination opposite in a sense to that of air injection. It is possible to envisage the subsurface saturation anomaly patterns as generated by a dynamic balance between this mechanism and air injection.

(4) Temperature changes in a water parcel after it has left the surface will result in a different estimate of the solubility concentration. This generates an apparent saturation anomaly which, if the temperature change is small (a few degrees or less), may be expressed as

$$\Delta(\%) = - 100 \frac{\partial \ln C^*}{\partial \theta} \Delta \theta \quad (2)$$

where  $\Delta \theta$  is the temperature change. Since the solubilities of the more soluble gases (Kr and Xe) show the strongest

temperature dependence, these gases will be affected the most.

(5) Mixing between water types of differing temperature and salinity will result in supersaturation. This arises from the positive curvature of the solubility-temperature relationship. The magnitude of these supersaturations depends on the strength of the curvature (greatest for the more soluble gases) and on the temperature difference between the two water types.

With the exception of mechanism (3), some quantitative examples of the above processes are given in Table 1.

Not a great deal has been accomplished in the quantitative empirical investigation of these processes, however, due to a lack of reliable and precise measurements, and due to the lack of accurate solubility data for Kr and Xe. Some attempts have been made, most notably by Craig and Weiss (1971) and Bieri (1971), to construct a model that accounts for some of the above processes (mechanisms (1), (2), and (4)). Each component of the model (corresponding to a mechanism) requires the simultaneous determination of the saturation anomaly of a gas other than helium. Thus the model of Craig and Weiss would require the simultaneous measurement of three gases in addition to helium. To account for all the mechanisms mentioned above a model with five components would be needed, and simultaneous determination

of five concentrations other than helium would be required. This would prove awkward in light of the fact that there are only four stable rare gases other than He.

#### B. Previous Measurements

The concentrations of rare gases in seawater were first reported by König et al. (1964) for He, Ne and Ar, and by Hintenberger et al. (1964) for Kr and Xe. The former group used microgasonometric techniques while the latter used isotope dilution mass spectrometry. Several investigators (see Table 2) have since reported measurements of some or all the dissolved rare gases, often with conflicting results. These results are summarized in Table 2 in the form of saturation anomalies, relative to the solubility data of Weiss (1971) for He and Ne, Weiss (1970b) for Ar, and König (1963) for Kr and Xe.

Recent He and Ne determinations (Bieri et al., 1966, 1968; Bieri and Koide, 1972; Beg, 1971) are in qualitative agreement. In fact the higher  $\Delta\text{He}$  values of Beg (1971) are due to the biasing of sampling toward the deep water, where  $\Delta\text{He}$  values are systematically larger. The most recent determinations (Bieri and Koide, 1972; Beg, 1971) reveal that He is generally supersaturated by  $\sim 11\%$  in Pacific deep water, while Ne is supersaturated by  $\sim 6.5\%$ . The only Atlantic

TABLE 2

## PUBLISHED RARE GAS CONCENTRATIONS

Year Reported	Group	Gas	Number Samples	Saturation Anomalies*			Techniques
				Min	Max	Mean	
1964	König et al.	He	11	-1	10	6	Microgasonometric
		Ne		-6	1	-1	
		Ar		-7	-1	-4	
1964	Hintenberger et al.	Kr	6	5	26	14	Isotope dilution
		Xe	8	0	48	24	
1964	Mazor et al.	Ne	3	1	25	9	Isotope dilution
		Ar		-23	3	-10	
		Kr		-13	-2	-7	
		Xe		-12	8	0	
1964	Bieri et al.	He	7	-22	24	1	Peak Height Mass Spectrometry
		Ne		-41	7	-21	
		Ar		-58	8	-22	
		Kr		-66	11	-24	
		Xe		-65	13	-20	
1966	Bieri et al.	He	80	-4	27	10	Peak Height Mass Spectrometry
		Ne		-7	13	7	
		Ar		-10	15	3	
		Kr		-1	20	13	
1967	Craig et al.	Ne	38	3	16	7	Isotope dilution Gas chromatography
		Ar		-5	1	-1	

TABLE 2 - continued

Year Reported	Group	Gas	Number Samples	Saturation Anomalies*			Techniques
				Min	Max	Mean	
1968	Bieri et al.	He	142	1	10	5	Isotope dilution
		Ne		-3	8	3	
		Ar		-5	6	0	
		Kr		-1	18	8	
1971	Beg	He	54	6	26	12	Isotope dilution
		Ne		1	15	5	
1972	Bieri and Koide	He	83	4	15	8	Isotope dilution
		Ne		4	12	6	
		Ar		0	14	3	
		Kr		4	21	10	

\* See text. For He, Ne and Ar relative to the solubility data of Weiss (1970, 1971), and for Kr and Xe relative to the solubility data of König (1963).

measurements in the literature (Bieri et al., 1968) show an average supersaturation of  $\sim 6\%$  for both gases. At least part of the  $\Delta\text{He}$  difference between the two oceans is attributable to radiogenic  $^4\text{He}$ .

There have been only three reported determinations of seawater Xe. Hintenberger et al. (1964) reported supersaturations of Xe as large as 48%, with an average supersaturation of 24%. Corresponding values for Kr were 26% and 14% respectively. For comparison they determined the Xe and Kr contents of artificially equilibrated samples, the results of which agreed qualitatively with solubility data. Mazor et al. (1964) criticized these results, and on the basis of three concentration measurements, found undersaturation for Kr averaging  $-7\%$ , and  $\sim 0\%$  supersaturation for Xe.

In the same year Bieri et al. (1964) reported grossly undersaturated samples. It was later admitted (Bieri et al., 1966) that the apparent undersaturation of the rare gases was likely due to incomplete extraction. The Kr measurements of Bieri since 1966 (Bieri et al., 1966, 1968; Bieri and Koide, 1972) are essentially in agreement with those of Hintenberger et al..

### C. Helium Isotope Measurements

Another approach to the problem of determining the non-atmospheric excess  $^4\text{He}$  would be to measure the helium isotope ratio, or rather the helium isotope ratio anomaly, defined by

$$\delta(^3\text{He}) \equiv [ (^3\text{He}/^4\text{He})_{\text{sample}} / (^3\text{He}/^4\text{He})_{\text{air}} - 1 ] \times 100\% \quad (3)$$

Since there is an isotope fractionation effect in solubility ( $^4\text{He}$  is slightly more soluble than  $^3\text{He}$ ), the quantity of interest is the helium isotope ratio anomaly relative to air equilibrated water, given by

$$\delta'(^3\text{He}) \equiv \delta(^3\text{He}) + (1-\alpha) \times 100\% \quad (4)$$

where  $\alpha$  is the fractionation factor ( $\sim 0.987$ ) as determined by Weiss (1970c).

Thus the presence of radiogenic  $^4\text{He}$  would be indicated by negative values of  $\delta'(^3\text{He})$ . It was with this in mind that Clarke et al. (1969) measured the dissolved helium isotopes in South Pacific seawater. Despite expectations, they found consistently positive values of  $\delta'(^3\text{He})$ , ranging from  $\sim 0$  to  $23 \pm 2\%$ , with the largest enrichments occurring at mid-depths. They interpreted these deviations as resulting from a flux of primordial  $^3\text{He}$  from

rise crests (Clarke et al., 1969). Fairhall (1969) criticized this interpretation, claiming that the excess  $^3\text{He}$  could be explained by in situ decay of cosmogenic tritium; but Craig and Clarke (1970) showed Fairhall's arguments to be inconsistent with existing knowledge of the pre-nuclear era tritium budget. They further calculated the flux of  $^3\text{He}$  into the Pacific to be  $6 \pm 2$  atoms  $\text{cm}^{-2} \text{sec}^{-1}$ .

Further measurements were performed in this laboratory on Pacific samples (Clarke et al., 1970; Beg, 1971), showing the mid-depth maximum to be a general feature, and showing the largest enrichments near the East Pacific Rise. This supported the original interpretation of the primordial origin of the excess  $^3\text{He}$  since the East Pacific Rise area is typified by high heat flow and shallow seismicity, characteristics of upwelling mantle material. In addition, samples taken in the South Atlantic were also analyzed (Jenkins et al., 1972) showing the South Atlantic to have an excess  $^3\text{He}$  component four times smaller than the Pacific, a result roughly consistent with present knowledge of fluid residence times in the two oceans.

#### D. Tritium in the Oceans and Tritium-Helium Dating

Prior to 1954, the global inventory of tritium was not in excess of 1.5 Kg (Craig and Lal, 1961); but due to hydrogen bomb testing by the US and USSR, about 200 Kg was added, predominantly to the stratosphere (Eriksson, 1965). This tritium in the form of HTO is being transferred to the surface layers of the ocean by means of precipitation and river discharge. Consequently tritium levels have increased markedly in the oceanic mixed layer since the major bomb-tests (Dockins et al., 1967; Rooth and Östlund, 1972).

To be of maximum use a radioactive tracer should have a half-life comparable to about one sixth the characteristic time scale of the system being studied. With its half-life of 12.26 y, tritium has great potential as a radioactive tracer for the study of the advective-diffusive structure of the oceanic thermocline. Difficulties are encountered, however, since the injection of tritium into the atmosphere has been pulse-like. Despite this, some interesting results have been obtained (e.g., Rooth and Östlund, 1972)

Simultaneous measurement of the daughter product  $^3\text{He}$  greatly increases the temporal sensitivity of tritium, and provides sufficient information for determining the initial tritium distribution. For example, if a sample containing 10 T.U. (1 T.U. =  $1 \text{ T}/10^{18} \text{ H}$ ) were to be isolated for two months, an enrichment of 0.4% would occur for  $^3\text{He}$ , a

measurable quantity with present techniques. This, however, would result in only a 0.9% decrease in the tritium content, smaller than present precision, and certainly smaller than the uncertainty induced by the irregular injection mode of the tritium. Thus it can be seen that Tritium-Helium Dating holds great promise for oceanic thermocline and circulation studies.

#### E. The Present Approach

With greatly increased precision in helium isotope determinations, and measurement of a large suite of samples (over 250 samples) it is felt that much can be learned about the circulation of the Atlantic and Pacific Oceans. Coupled with tritium measurements, the North Atlantic helium data may be used to calculate "Tritium-Helium Ages", and thus spreading velocities and residence times may be estimated for some water masses.

In addition, careful and precise determinations of He, Ne, Kr, and Xe would serve to settle some of the unanswered questions about the distribution, variability and magnitude of rare gas concentrations in the oceans.

## CHAPTER 2

### EXPERIMENTAL TECHNIQUES

#### A. Introduction

A number of samples of sea water were taken at several "stations" (locations) in the Pacific and North Atlantic Oceans. The shipboard sampling method has been described by Clarke et al. (1969). The dissolved rare gases were extracted from the sea water samples in an all glass, high vacuum apparatus, and the gases purified and separated into different fractions, each fraction being stored in a glass sample tube.

A portion of the helium and neon was analyzed for the helium isotopic ratio while the remainder was analyzed by isotope dilution for total contents. For the Pacific samples, a third fraction consisting of all the krypton and xenon was also analyzed by isotope dilution.

#### B. Sample Collection and Storage

The GEOSECS sample vessels were filled from thirty-litre Niskin bottles using the simple gravity feed method described by Clarke et al. (1969). The HUDSON samples were taken in the same manner, but from four-litre Nansen bottles.

The transfer took place within a few minutes of the bottle's arrival at the sea surface.

The sample vessels used for the GEOSECS II and the HUDSON 70 series were 325 ml stainless steel cylinders with Whitey forged body valves on either end tightened to a torque of 60 inch-pounds. The remaining samples were stored in a length ( $\sim$  36 in.) of soft copper refrigeration tubing (3/8 in. O.D.  $\times$  1/4 in. I.D.) sealed at either end with a steel pinch clamp. This, as discussed by Weiss (1968), proved to be an ultra-high vacuum seal. A short length of tubing ( $\sim$  2 in.) protruded beyond the clamps to allow coupling to a vacuum system.

### C. Extraction of the Rare Gases from Sea Water

The four series of samples (GEOSECS II, HUDSON 70, GEOSECS Leg I and GEOSECS Leg III) were processed at different times and with different objectives in mind. Consequently the techniques vary somewhat. Quantitative (i.e., better than 99.9%) extraction of helium and neon was achieved for all samples whereas only the HUDSON 70 samples were processed to obtain krypton and xenon as well.

#### (i) The basic procedure

The sample vessel was coupled to an all glass, high

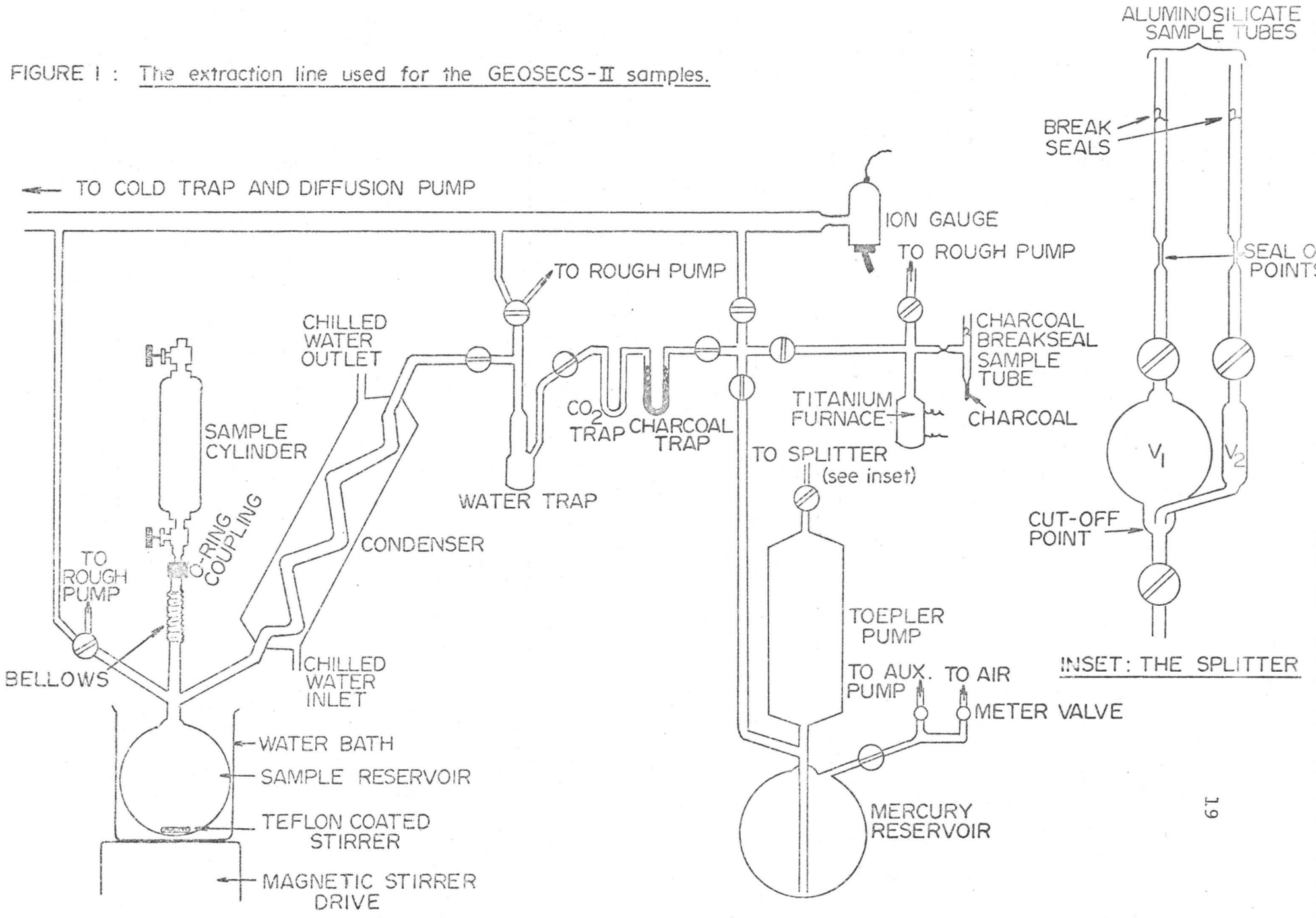
vacuum line (see Fig. 1) by means of an O-ring seal. The water was admitted to the reservoir where it was allowed to degas. Water vapour was trapped while the evolved gases, except for helium and neon, were collected in the two following traps. The helium and neon were transferred to a splitter and subsequently, to aluminosilicate sample tubes. Aluminosilicate glass was used because of its low helium permeability (see Norton 1959, Altimose 1961).

Following removal of the helium-neon fractions, and after sufficient time had elapsed for quantitative degassing of the krypton and xenon, the evolved gases were transferred from the U-traps to another section of the vacuum line where they were purified over hot ( $\sim 800^{\circ}\text{C}$ ) titanium and condensed in a sample tube on activated charcoal. Further details are given by Beg (1971).

(ii) The GEOSECS II extractions

The samples were processed on the vacuum line shown in Fig. 1. Typical extraction times were 45 and 90 minutes for the helium-neon and argon fractions respectively. The helium-neon fraction was divided in a calibrated splitter (see inset, Fig. 1) by raising mercury past a cut-off point, isolating two volumes in the ratio 13.83:1.00. The larger split was used for helium isotope analysis and the smaller split for isotope dilution measurements.

FIGURE 1 : The extraction line used for the GEOSECS-II samples.



About 50 mg of  $P_2O_5$  was added to the reservoir prior to sample admission. Upon mixing, the sample released large amounts of  $CO_2$  due to the acidification. It was expected that the bubbling action would aid degassing. Further tests showed that the addition of  $P_2O_5$  was ineffective, so the method was discontinued after this series.

(iii) The HUDSON 70 extractions

For this series, a short ( $\sim 2$  in.) length of .5 mm I.D. capillary tubing was included in the extraction line between the condenser and the water trap. Prior to the series, the properties of this "capillary pump" (the capillary plus the water trap) were investigated: both on a specially constructed line connected to a mass spectrometer and on the extraction line itself by means of efficiency blanks. The results showed the pump's advantages to be threefold:

- 1) Because of the restricted inner diameter, the pump reduced the rate of water vapour transfer to the water trap, thereby decreasing the rate of buildup of ice in the trap.
- 2) The water vapour that did pass through was driven by a pressure differential of about 10 mm Hg. The flow served to sweep the evolved gases through the capillary, pumping continuously on the sample. A toepler pump, on the other

hand, pumps on the sample only a fraction of the time.

- 3) There was no measurable backstreaming, meaning that the volume that the toepler equilibrated with did not include the sample reservoir. Thus the toepler efficiency was enhanced, and the number of toepler cycles necessary during extraction was reduced correspondingly.

Sixty minutes was allowed for extraction of the helium-neon samples, while the krypton and xenon was extracted for 3 1/2 hours.

(iv) The GEOSECS Leg I and Leg III extractions

A new line was constructed for the GEOSECS extractions (fig. 2). Because the samples were much smaller than the previous series (40 g compared to 325 g) it was necessary to reduce the blank as much as possible. This was accomplished by constructing the line entirely (with the exception of the pyrex stopcocks) of aluminosilicate glass.

The new line did not include a condenser because the capillary effectively reduced water vapour transfer. In addition, since it was decided to measure only the helium and neon, no charcoal trap was necessary. Extraction times were typically 15 minutes, and the resultant helium blank about 0.2% of sample size.

For the Leg I extractions the calibrated splitter pictured in Fig. 2 (inset) was used to split the helium-neon samples in a ratio of 0.5683:0.4317. A different splitter (Fig. 3(b)) was used for the Leg III extractions, giving a split ratio of 0.5158:0.4842 for that series.

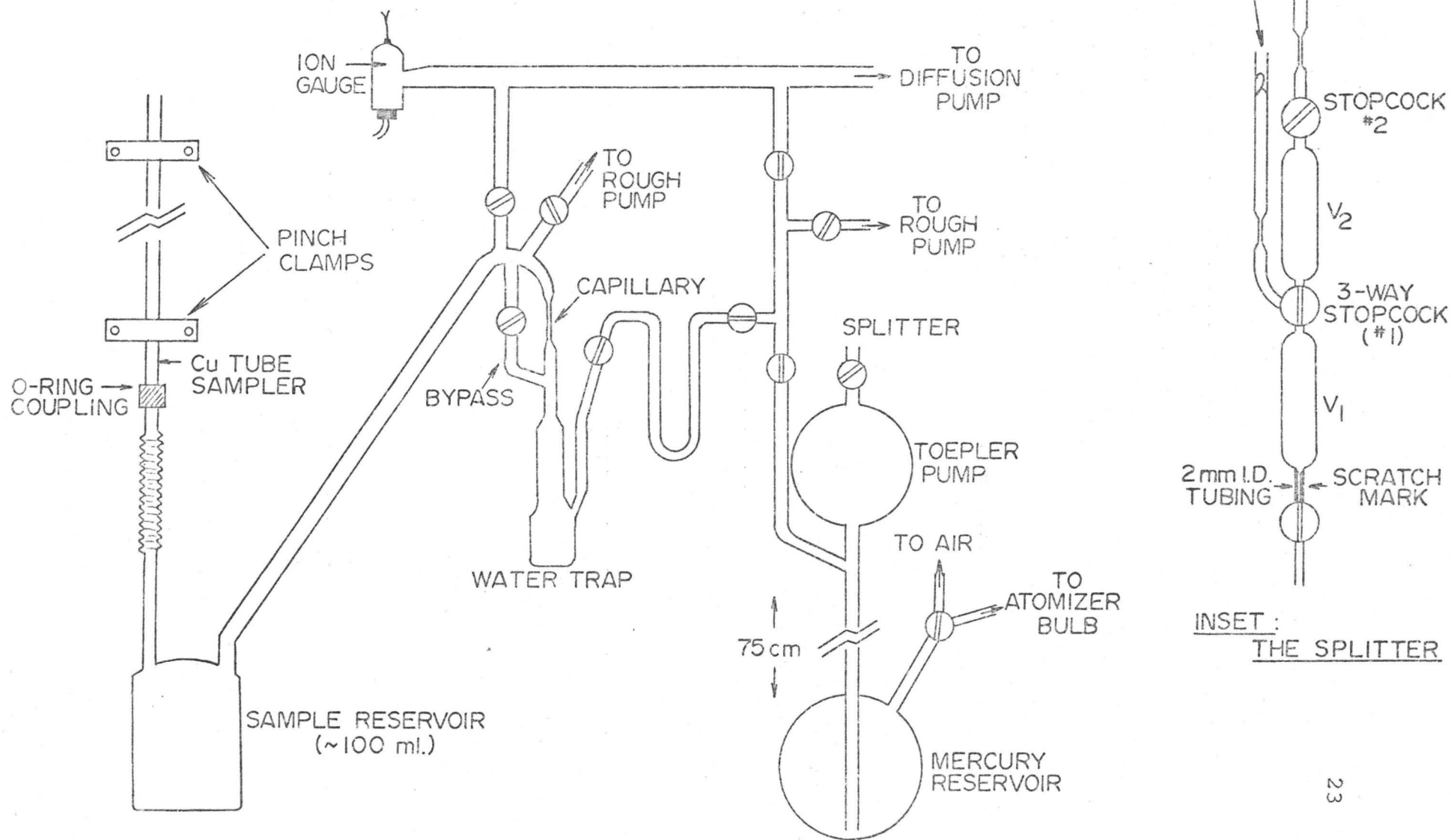
For the Leg III series, the line was further altered to permit simultaneous extraction of helium and neon and degassing of the water for subsequent tritium measurement. A reservoir cum sample vessel (Fig. 3(a)) was attached to the line with an O-ring coupling. Upon completion of the extraction the water sample was "saved" in the degassed state by flame sealing the constriction.

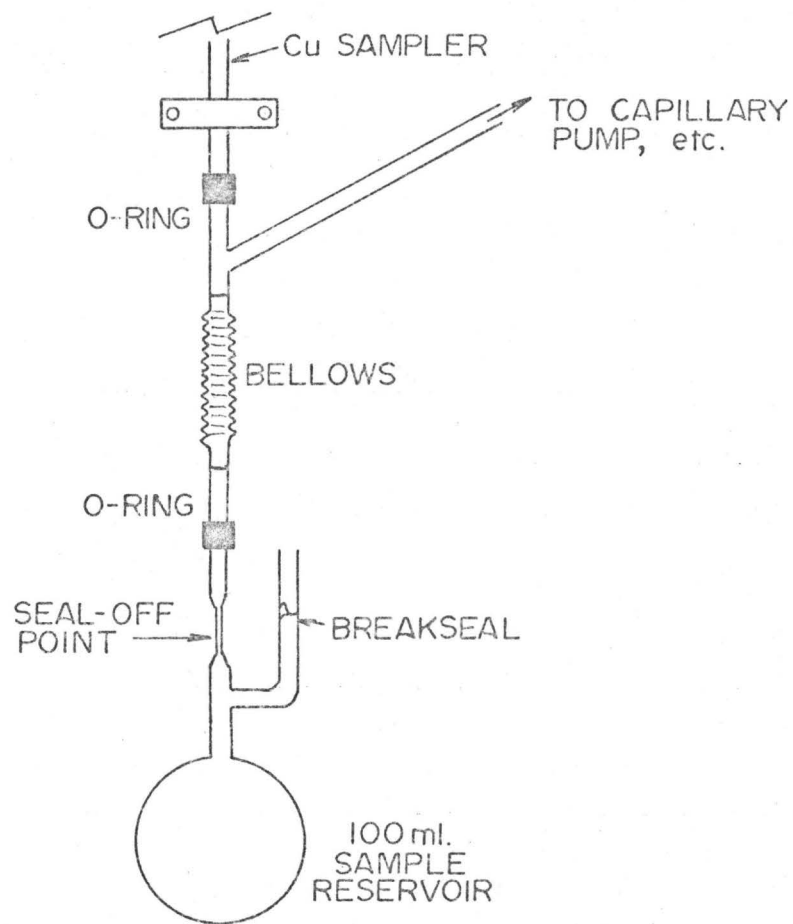
#### (v) Blanks

For each series, at least one "blank extraction" was performed. In the HUDSON 70 series one blank for each station was taken to determine the variability of the blank. Thus it was possible to determine the amount of helium that diffused into the extraction line during extraction, and allow corrections to be made. Table 3 summarizes the results.

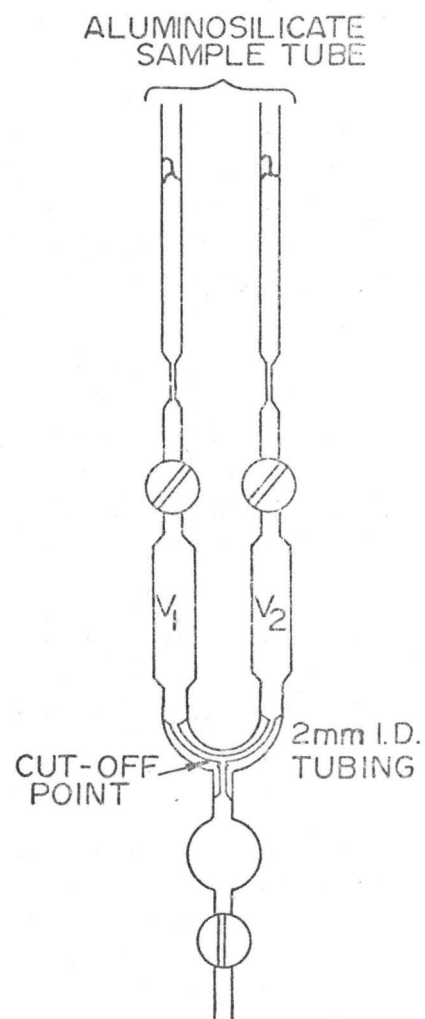
Also, it was necessary to determine the length of time necessary for "quantitative" (better than 99.9%) extraction. This was achieved by extracting the gases remaining in the sea water after a regular extraction had been performed. Extraction efficiencies were determined for Ne and Xe.

FIGURE 2 : Extraction line for the GEOSECS Leg I series.





(a) The sample reservoir system.



(b) The splitter.

FIGURE 3: Leg III modifications to the GEOSECS extraction line.

TABLE 3  
EXTRACTION BLANK RESULTS

Series	Helium Blank*	
	( $\times 10^{-9}$ cc)	(% of sample size)
GEOSECS II	2.2	0.2
HUDSON 70	5.2	0.5
GEOSECS Leg I	3.1	0.3
GEOSECS Leg III	1.6	0.2

\* for small splits.

The HUDSON 70 blanks showed a variance of less than 10% of the blank size. This meant that negligible error was introduced to the helium measurements after blank corrections were made.

#### D. Helium Isotope Measurements

##### (i) The GEOSECS II analyses

The procedure and apparatus used for the GEOSECS II samples is identical to that of Beg (1971). The samples were analyzed on a ten-inch, 90° sector, direction focussing mass-spectrometer operated in the static mode. The mass resolution of the instrument was 1:625, enabling complete separation of the H<sub>3</sub>-HD and the <sup>3</sup>He peaks. Each sample was bracketted by air samples of roughly the same size to monitor instrument discrimination. All samples were purified by exposure to hot, then cooled, titanium metal sponge and toeplered into a reproducible volume from which they were admitted to the mass spectrometer through a charcoal trap cooled by liquid nitrogen.

##### (ii) The branch-tube mass spectrometer

The Branch-Tube spectrometer (Fig. 4) was a 10-inch radius, 90° sector, direction focussing, simultaneous collection mass spectrometer specifically designed for

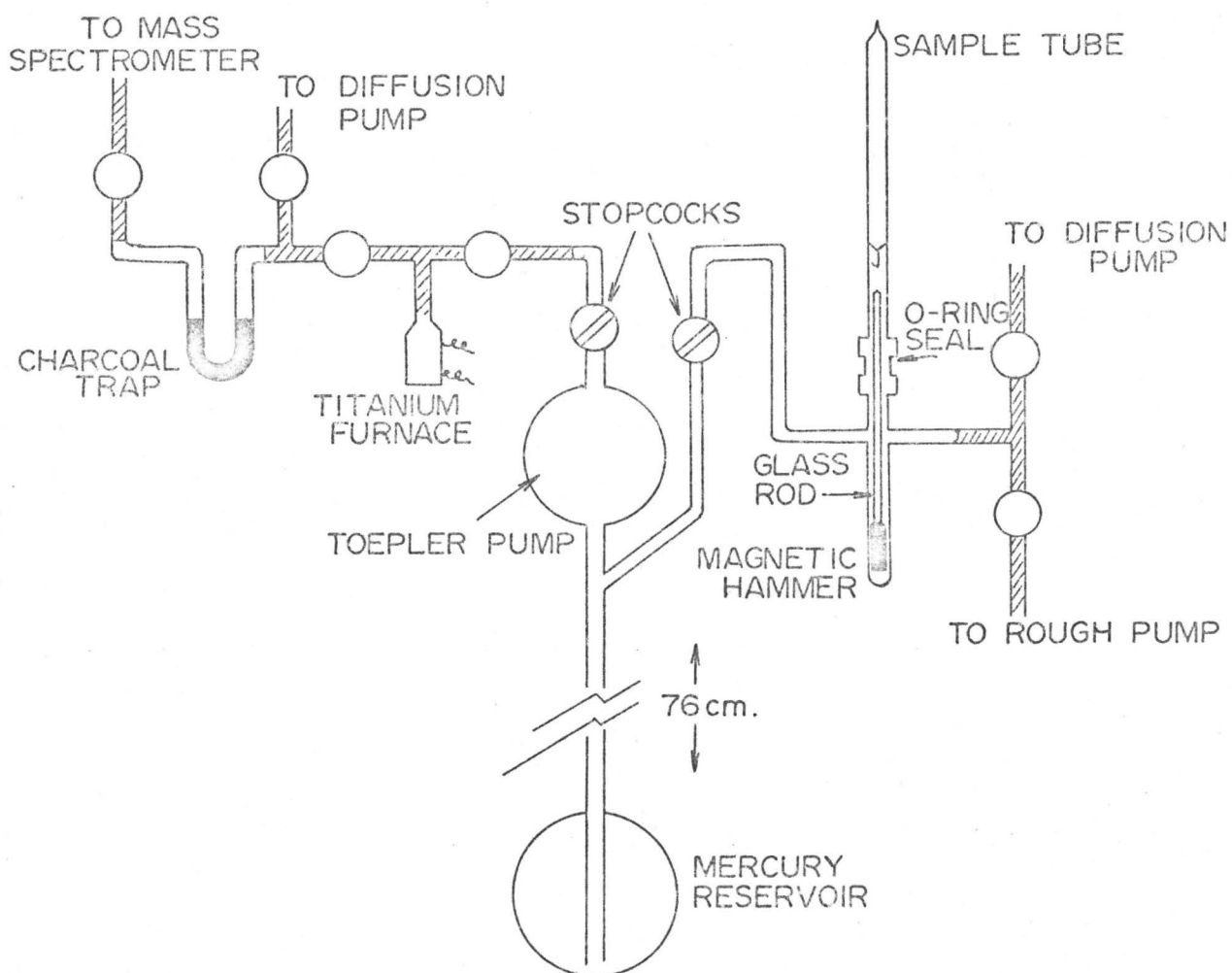
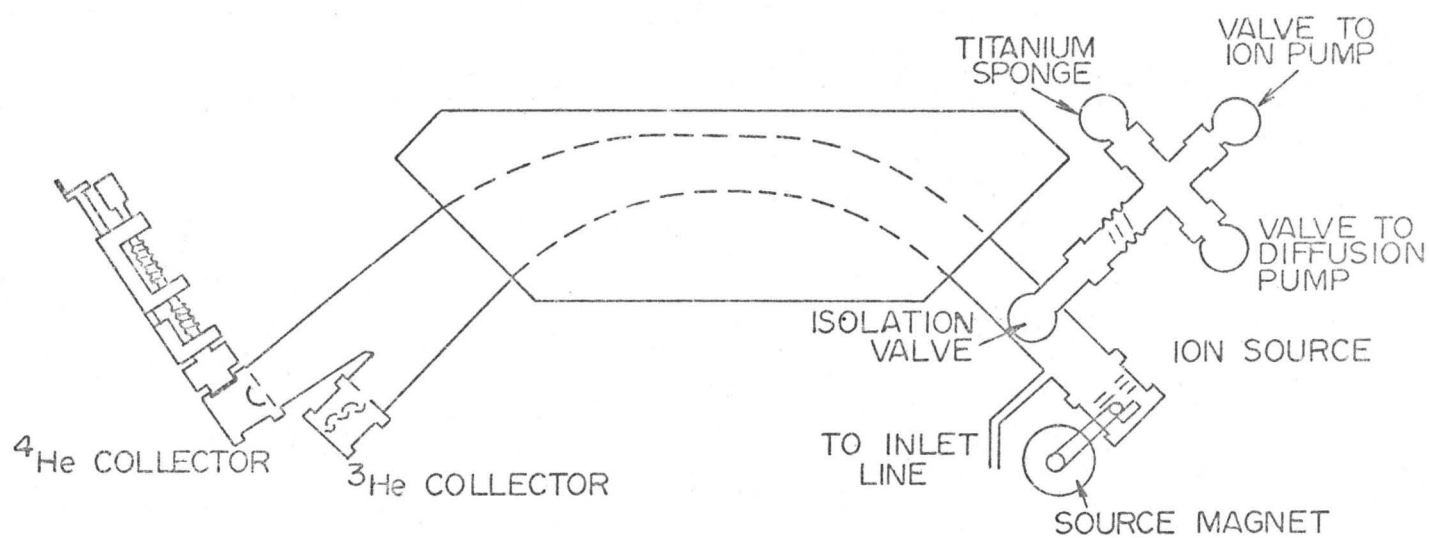


FIGURE 4: The branch-tube mass spectrometer and sample inlet system.

isotopic analysis of small helium samples in the static mode. The "tube" was channelled from a solid block of inconel to minimize the internal volume. Because the precision of the isotope ratio determinations is limited by  $^3\text{He}$  ion currents the smaller internal volume (less than one twentieth of its predecessor) resulted in greatly improved precision.

The pumping system consisted of a mercury vapour diffusion pump and an ion pump, both of which could be isolated from the pumping manifold by one-inch Granville-Phillips ultra-high vacuum valves. The pumping manifold was connected to the spectrometer by a one-inch valve of the same kind. In addition to the pumps, a stainless steel thimble containing about 10 g of titanium sponge was attached to the manifold. At room temperature the titanium acted as a pump for hydrogen, maintaining the HD peak at operable levels during static operation.

The  $^3\text{He}$  collection system was a 0.3 mm slit followed by a focussed mesh electron multiplier. The instrument mass resolution was 1:625, sufficient to clearly resolve the  $^3\text{He}$  peak from the HD- $\text{H}_3$  peak. The  $^4\text{He}$  collection system consisted of an adjustable width slit followed by a Faraday cup, all mounted on a movable platform.

The data acquisition system consisted of two vibrating reed electrometers interfaced to a frequency counter, operated in the ratio mode, by means of two voltage-to-frequency converters. The counter output, a number

proportional to the isotope ratio, was stored by a digital printer. Details of a similar system are given by Beaver (1973).

An analysis consisted of many digital integrations (approximately 30 seconds in length - inversely proportional to the  $^4\text{He}$  signal) of the  $^3\text{He}/^4\text{He}$  ratio with periodic measurements of the  $^3\text{He}$ -Baseline/ $^4\text{He}$  ratio. The latter measurements were achieved by incrementing the accelerating voltage by 6 V. The  $^4\text{He}$  acceptance slit was adjusted to sufficient width ( $\sim 1$  mm) to allow entrance of the  $^4\text{He}$  beam at both voltages. The voltage switching and associated functions were controlled automatically by a digital programmer.

(iii) Sample measurement using the branch-tube spectrometer

The gas samples prior to admission were treated in the same fashion as the GEOSECS II samples. The inlet line is shown in Fig. 4.

The general format of analysis was nine blocks of measurements each consisting of five integrations of the  $^3\text{He}/^4\text{He}$  ratio bracketted by single integrations of the baseline/ $^4\text{He}$  ratio. Since (with the exception of the HUDSON 70 samples) there was no apparent trend with time, the ratios were averaged to give the final result. As before, sea samples were bracketted with air samples.

The HUDSON 70 samples suffered a constant ratio shift with time due to a small  $^3\text{He}$  memory effect. The  $^3\text{He}$  memory resulted from sand-blasting some of the source plates with sand that had been exposed to large amounts of  $^3\text{He}$ . After the HUDSON series, the memory was removed by electropolishing the plates.

#### E. Spike Preparations

##### (i) Helium and neon

Separated isotopes ( $^3\text{He}$ ,  $^{22}\text{Ne}$  and  $^{20}\text{Ne}$ ) were purchased from Monsanto Laboratories, and  $^4\text{He}$  was obtained by boiling liquid helium. Large aliquots ( $10^{-3}$  to  $10^{-2}$  cc STP) of each isotope were first prepared, and small aliquots ( $10^{-7}$  to  $10^{-6}$  cc STP) were prepared by re-expanding the large aliquots.

To prepare the large aliquots, the gas was first purified by passing it through cool titanium (to remove hydrogen) and activated charcoal cooled by liquid nitrogen. An accurately calibrated glass volume  $V_1$  (see Fig. 5) was then filled with the gas at an accurately known pressure and temperature. The contents of  $V_1$  were then expanded into  $V_2$ , a sufficient time allowed for pressure equilibrium ( $> 30$  min.) and aliquots taken using another calibrated volume ( $V_3$ ).

The small aliquots were prepared by re-expanding a large aliquot of  $^3\text{He}$  and  $^{22}\text{Ne}$  into  $V_2$ , and further aliquots



(using  $V_3$ ) taken. Care was taken (by taking blanks) to ensure that the system contained a negligible residual from the large spike preparations. The small aliquots ("spikes") were used for isotope dilution of the gas samples extracted from the sea water.

After a sufficient number of spikes had been prepared, a  $^{20}\text{Ne}$  and  $^4\text{He}$  aliquot was admitted to  $V_2$ , in addition to the already present  $^3\text{He}$  and  $^{22}\text{Ne}$ . The resultant mixture, once the  $^3\text{He}$  and  $^{22}\text{Ne}$  had been corrected for depletion and insertion loss, had precisely known isotopic ratios. Aliquots of this served as standards for monitoring mass-spectrometric discrimination.

(ii) Krypton and xenon standards

The krypton-xenon spikes consisted of a  $^{80}\text{Kr}$ - $^{82}\text{Kr}$ - $^{128}\text{Xe}$  mixture produced by thermal neutron irradiation of a KI-KBr mixture. The size of the spikes were determined by mass spectrometric comparison with accurately known atmospheric krypton-xenon standards. The spike gases were purified over hot titanium and expanded into a 5l reservoir, from which aliquots were taken directly on the mass-spectrometer inlet system.

The calibrating standards were prepared from separated gases obtained from Linde Gas Co. Large aliquots were made in a similar fashion to the helium-neon spikes, but with a different purification: the gases were exposed to hot

titanium. A large aliquot of each gas was expanded into an accurately calibrated 5ℓ reservoir and small aliquots were taken using an accurately calibrated volume attached to the mass-spectrometer sample inlet system.

(iii) Volume calibrations

The volumes, except for  $V_2$  ( $\sim 10\ell$ ) and the 5ℓ reservoir were calibrated by repeated weighings with mercury. The standard deviation of a measurement was used as the volume uncertainty. The average relative uncertainty was 0.01%.

The 5ℓ reservoir was calibrated volumetrically with water using a flask which in turn was calibrated gravimetrically with water. The uncertainty in measurement was determined to be .02%. The 5ℓ reservoir was used to calibrate the 10ℓ volume ( $V_2$ ). This was achieved by filling the 5ℓ volume with  $N_2$  at a known pressure, expanding the  $N_2$  into  $V_2$  and measuring the resultant pressure. The precision of the determination was obtained by repetition to be 0.08%.

(iv) Spike size calculations and uncertainties

The size of a spike is given by

$$S = V_1 \cdot \frac{P}{P_0} \cdot \frac{T_0}{T} \cdot (1-\delta) \cdot \frac{V_2}{V_1+V_2} \cdot \frac{V_3}{V_2+V_3} \cdot \frac{V_2'}{V_1'+V_2'} \cdot \frac{V_3'}{V_2'+V_3'} \quad (5)$$

$$\delta \equiv \frac{Pb}{RT}$$

where the first three terms are the usual ideal gas pressure-temperature corrections,  $\delta$  is a first order correction for a van der Waal's gas, the fifth term is the insertion loss, the sixth is the aliquot ratio and the seventh and eighth are the corresponding terms for the re-expansion.

The expression given does not take into account the "interstitial volumes" (the volumes between the calibrated volumes) or depletion losses. The former were measured by volumetric comparison with the resident calibrated volume ( $V_3$ ) using nitrogen and a manometer. These corrections were made in the actual calculations. In addition it was necessary to measure and correct for a slight ( $< 1^\circ\text{C}$ ) variable temperature differential between the aliquot volume and the reservoir.

As can be readily seen, the relative uncertainty in the spike size was the quadrature sum of the relative uncertainties of the pressure, temperature and all the volumes. Table 4 gives a summary of the uncertainties. The resultant uncertainties were .2% for the helium-neon spikes and .1% for the krypton-xenon standards.

TABLE 4

## ABSOLUTE AND RELATIVE MEASUREMENT UNCERTAINTIES

Measurement	Absolute Error* (in appropriate units)	Maximum Relative Error* (in %)
Pressure	0.2 torr	.04
Temperature	0.1°K	.03
Volume $V_1, V_3$	— **	.01
5 l Vol.	1.0 cc	.02
10 l Vol.	8.5 cc	.08

\* One standard deviation

\*\* Varied with the size of the volume.

## F. Isotope Dilution Mass Spectrometry

### (i) Helium and neon

The mass spectrometer used by Beg (1971) suffered from static helium background rise. This was due to helium diffusing from the electron multiplier dynode resistors, which were gas filled. The resistors were replaced with evacuated envelope resistors. In addition, the ground glass valves used to isolate the mass spectrometer during static operation were replaced with metal valves.

The sample and spike, in breakseal tubes, were attached to the sample inlet system by means of O-ring couplings. They were allowed to mix; then purified and inletted in a fashion identical to the helium isotope samples. At regular intervals standards (without spikes) were processed and analyzed in the same way to monitor instrument mass discrimination.

An analysis consisted of twenty-four alternate, one-second digital peak height integrations on each of the helium isotopes, followed by a similar treatment of the neon isotopes ( $^{20}\text{Ne}$  and  $^{22}\text{Ne}$ ). Switching between isotopes was achieved by altering the accelerating voltage, whereas the magnetic field was changed to alternate between the helium and neon mass regions. The isotopic ratios, calculated from the peak heights, were averaged for each gas in an analysis. An "internal precision" was estimated by calculating the

standard deviation of each mean, and this compared well with the reproducibility as determined by the monitoring standards.

(ii) Krypton and xenon

The krypton and xenon samples were analyzed with the spectrometer in the dynamic mode (source valve closed, collector valve open).

The sample tubes were sealed to the sample line (Fig. 6) and the line evacuated, flamed and isolated from the pumps. An aliquot was admitted to the line from the spike reservoir and then the breakseal of the sample tube was broken. To ensure mixing, the gas was condensed on activated charcoal and then released. The mixture was then condensed at the bottom of a charcoal column using liquid nitrogen. The column was then warmed to  $-78^{\circ}\text{C}$  using a dry-ice acetone bath and maintained at that temperature for ten minutes. During this time any gas evolved (largely argon) was condensed on activated charcoal in a recovery sample tube, which was flame sealed at the end of the ten minute period. The remaining gas was transferred to the reservoir which was then isolated from the line and the mercury raised to the top to maximize the pressure behind the gas leak. Several minutes were allowed for flow equilibrium to be reached.

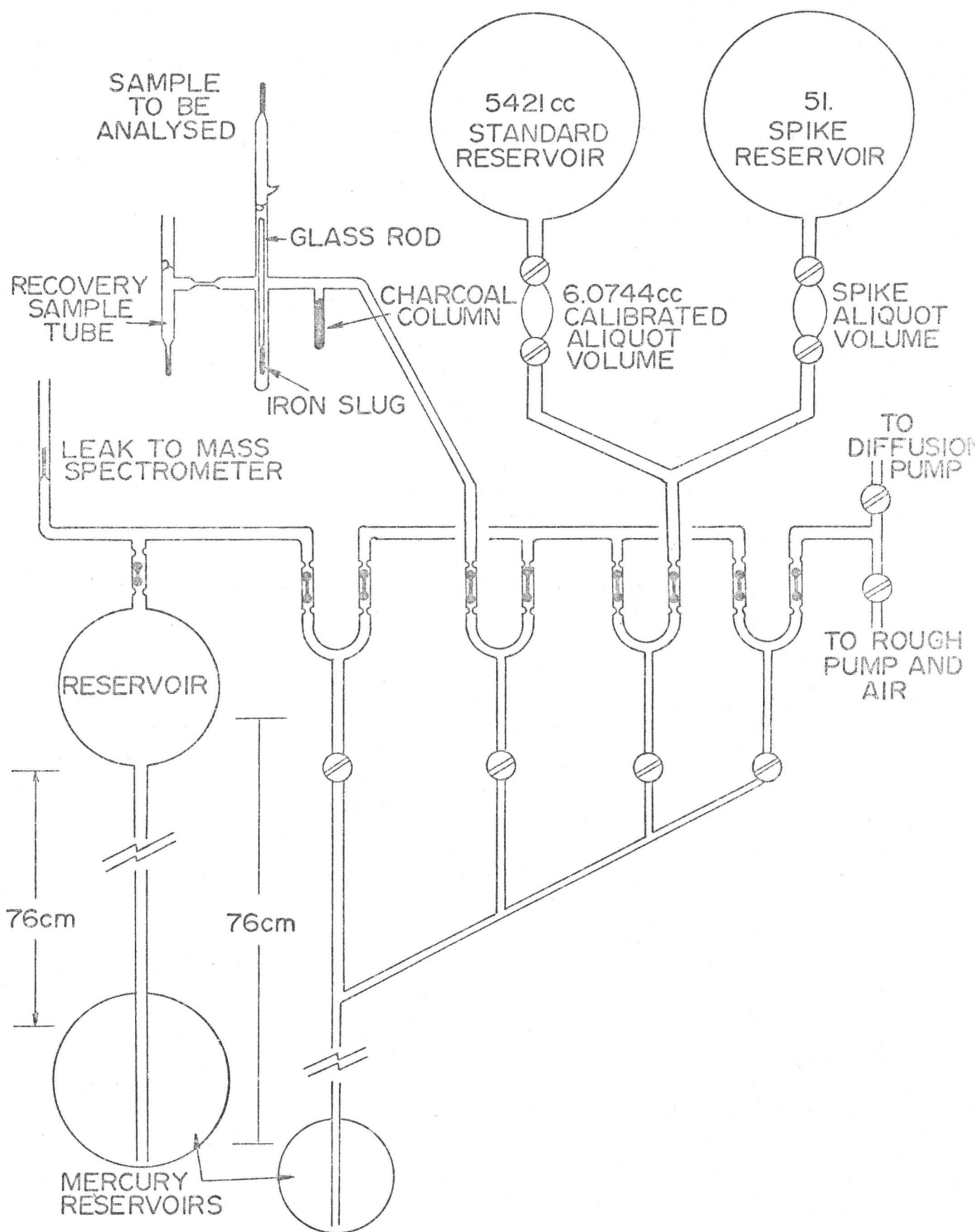


Figure 6: The Kr-Xe sample line.

Measurement consisted of 96 one-second digital peak-height integrations of five isotopes in the following pattern:

A R B R C R D R .

The pattern was repeated twelve times. Each letter represents an isotope (given in Table 5 for each gas). Digitally controlled voltage stepping was used between isotopes, and magnet stepping between gases. The ratio of each of the four isotopes A, B, C and D were taken with respect to the average reference isotope peak height immediately preceding and following, and the average ratio taken for each isotope in an analysis.

TABLE 5  
KRYPTON AND XENON ISOTOPES

Gas	Isotope				
	A	B	C	D	R (Reference)
Xenon	136	132	131	129	128*
Krypton	86	84	83	82*	80*

\* Spiked isotopes.

## CHAPTER 3

### THE ATLANTIC: RESULTS AND DISCUSSION

#### A. Results

The helium concentrations, saturation anomalies\*, and isotope ratio anomalies together with relevant hydrographic data are given for stations\*\* 4, 37, 40, 48 and 54 in Table 5. For stations\*\* 3, 5, 11, 27, 30 and GII<sup>†</sup>, in addition to the above information, "Tritium-helium Ages" are given. These Ages are calculated from the helium data of this work and the tritium data of Östlund et al. (1974), according to

$$\tau = 17.69 \log_e \left\{ 1 + 0.0542 \frac{\delta'(^3\text{He})}{T} C(\text{He}) \times 10^5 \right\} \quad (6)$$

as derived in Appendix 1. In the above expression,  $\tau$  is the Tritium-helium Age in years,  $T$  is the tritium concentration in T.U. (1 T.U. =  $10^{-18}$  T/H),  $C(\text{He})$  the helium concentration in cc STP/Kg, and  $\delta'(^3\text{He})$  is the helium isotope ratio anomaly relative to air equilibrated water, defined by

---

\* relative to the solubility data of Weiss (1971).

\*\* Station locations are given in the tables, along with date of sampling. See Fig. 7, for a map of positions.

† The GEOSECS II Intercalibration Station, hereafter referred to as "GII".

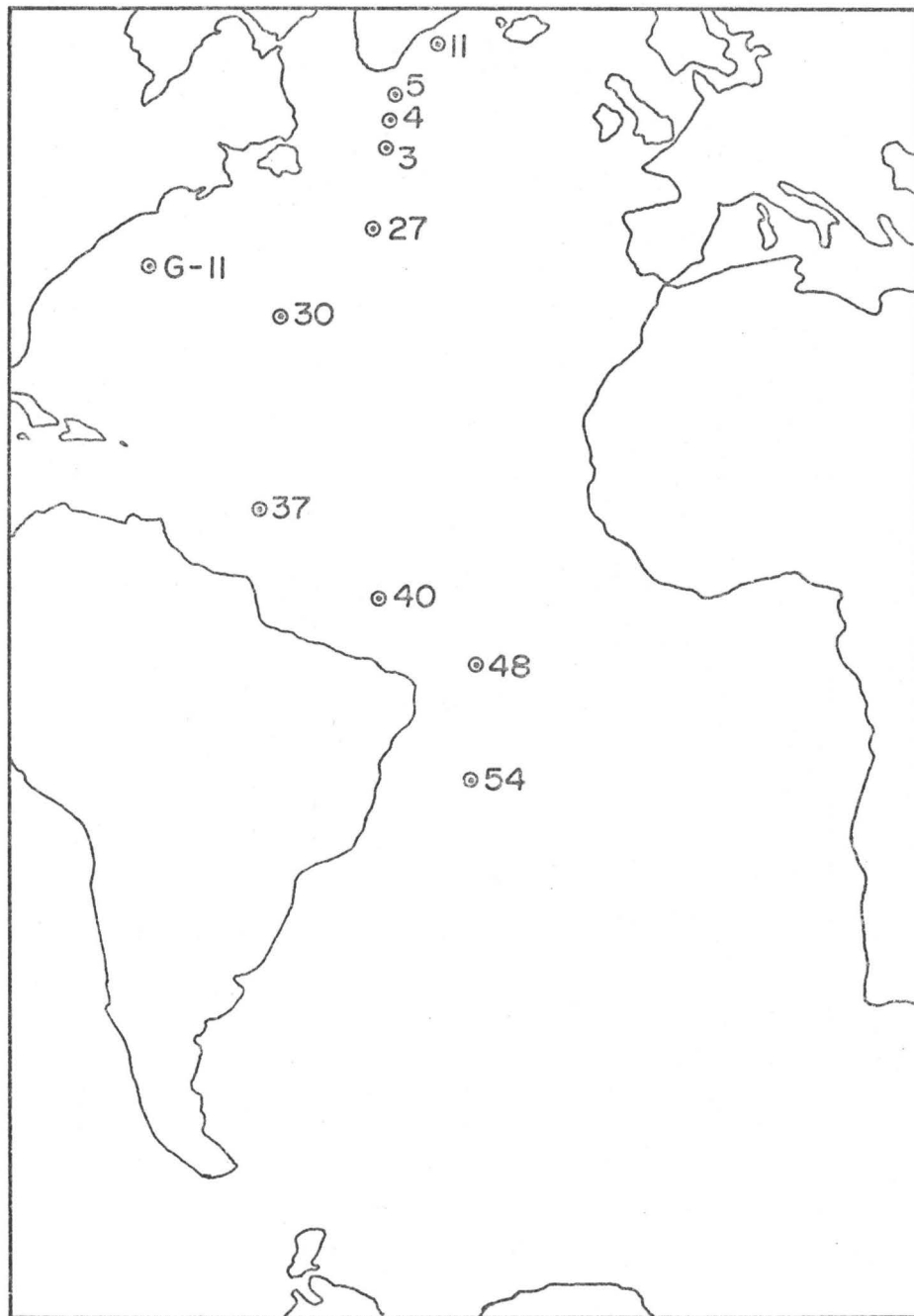


FIG.7 : Station positions in the Atlantic.

$$\delta'(^3\text{He}) \equiv \delta(^3\text{He}) + (1-\alpha) \times 100\% \quad (4)$$

where  $\alpha$  is the solubility isotope fractionation factor. The numerical factor in Eq. (5) contains appropriate conversion factors, and assumes an average potential density of  $1.026 \text{ g cm}^{-3}$ . The errors quoted are computed from a formula derived and given in Appendix 1.

At stations where tritium values are available, the observed helium isotope ratio anomalies have been corrected for in storage decay of tritium. These corrections varied from 0 to -2.5%, with the largest corrections, corresponding to the largest tritium concentrations, being in the near-surface samples. It should be noted that due to low tritium levels the observed deep water  $\delta(^3\text{He})$  patterns were only slightly altered by in storage decay corrections.

The helium concentrations at stations 4, 27, 30 and GII were measured using the isotope dilution technique. For all the stations helium concentrations were determined by the less precise method of peak-height comparison with a standard air aliquot. Regression of the peak-height data against the isotope dilution data for stations 4, 27 and 30 (a total of 59 samples) allowed a calibration of the air aliquot and also an estimate of the uncertainty of the peak-height data. The latter agreed well with the reproducibility of the air aliquot measurements.

Table 8 gives the neon concentrations and saturation anomalies for stations 4, 27, 30 and GII, as determined by isotope dilution. As with helium, the neon saturation anomalies were calculated relative to the solubility data of Weiss (1971) and the quoted uncertainty includes that of the solubility values. The saturation anomalies are defined by

$$\Delta(\%) \equiv \{C/C^*(\theta,S) - 1\} \times 100\% \quad (1)$$

where C is the measured concentration and  $C^*(\theta,S)$  is the solubility equilibrium concentration at the potential temperature and salinity of the sample.

Profiles (plots versus depth) of the helium isotope ratio anomalies are given in Fig. 12 for all stations. Tritium-helium Age profiles are shown in Fig. 15, and profiles of  $\Delta\text{He}$  and  $\Delta\text{Ne}$  are given in Figs. 8 and 9<sup>†</sup>. In addition, profiles of a quantity called the "Excess Helium" defined by

$$\Delta'\text{He} \equiv \Delta\text{He} - \Delta\text{Ne}$$

are shown in Fig. 10.

---

†

for the isotope dilution stations only.

TABLE 6

## HELIUM AND TRITIUM-HELIUM AGE DATA FOR ATLANTIC STATIONS

Station 11								63.5°N × 35.2°W	
Depth	Potential	Salinity	He Concentration	$\Delta$ He	$\delta(^3\text{He})$	T-He Age			
(m)	Temperature	(‰)	(cc STP/Kg <sup>-1</sup> )	(%)	(Corrected)	(y)	±		
	(°C)		(× 10 <sup>5</sup> )		(%)				
31	7.65	34.97	3.98	3.4	-1.3	-0.1	0.3		
83	6.77	35.05	3.96	2.7	-0.5	0.5	0.4		
168	5.99	35.02	4.06	5.0	-0.5	0.5	0.3		
258	5.36	34.99	4.03	3.9	0.3	1.2	0.4		
358	4.83	34.94	4.13	6.3	-1.0	0.1	0.4		
459	4.55	34.93	4.13	6.1	0.6	1.3	0.4		
558	4.29	34.92	4.09	5.0	-0.7	0.3	0.3		
658	4.13	34.92	4.07	4.4	0.8	1.5	0.4		
759	4.00	34.91	4.02	3.1	-0.1	0.9	0.4		
861	3.88	34.91	4.10	5.1	1.1	1.9	0.4		
906	3.81	34.91	4.03	3.2	1.3	2.1	0.4		
961	3.78	34.91	4.06	4.0	-0.2	1.0	0.5		
1005	3.74	34.90	4.05	3.7	0.1	(1.3)	0.5		
1207	3.69	34.92	4.09	4.7	3.3	5.7	0.6		
1406	3.68	34.94	4.09	4.7	2.2	6.8	0.9		
1612	3.55	34.95	4.05	3.7	2.2	7.1	0.9		
1807	3.37	34.95	4.08	4.4	2.9	9.3	1.0		
1953	2.97	34.92	4.06	3.7	2.0	(3.6)	0.5		
2051	2.57	34.90	4.15	5.8	1.1	2.3	0.5		
2210	1.76	34.90	4.11	4.4	-0.3	1.0	0.5		
2380	1.08	34.88	4.18	5.8	1.6	(2.4)	0.4		
UNCERTAINTIES			0.04	1.0	0.5				

Station 5								56.9°N × 42.8°W	
Depth	Potential	Salinity	He Concentration	$\Delta$ He	$\delta(^3\text{He})$	T-He Age			
(m)	Temperature	(‰)	(cc STP/Kg <sup>-1</sup> )	(%)	(Corrected)	(y)	±		
	(°C)		(× 10 <sup>5</sup> )		(%)				
21	6.89	34.64	4.02	4.0	-2.5	-0.6	0.2		
110	4.74	34.85	3.99	2.6	-0.8	0.3	0.4		
209	4.36	34.89	4.12	5.8	0.9	1.5	0.3		
463	3.61	34.86	4.00	2.4	2.1	2.3	0.3		
667	3.46	34.86	4.17	6.7	1.8	2.2	0.3		
861	3.36	34.85	4.15	6.1	1.7	2.1	0.3		
988	3.36	34.86	4.09	4.6	2.6	2.9	0.4		
1191	3.63	34.94	4.10	5.0	2.9	5.5	0.6		
1411	3.60	34.93	4.15	6.2	2.0	6.9	1.0		
1639	3.42	34.95	4.00	2.3	1.1	7.1	1.4		
1811	3.33	34.96	4.12	5.4	0.5	5.2	1.4		
1864	3.30	34.96	4.04	3.3	1.1	7.8	1.5		
2086	3.11	34.96	4.13	5.5	1.4	(8.8)	1.5		
2260	2.97	34.95	4.10	4.7	1.1	(7.2)	1.4		
2363	2.91	34.96	4.13	5.4	1.5	(8.3)	1.4		
2729	2.68	34.96	4.15	5.9	1.6	(8.6)	1.4		
2819	2.62	34.96	4.17	6.3	2.5	9.9	1.2		
3014	2.37	34.94	4.06	3.4	1.1	(5.4)	1.1		
3014	2.36	34.94	4.07	3.7	1.2	(5.6)	1.1		
3154	2.06	34.93	4.10	4.3	2.0	(5.8)	0.8		
UNCERTAINTIES			0.04	1.0	0.5				

TABLE 6 - continued

Station GII							35.8°N × 68.0°W	
Depth	Potential	Salinity	He Concentration	$\Delta$ He	$\delta(^3\text{He})$	T-He Age		
(m)	Temperature	(‰)	(cc STP/Kg <sup>-1</sup> )	(%)	(Corrected)	(y)	±	
	(°C)		(× 10 <sup>5</sup> )		(%)			
20	26.57	36.06	3.85	4.8	-	-	-	
204	18.3	36.55	3.87	4.3	-0.5	0.3	0.6	
508	17.19	36.44	3.88	4.3	4.1	2.6	0.5	
996	8.26	35.34	3.94	2.8	-1.8	-1.0	2.1	
1221	5.08	34.99	3.98	2.5	-1.0	0.4	2.8	
1511	4.40	34.98	4.03	3.5	-0.9	0.9	3.7	
1916	3.78	34.96	4.13	5.8	3.6	15.7	2.9	
2215	3.53	34.97	4.12	5.5	0.3	7.8	5.2	
2531	3.27	34.96	4.13	5.6	2.2	15.3	4.1	
2955	2.85	34.95	4.05	3.4	3.9	20.7	3.8	
3214	2.56	34.93	4.09	4.3	7.2	37.7	6.6	
3520	2.30	34.92	4.09	4.1	2.2	24.5	7.1	
4554	1.89	34.89	4.09	3.9	0.3	14.8	9.0	
UNCERTAINTIES			0.01	0.4	1.2			

Station 30							31.8°N × 50.8°W	
Depth	Potential	Salinity	He Concentration	$\Delta$ He	$\delta(^3\text{He})$	T-He Age		
(m)	Temperature	(‰)	(cc STP/Kg <sup>-1</sup> )	(%)	(Corrected)	(y)	±	
	(°C)		(× 10 <sup>5</sup> )		(%)			
50	21.74	36.55	3.94	6.8	-0.1	(0.6)	0.1	
201	17.71	36.43	3.93	5.7	0.5	(0.9)	0.1	
300	17.34	36.42	3.90	4.8	3.5	(2.7)	0.1	
401	16.49	36.28	3.93	5.4	5.0	(3.9)	0.2	
499	15.06	36.03	3.89	3.8	4.7	4.1	0.2	
590	13.46	35.79	3.95	4.9	6.0	5.6	0.2	
700	11.55	35.51	3.93	3.7	2.2	4.8	0.4	
903	7.62	35.16	4.00	4.1	1.4	10.4	1.4	
1003	6.72	35.15	4.03	4.5	1.1	(8.6)	1.1	
1103	5.79	35.11	4.12	6.5	2.0	(7.3)	0.6	
1302	4.92	35.08	4.04	4.1	1.0	(4.6)	0.5	
1394	4.74	35.08	4.06	4.5	1.7	(8.0)	0.8	
1793	3.82	35.01	4.07	4.3	1.3			
2193	3.40	35.00	4.08	4.4	0.7			
2593	3.00	34.97	4.11	5.0	1.7			
2992	2.69	34.95	4.14	5.6	1.4			
3393	2.37	34.92	4.17	6.2	1.0			
3783	2.11	34.9	4.15	5.6	1.6			
4184	1.90	34.89	4.20	6.7	1.8			
4584	1.74	34.87	4.18	6.1	2.7			
4985	1.65	34.86	4.14	5.1	2.2			
5387	1.63	34.86	4.19	6.3	1.5			
5786	1.63	34.86	4.15	5.3	1.7			
UNCERTAINTIES			0.01	0.4	0.2			

TABLE 6 - continued

Station 3				51.0°N × 43.0°W			
Depth	Potential	Salinity	He Concentration	$\Delta$ He	$\delta$ ( $^3$ He)	T-He Age	
(m)	Temperature	(‰)	(cc STP/Kg $^{-1}$ )	(%)	(Corrected)	(y)	
	(°C)		( $\times 10^5$ )		(%)		
105	9.28	35.01	-	-	0.2	0.6	0.2
182	6.79	34.74	-	-	1.7	1.3	0.2
274	7.62	34.99	3.97	3.2	-0.1	0.5	0.2
377	6.05	34.82	4.10	5.9	-2.4	-0.6	0.3
464	5.13	34.83	-	-	2.4	2.3	0.3
575	4.77	34.90	4.05	4.1	2.7	2.8	0.3
813	4.16	34.90	-	-	3.7	3.5	0.3
1083	4.17	34.96	4.07	4.5	3.8	5.2	0.5
1376	3.80	34.94	4.27	9.4	7.9	9.9	0.5
1575	3.69	34.94	-	-	6.4	12.5	0.8
1875	3.49	34.94	-	-	3.1	(10.1)	1.1
2039	3.37	34.94	4.10	4.9	1.2	5.3	1.0
2356	3.14	34.95	-	-	0.8	6.3	1.4
2356	3.14	34.95	4.16	6.3	1.0	7.1	1.5
2595	2.87	34.95	4.09	4.4	1.0	(7.6)	1.6
2696	2.73	34.94	4.25	8.4	1.4	9.8	1.7
3089	2.48	34.94	4.22	7.5	4.8	(15.2)	1.3
3267	2.32	34.93	4.21	7.2	11.0	24.9	1.6
3368	2.21	34.93	4.20	6.9	13.5	(25.9)	1.4
3630	2.02	34.93	4.29	9.1	7.1	(12.4)	0.7
3896	1.85	34.92	4.13	4.9	4.7	(7.2)	0.6
4150	1.68	34.91	4.10	4.1	6.1	7.4	0.5
UNCERTAINTIES			0.04	1.0	0.5		

Station 27				42.0°N × 42.0°W			
Depth	Potential	Salinity	He Concentration	$\Delta$ He	$\delta$ ( $^3$ He)	T-He Age	
(m)	Temperature	(‰)	(cc STP/Kg $^{-1}$ )	(%)	(Corrected)	(y)	
	(°C)		( $\times 10^5$ )		(%)		
27	22.12	36.11	3.79	2.6	-1.7	(-0.3)	0.1
102	17.09	36.38	3.91	5.0	1.6	(1.5)	0.1
181	15.82	36.12	3.88	3.8	1.9	1.6	0.1
319	14.36	35.87	3.94	4.9	1.6	1.5	0.1
461	13.45	35.78	4.08	8.3	3.2	2.7	0.1
599	11.26	35.46	4.02	5.9	3.1	3.1	0.2
738	8.69	35.19	4.31	12.5	2.7	5.7	0.4
879	6.15	34.95	4.06	5.0	3.6	(4.5)	0.2
1000	6.03	35.10	4.15	7.3	4.0	7.5	0.4
1268	4.60	35.01	4.05	4.1	3.4	(6.4)	0.4
1441	4.39	35.04	4.07	4.6	2.7	9.5	0.8
1832	3.82	34.97	4.08	4.6	1.7	11.4	1.4
2231	3.46	34.96	4.07	4.2	1.1	(17.4)	3.9
2630	3.11	34.95	4.16	6.3	0.7	(15.6)	3.7
3038	2.76	34.94	4.12	5.1	1.1	14.5	2.7
3442	2.43	34.93	4.10	4.5	0.9	(16.5)	3.8
3855	2.12	34.91	4.12	4.8	1.2	(22.9)	6.6
4257	1.93	34.90	4.14	5.2	1.9	26.4	7.0
4486	1.87	34.90	4.20	6.7	1.0	(17.2)	3.9
4678	1.85	34.90	4.12	4.7	2.0	(15.6)	2.2
4858	1.83	34.90	4.12	4.7	2.5	(11.5)	1.1
UNCERTAINTIES			0.01	0.4	0.2		

TABLE 7  
HELIUM DATA FOR ATLANTIC STATIONS

Station 4					
54.1°N × 43.0°W					
Depth	Potential	Salinity	He Concentration	ΔHe	δ( <sup>3</sup> He)
(m)	Temperature	(‰)	(cc STP/Kg <sup>-1</sup> )	(%)	(%)
	(°C)		(× 10 <sup>5</sup> )		
18	7.43	34.93	3.96	2.8	-1.3
270	3.85	34.85	4.10	5.0	2.7
426	3.78	34.87	-	-	4.1
749	3.67	34.89	4.10	5.0	5.2
1104	3.65	34.91	4.10	5.0	5.6
1601	3.47	34.94	4.10	4.9	1.3
1842	3.32	34.94	4.05	3.6	0.9
2089	3.15	34.95	4.09	4.5	-0.6
2302	3.00	34.96	4.15	6.0	0.6
2701	2.82	34.97	4.14	5.7	2.4
2799	2.78	34.97	4.09	4.4	-0.4
2904	2.72	34.97	4.16	6.1	-0.6
2988	2.62	34.97	4.10	4.6	0.0
3187	2.39	34.94	4.15	5.7	1.0
3392	2.25	34.93	4.07	3.6	1.3
UNCERTAINTIES			.01	.4	.5

Station 37					
12.0°N × 51.0°W					
Depth	Potential	Salinity	He Concentration	ΔHe	δ( <sup>3</sup> He)
(m)	Temperature	(‰)	(cc STP/Kg <sup>-1</sup> )	(%)	(%)
	(°C)		(× 10 <sup>5</sup> )		
39	26.25	36.46	3.81	4.0	-0.44
115	21.09	36.76	3.89	5.5	3.72
227	12.38	35.48	4.00	5.7	3.52
351	9.80	35.11	3.98	4.2	1.31
552	7.22	34.74	4.05	5.0	0.60
751	6.01	34.67	4.09	5.5	1.36
949	5.01	34.67	4.10	5.4	1.84
1199	4.91	34.90	4.12	6.0	1.38
1400	4.48	34.98	4.09	5.1	0.20
1599	4.03	34.99	4.11	5.4	-0.13
1848	3.56	34.98	4.14	6.0	-0.10
1940	3.38	34.97	4.12	5.4	-0.07
2241	3.01	34.96	4.05	3.4	1.46
2539	2.78	34.94	4.16	6.1	1.68
2840	2.56	34.93	4.19	6.8	2.74
3239	2.33	34.92	4.18	6.4	2.49
3441	2.23	34.91	4.27	8.7	1.35
4051	1.94	34.89	4.17	6.0	0.83
4751	1.44	34.84	4.17	5.7	3.37
UNCERTAINTIES			.04	1	.2

TABLE 7 - continued

Station 40				3.5°N × 38.0°W	
Depth	Potential	Salinity	He Concentration	ΔHe	δ( <sup>3</sup> He)
(m)	Temperature	(‰)	(cc STP/Kg <sup>-1</sup> )	(%)	(%)
	(°C)		(× 10 <sup>5</sup> )		
36	27.54	35.99	3.82	4.2	- .44
135	21.24	36.3	3.9	5.5	1.57
298	9.44	34.87	4.04	5.6	- .37
448	7.53	34.66	4.06	5.3	1.27
600	6.08	34.59	4.31	11.2	1.12
892	4.63	34.59	4.09	4.9	1.88
1008	4.47	34.66	4.12	5.7	1.98
1133	4.44	34.73	4.11	5.4	1.71
1231	4.47	34.83	4.09	5	.42
1712	3.87	34.98	4.14	6.1	.34
2000	3.43	34.96	4.14	5.9	.7
2597	2.72	34.94	4.15	5.9	2.29
2898	2.49	34.92	4.19	6.8	3.53
3209	2.32	34.92	4.13	5.2	2.35
3510	2.18	34.91	4.14	5.3	1.6
3811	1.96	34.89	4.24	7.8	1.02
4062	1.68	34.86	4.25	7.9	1.92
UNCERTAINTIES			.04	1	.2

Station 48				4.0°S × 28.0°W	
Depth	Potential	Salinity	He Concentration	ΔHe	δ( <sup>3</sup> He)
(m)	Temperature	(‰)	(cc STP/Kg <sup>-1</sup> )	(%)	(%)
	(°C)		(× 10 <sup>5</sup> )		
30	26.06	36.08	4	9	-2.01
82	24.88	36.05	3.81	3.6	-.71
153	13.72	35.38	4.24	12.4	-1.14
274	9.84	34.89	4.22	10.4	-.58
433	7.14	34.63	4.04	4.6	.17
594	5.28	34.48	4.12	5.9	.51
759	4.38	34.47	4.13	5.8	1.79
920	4.18	34.54	4.11	5.2	2.38
1090	4.13	34.67	4.12	5.5	2.38
1267	4.3	34.85	4.14	6.2	1.38
1576	3.94	34.96	4.09	4.9	.57
1951	3.4	34.96	4.22	8	1.03
2350	2.96	34.94	4.13	5.5	2.54
3150	2.38	34.91	4.21	7.2	1.89
3549	2.22	34.89	4.17	6.1	1.9
3898	1.8	34.86	4.17	5.9	1.94
4197	.98	34.77	4.25	7.5	5.14
4494	.59	34.73	4.24	7	5.57
4791	.34	34.71	4.28	7.9	6.39
5069	.22	34.69	4.24	6.8	6.52
UNCERTAINTIES			.04	1	.2

TABLE 7 - continued

Station 54			15.5°S × 29.0°W		
Depth	Potential	Salinity	He Concentration	$\Delta$ He	$\delta(^3\text{He})$
(m)	Temperature	(‰)	(cc STP/Kg <sup>-1</sup> )	(‰)	(‰)
	(°C)		(× 10 <sup>5</sup> )		
188	19.00	36.16	4.07	9.6	-1.24
490	6.85	34.56	4.05	4.7	.25
689	4.3	34.40	4.13	5.7	2.39
898	3.65	34.47	4.21	7.5	3.60
1097	3.67	34.63	4.12	5.3	3.02
1297	3.79	34.80	4.12	5.5	1.82
1694	3.36	34.92	4.17	6.6	2.69
1879	3.11	34.93	4.16	6.3	2.33
2278	2.73	34.91	4.52	15.3	3.40
3080	2.38	34.90	4.21	7.2	3.92
3878	1.71	34.86	4.16	5.6	3.75
4389	0.80	34.76	4.24	7.1	5.88
4787	0.38	34.72	4.28	7.9	6.25
5081	0.04	34.69	4.29	7.9	6.58
UNCERTAINTIES			.04	1	.2

TABLE 8  
ATLANTIC NEON DATA

Station 4		54.1°N × 43.0°W		
Depth (m)	Potential Temperature (°C)	Salinity (‰)	Ne Concentration (cc STP/Kg <sup>-1</sup> ) (× 10 <sup>5</sup> )	ΔNe (%)
18	7.43	34.93	17.23	3.8
270	3.85	34.85	18.06	5.6
749	3.67	34.89	17.97	5.0
1164	3.65	34.91	18.04	5.4
1601	3.47	34.94	18.07	5.4
1842	3.32	34.94	17.95	4.6
2089	3.15	34.95	18.05	5.0
2302	3.00	34.96	18.27	6.1
2701	2.82	34.97	18.28	6.0
2799	2.78	34.97	18.13	5.1
2904	2.72	34.97	18.39	6.6
2988	2.62	34.97	18.12	4.9
3187	2.39	34.94	18.35	6.0
3392	2.25	34.93	17.78	2.6
UNCERTAINTIES			0.05	0.4

Station 27		42.0°N × 42.0°W		
Depth (m)	Potential Temperature (°C)	Salinity (‰)	Ne Concentration (cc STP/Kg <sup>-1</sup> ) (× 10 <sup>5</sup> )	ΔNe (%)
27	22.12	36.11	15.22	2.2
102	17.09	36.38	16.07	4.6
181	15.82	36.12	16.13	4.0
319	14.36	35.87	16.34	4.1
461	13.45	35.78	16.92	7.1
599	11.26	35.46	17.02	5.9
738	8.69	35.19	18.21	10.9
879	6.15	34.95	17.54	4.6
1000	6.03	35.10	17.92	6.9
1268	4.60	35.01	17.49	3.0
1441	4.39	35.04	17.73	4.3
1832	3.82	34.97	17.98	5.2
2231	3.46	34.96	17.92	4.5
2630	3.11	34.95	18.17	5.7
3038	2.76	34.94	18.27	5.9
3442	2.43	34.93	18.14	4.8
3855	2.12	34.91	18.14	4.5
4257	1.93	34.90	18.27	5.1
4486	1.87	34.90	18.41	5.9
4678	1.85	34.90	18.18	4.5
4858	1.83	34.90	18.25	4.9
UNCERTAINTIES			0.05	0.4

TABLE B - continued

Station G11 35.8°N × 68.0°W

Depth (m)	Potential Temperature (°C)	Salinity (‰)	Ne Concentration (cc STP/Kg <sup>-1</sup> ) (× 10 <sup>5</sup> )	ΔNe (%)
20	26.57	36.06	15.19	4.9
204	18.3	36.55	16.02	5.2
508	17.19	36.44	15.97	4.1
996	8.26	35.34	16.98	3.2
1221	5.08	34.99	17.50	3.5
1511	4.40	34.98	17.46	2.7
1916	3.78	34.96	17.83	4.3
2215	3.53	34.97	17.62	2.8
2531	3.27	34.96	18.34	6.8
2955	2.85	34.95	17.74	2.9
3214	2.56	34.93	17.48	1.1
3520	2.30	34.92	17.80	2.8
4554	1.89	34.89	18.05	3.8

UNCERTAINTIES .05 .4

Station 30 31.8°N × 50.8°W

Depth (m)	Potential Temperature (°C)	Salinity (‰)	Ne Concentration (cc STP/Kg <sup>-1</sup> ) (× 10 <sup>5</sup> )	ΔNe (%)
50	21.74	36.55	15.85	6.5
201	17.71	36.43	16.28	6.5
300	17.34	36.42	16.05	4.7
401	16.49	36.28	16.27	5.5
499	15.06	36.03	16.16	3.6
590	13.46	35.79	16.58	5.0
700	11.55	35.51	16.66	3.9
903	7.62	35.16	17.49	5.7
1003	6.72	35.15	17.45	4.7
1103	5.79	35.11	17.84	6.2
1302	4.92	35.08	17.65	4.3
1394	4.74	35.08	17.80	5.0
1793	3.82	35.01	17.93	4.9
2193	3.40	35.00	17.99	4.9
2593	3.00	34.97	18.05	4.9
2992	2.69	34.95	18.24	5.7
3393	2.37	34.92	18.28	5.6
3783	2.11	34.90	18.37	5.9
4184	1.90	34.89	18.48	6.3
4584	1.74	34.87	18.38	5.5
4985	1.65	34.86	18.26	4.8
5387	1.63	34.86	18.50	6.1
5786	1.63	34.86	18.22	4.5

UNCERTAINTIES .05 .4

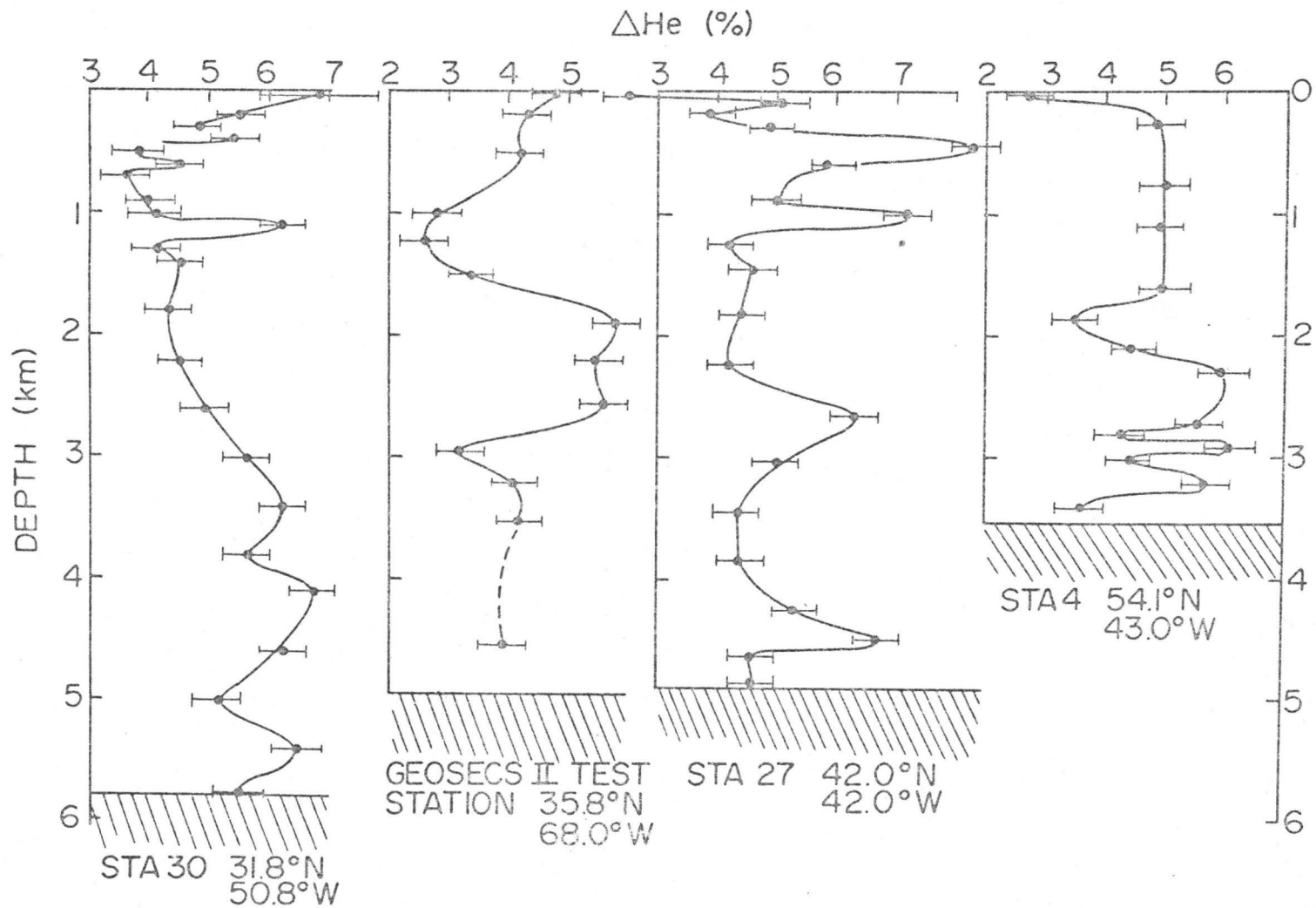


Fig 8 : Helium saturation anomaly profiles for four North Atlantic stations.

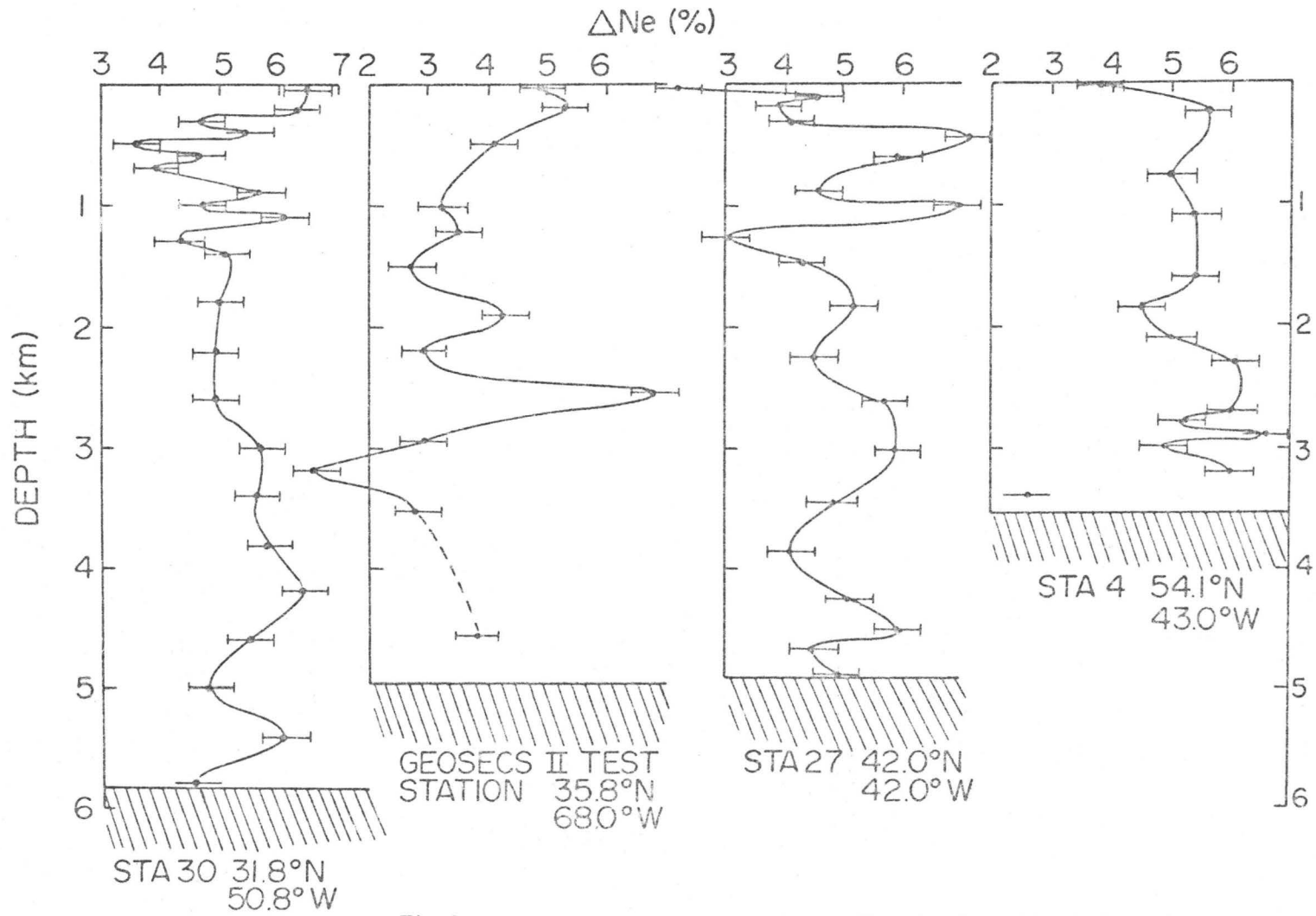


Fig 9 : Neon saturation anomaly profiles for four North Atlantic stations.

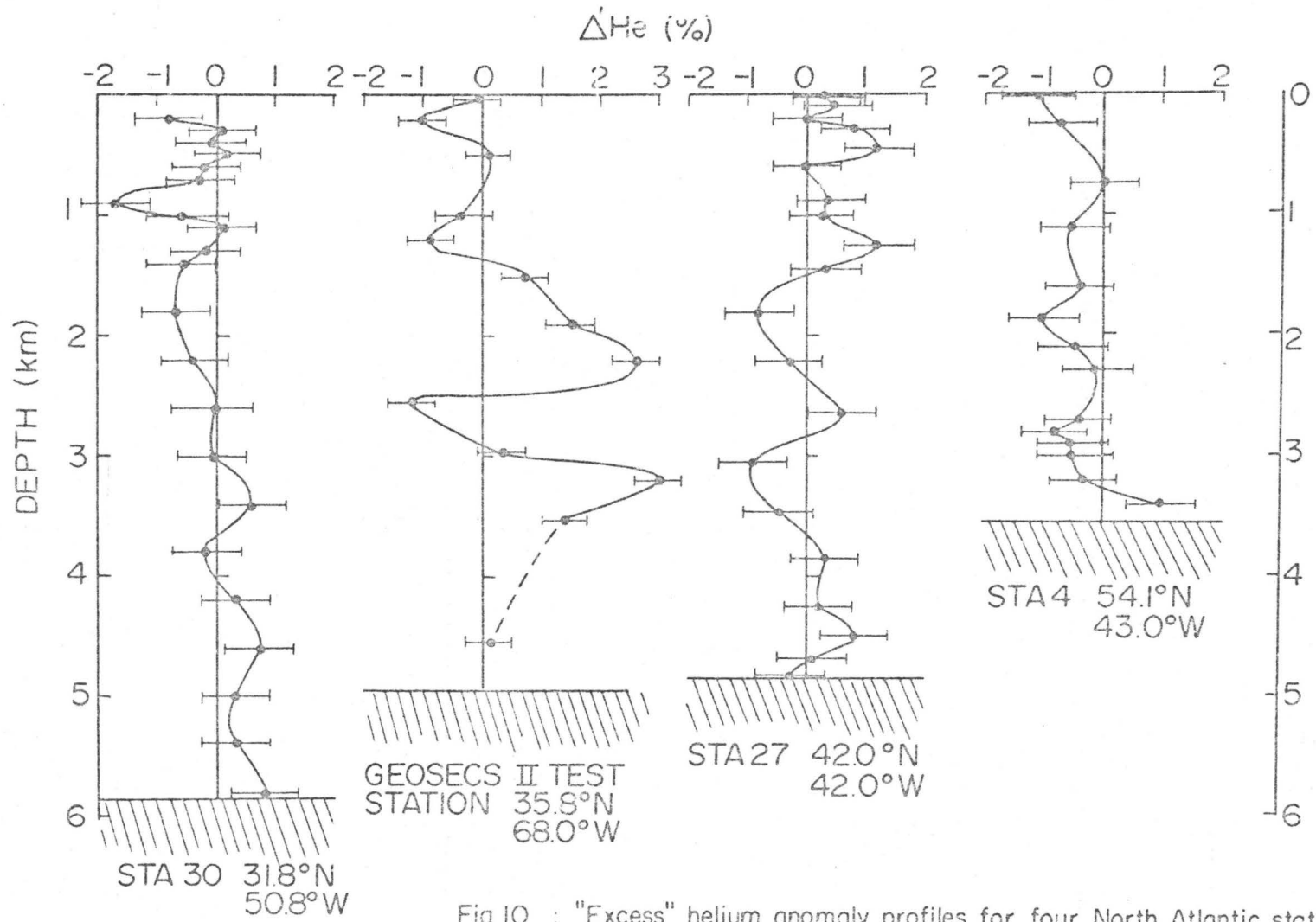


Fig 10 : "Excess" helium anomaly profiles for four North Atlantic stations.

## B. Discussion

### (i) Helium and neon saturation anomalies

The average of all 194  $\Delta\text{He}$  measurements is 5.4%, with a North Atlantic (north of 12°N) average  $\Delta\text{He}$  of  $4.9 \pm 0.2\%$  and a South Atlantic average of  $6.3 \pm 0.2\%$ . This indicates a real difference between the two "oceans". The RMS scatter about the mean is 1.6% in both cases, significantly larger than the standard deviation of an individual measurement. Table 9 gives the average  $\Delta\text{He}$  values for Surface (< 500 m), Intermediate (500 m - 1500 m), Deep (1500 m - 4000 m) and Bottom (> 4000 m) Waters; together with the standard deviation of each mean. The choice of boundaries is to some extent arbitrary, but an attempt has been made (not without compromise) to follow generally accepted views. Included, as well, are North and South Atlantic and grand averages. Because of the abnormally low  $\Delta$  values, the GII data have not been included in the averaging procedure.

With each station-depth-range mean, a RMS scatter was computed, and the scatters averaged over all "peak-height" stations for each depth range. These values, given in Table 10, suggest that aside from surface values, the  $\Delta\text{He}$  values do not vary significantly within any depth range compared to the peak-height uncertainty.

TABLE 9

 $\Delta$ He AVERAGES IN THE ATLANTIC OCEAN

Station No.	Latitude	Surface		Intermediate		Deep		Bottom	
		Avg	$\sigma$	Avg	$\sigma$	Avg	$\sigma$	Avg	$\sigma$
11	63.5°N	4.6	0.6	4.2	0.2	4.6	0.4	—	—
5	57 °N	3.7	0.8	5.7	0.4	4.6	0.4	—	—
4	54 °N	3.9	1.1	5.0	—	4.9	0.3	—	—
3	51 °N	4.5	1.4	6.0	1.7	6.4	0.5	—	—
27	43 °N	4.9	1.0	5.4	0.6	4.9	0.3	5.3	0.5
GII	36 °N	4.5	0.2	2.7	0.2	4.6	0.4	3.9	—
30	32 °N	5.3	0.5	4.6	0.3	5.2	0.3	5.9	0.3
37	12 °N	4.9	0.4	5.4	0.2	6.0	0.5	5.9	0.1
40	3.5°N	5.2	0.3	5.3	0.2	6.1	0.3	7.9	—
48	4 °S	8.0	1.7	5.7	0.2	6.3	0.5	7.3	0.2
54	15.5°S	7.2	2.5	6.0	0.5	6.4	0.3	7.6	0.3
N. Atlantic Avg*		4.6	0.2	5.1	0.2	4.9	0.3	5.6	0.3
S. Atlantic Avg		6.3	0.6	5.6	0.2	6.2	0.1	7.2	0.4
Grand Avg*		5.1	0.4	5.3	0.3	5.4	0.2	6.3	0.5

\* not including the GII values.

TABLE 10  
 AVERAGE SCATTER OF PEAK-HEIGHT VALUES  
 OVER DIFFERENT DEPTH RANGES

Range	Scatter (%)	# of Samples
Surface	1.9	26
Intermediate	0.9	36
Deep	1.2	53
Bottom	0.4	10
Weighted Average	1.2	

Considering the small number of bottom samples, the low scatter is not considered to be significant, but the high surface scatter is well documented. Excluding the surface value, the average scatter is 1.0%, identical with the measurement uncertainty. The high surface scatter is likely a reflection of the more variable surface conditions relative to the "mixing averaged" deeper water conditions. This is further supported by the lower average Surface Water  $\Delta$ He values. (Mixing tends to increase  $\Delta$  values. See Chapter 1.)

A more sensitive test of the  $\Delta$  variability lies in the examination of scatter for the isotope dilution samples.

These scatter values are given in Table 11.

TABLE 11  
 AVERAGE SCATTER OF ISOTOPE DILUTION  
 VALUES OVER DIFFERENT DEPTH RANGES

Range	Scatter	
	$\Delta\text{He}$	$\Delta\text{Ne}$
Surface	1.2	1.2
Intermediate	0.6	0.7
Deep	0.8	1.0
Bottom	0.7	0.7
Average	0.8	0.9

Because of the smaller measurement uncertainties ( $\pm 0.4\%$ ) it becomes apparent that there are significant variations inside the depth ranges, particularly in the surface samples. The mean variations assuming a .4% uncertainty for the isotope dilution measurements and a 1.0% uncertainty for the peak-height variations is 0.7% in both cases. It is likely that part of the scatter is caused by the choice of depth-range boundaries. The  $\Delta\text{He}$  and  $\Delta\text{Ne}$  scatters are not significantly different.

Returning to Table 9, two major trends are evident. The first is generally increasing  $\Delta\text{He}$  with depth and the second is increasing  $\Delta\text{He}$  southward. The latter is most strikingly developed in Surface and Bottom Waters, and most weakly developed at Intermediate depths.

The surface trend in  $\Delta\text{He}$  is well documented, if somewhat irregular. This trend must be related to the spatial and temporal meteorological distribution, which will control the distribution and intensity of air injection processes as well as atmospheric pressure. The Intermediate trend is more irregular, and may be an artifact of the different origins of the waters at intermediate depths between the North and South Atlantic (see, for example, Broecker, 1973).

The latitudinal trend in the Deep Water, although not as marked as the surface trend, is somewhat smoother. The larger value at Station 3 may indicate the presence of nonatmospheric  $^4\text{He}$ , but in light of the errors involved further measurements are required before any definitive statement can be made. In Fig. 11,  $\Delta\text{He}$  values for the Deep Water range have been plotted as a function of latitude. The average rate of increase in  $\Delta\text{He}$  is about 0.2% per 1000 km. Examination of the  $\Delta\text{He}$  values for the Bottom Water leaves little doubt that the increase in  $\Delta\text{He}$  in the Deep Water (NADW) is due to an upward flux from the Antarctic Bottom Water (AABW).

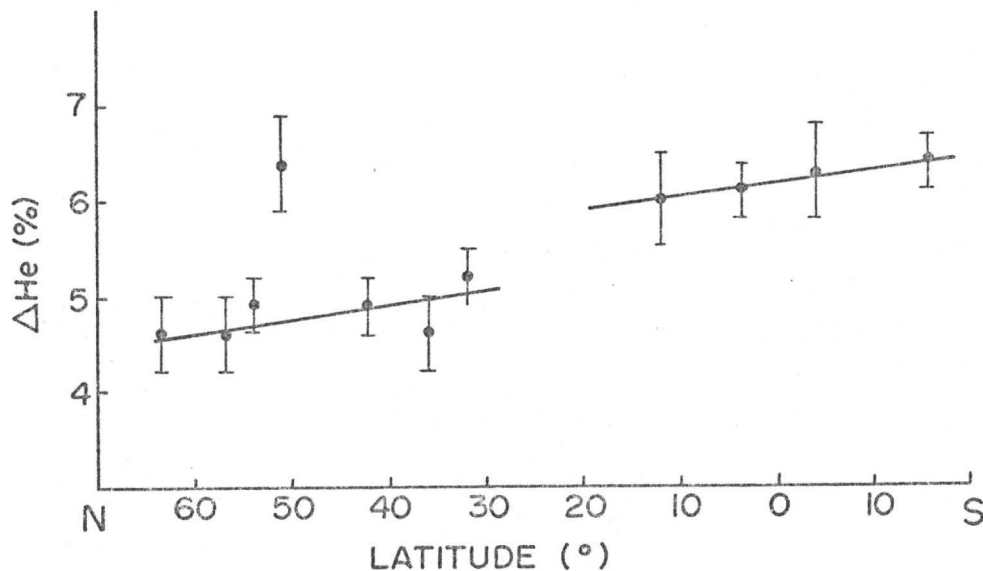


FIG. II : Latitudinal distribution of  $\Delta\text{He}$  in the NADW.

It is possible, using a simple flux balance calculation to estimate the ratio of the vertical diffusivity to the lateral velocity for the region  $12^\circ\text{N}$  to  $16^\circ\text{S}$ . As derived in Appendix 1 for a concentration  $C$ ,

$$\frac{D}{v} = \left(\frac{\partial C}{\partial y}\right) / \left(\frac{\partial^2 C}{\partial z^2}\right) \quad (7)$$

where  $D$  is the vertical coefficient of turbulent diffusion in  $\text{cm}^2 \text{sec}^{-1}$ ,  $v$  is the lateral velocity in  $\text{cm sec}^{-1}$ , and  $y$  and  $z$  are the horizontal and vertical spatial coordinates. From Fig. 11, the mean horizontal  $\Delta\text{He}$  gradient is  $(1.3 \pm .2) \times 10^{-9} \% \text{cm}^{-1}$  between  $12^\circ\text{N}$  and  $16^\circ\text{S}$ . Taking the

difference between the AABW and NADW mean  $\Delta\text{He}$ 's (the South Atlantic Deep and Bottom Water averages) as  $(1.0 \pm .3)\%$  and estimating the "transition layer" thickness from the  $\delta(^3\text{He})$  distributions as 200 m, one obtains

$(\partial^2\text{C}/\partial z^2) = (2 \pm .6) \times 10^{-10} \text{ \% cm}^{-2}$  using the water mass thickness of 2.5 km and assuming no flux through the upper boundary. This yields

$$\frac{D}{v} = 6.5 \text{ cm}$$

in good general agreement with the values obtained by Defant (1961: Fig. 321, p. 681) from temperature and salinity.

Table 12 shows the  $\Delta\text{Ne}$  mean values calculated in the same manner as Table 9. The average values again do not include the GII values, which appear to be systematically low.

TABLE 12

 $\Delta\text{Ne}$  AVERAGES IN THE ATLANTIC OCEAN

Station No.	Latitude ( $^{\circ}\text{N}$ )	Surface		Inter-mediate		Deep		Bottom	
		Avg	$\sigma$	Avg	$\sigma$	Avg	$\sigma$	Avg	$\sigma$
4	54	4.7	0.9	5.2	0.2	5.2	0.4	—	—
27	42	4.4	0.8	4.9	0.7	5.1	0.2	5.1	0.3
GII	36	4.7	0.3	3.4	0.2	3.3	0.7	3.8	—
30	32	5.4	0.6	5.0	0.3	5.3	0.2	5.4	0.4
Average		4.8	0.3	5.0	0.1	5.2	0.1	5.3	0.2

Due to the station spacing it is not possible to determine with confidence any latitudinal trends, but there is a marginal increase in  $\Delta\text{Ne}$  with depth. What is notable, however, is the tendency for the  $\Delta\text{He}$  and  $\Delta\text{Ne}$  values to correlate: a tendency originating from their common air-injected and diffusive origin. A potentially useful approach is to study the saturation anomaly difference,  $\Delta\text{He} - \Delta\text{Ne} \equiv \Delta'\text{He}$  (Craig and Weiss, 1971; Weiss, 1970). This procedure de-emphasizes the correlation and emphasizes the processes which tend to differentiate the two gases. Figure 10 shows the  $\Delta'\text{He}$  profiles for the four isotope dilution stations. The GII profile shows larger variations in  $\Delta'\text{He}$  than any of the other stations. This may be related to the fact that the GII station lies closer to the Western Boundary and thus is representative of less well mixed water masses associated with the Western Boundary Undercurrent (WBUC).

Aside from the GII profile, the  $\Delta'\text{He}$  values generally deviate no more than 1% from zero. In fact, the mean  $\Delta'\text{He}$  value for all 70 samples is 0.1%. Table 13 gives the mean depth distributions of  $\Delta'\text{He}$ . The average given, as in the other tables, is weighted according to the number of samples.

The surface value of 0 for  $\Delta'\text{He}$  is worthy of comment. Considering the mechanisms that are responsible for the transfer of gas between the atmosphere and the sea, the major

TABLE 13

 $\Delta$ 'He AVERAGES IN THE ATLANTIC OCEAN

Station No.	Latitude ( $^{\circ}$ N)	Surface	Intermediate	Deep	Bottom
4	54	-0.8	-0.2	-0.3	—
27	42	0.5	0.5	-0.2	0.2
GII	36	-0.2	-0.7	1.3	0.1
30	32	-0.1	-0.4	-0.1	0.5
Weighted Average		0.0	-0.1	+0.1	0.3

ingassing mechanism is likely air injection by forced dissolution of bubbles (Kanwisher, 1963; Atkinson, 1973) balanced by turbulent and molecular diffusive loss to the atmosphere. As explained in Chapter 1, the resultant  $\Delta$ He and  $\Delta$ Ne values are a product of a dynamic balance between the two processes, the former tending to enrich He due to the lower solubility of helium and the latter tending to enrich Ne because of the lower molecular diffusivity of neon. The observation of  $\Delta$ 'He = 0 for Surface Waters indicates that the two enrichment processes approximately cancel.

As seen qualitatively in the profiles, the  $\Delta$ 'He values tend to be largest in the Bottom Water, likely due to the invasion of AABW into the North-western Atlantic (see,

for example, Eittreim and Ewing, 1972; McCoy, 1968). The Intermediate Water negative value can be explained by subsurface mixing in that the average  $\Delta\text{Ne}$  values are slightly higher than those in the Surface Waters. Mixing will tend to enrich  $\Delta\text{Ne}$  relative to  $\Delta\text{He}$ , thereby driving  $\Delta'\text{He}$  negative.

In the Deep Waters however, there is a discrepancy between the central basin stations (27 and 30) and GII, the boundary station. As suggested earlier, the generally lower values at GII may be explained if one assumes that the WBUC water represents a relatively un-mixed zone of water. If this were the case, GII would be expected to have higher  $\Delta'\text{He}$  values in the Deep Water, which is observed. There is, however, an additional possible mechanism for increasing the  $\Delta'\text{He}$  at the boundary stations: injection of nonatmospheric  $^4\text{He}$  from the crust. The difficulty with this interpretation is that the GII Deep Water  $\Delta\text{He}$  values would be expected to be larger than the central basin stations. Since they are not, the former interpretation appears more likely.

(ii) The distribution of  $\delta(^3\text{He})$

In the North Atlantic Deep Water between  $4^\circ\text{S}$  and  $51^\circ\text{N}$ , there occurs a maximum in the helium isotope ratio anomaly profiles at a depth of about 3000 m. This maximum is deepest,

sharpest and most intense in the north; shoals upward, broadens and weakens southward; and appears to be associated with the Western Boundary Undercurrent (WBUC) because of the fact that no maximum is observed in the central basin stations (27 and 30). Although the sampling at the stations south of the equator was inadequate to define the maximum precisely, it is not unlikely that this feature extends well into the South Atlantic. It is reasonable to infer, then, that this feature originates in the north and flows southward along the Western Boundary.

Away from the area of formation the  $\delta(^3\text{He})$  maximum lies well below the characteristic salinity and oxygen maxima which, according to the terminology of Wüst, mark the Upper (UDW) and Middle (MDW) North Atlantic Deep Water respectively (Defant, 1961; Neumann and Pierson, 1966). One can thus conclude that this feature is part of the Lower (LDW) North Atlantic Deep Water.

At station 3 (51°N) the  $\delta(^3\text{He})$  maximum at 3400 m corresponds to a potential temperature and salinity of 2.2°C and 34.93 ‰, intermediate between the temperature and salinity characteristics of the North-east Atlantic Deep Water\* (NEADW) and the NADW of Lee and Ellet (1967). The  $\delta(^3\text{He})$  maximum lies somewhat below the salinity maximum associated with the NEADW that penetrates the western basin

---

\* Also called the Iceland-Scotland Overflow Water.

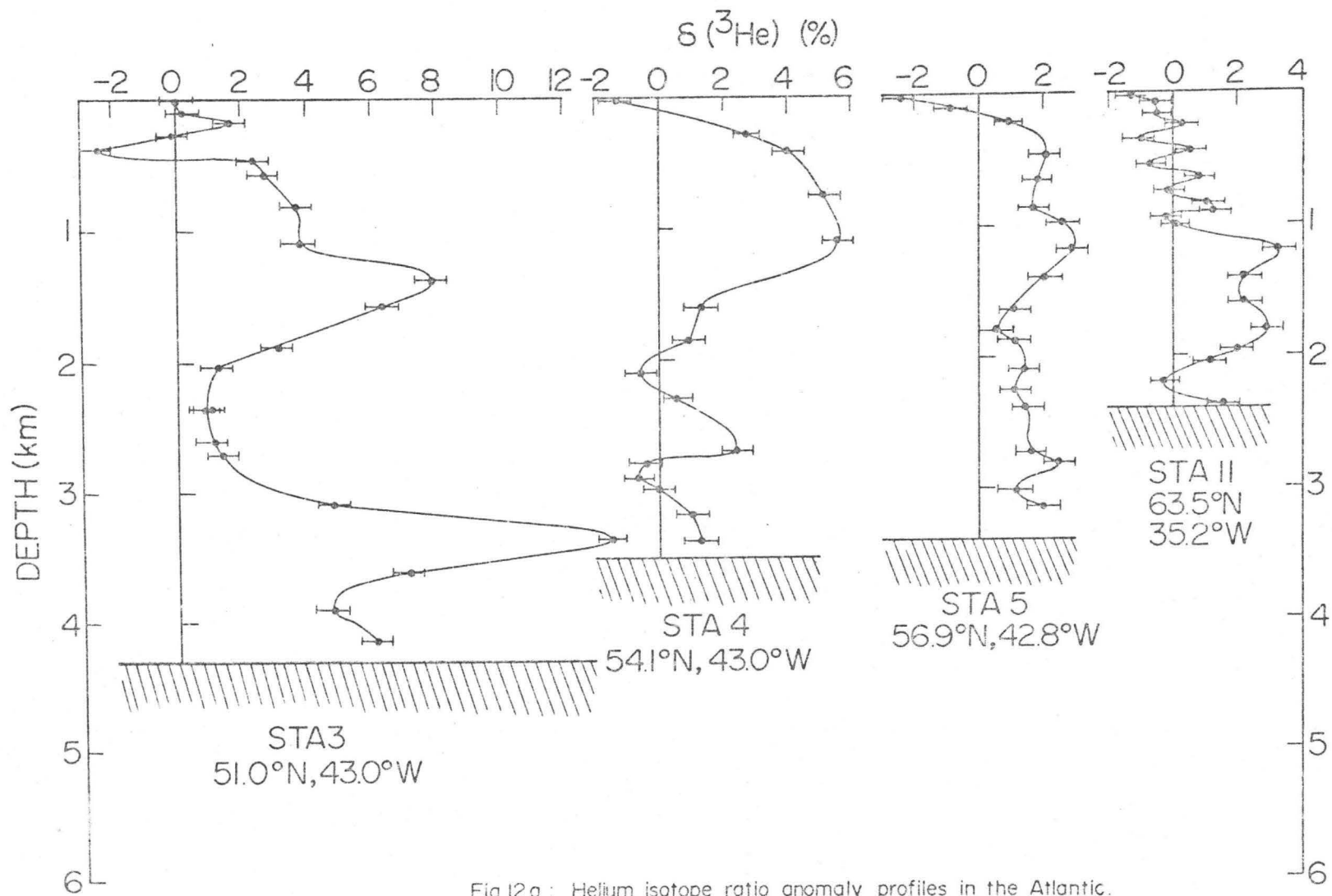


Fig 12a : Helium isotope ratio anomaly profiles in the Atlantic.

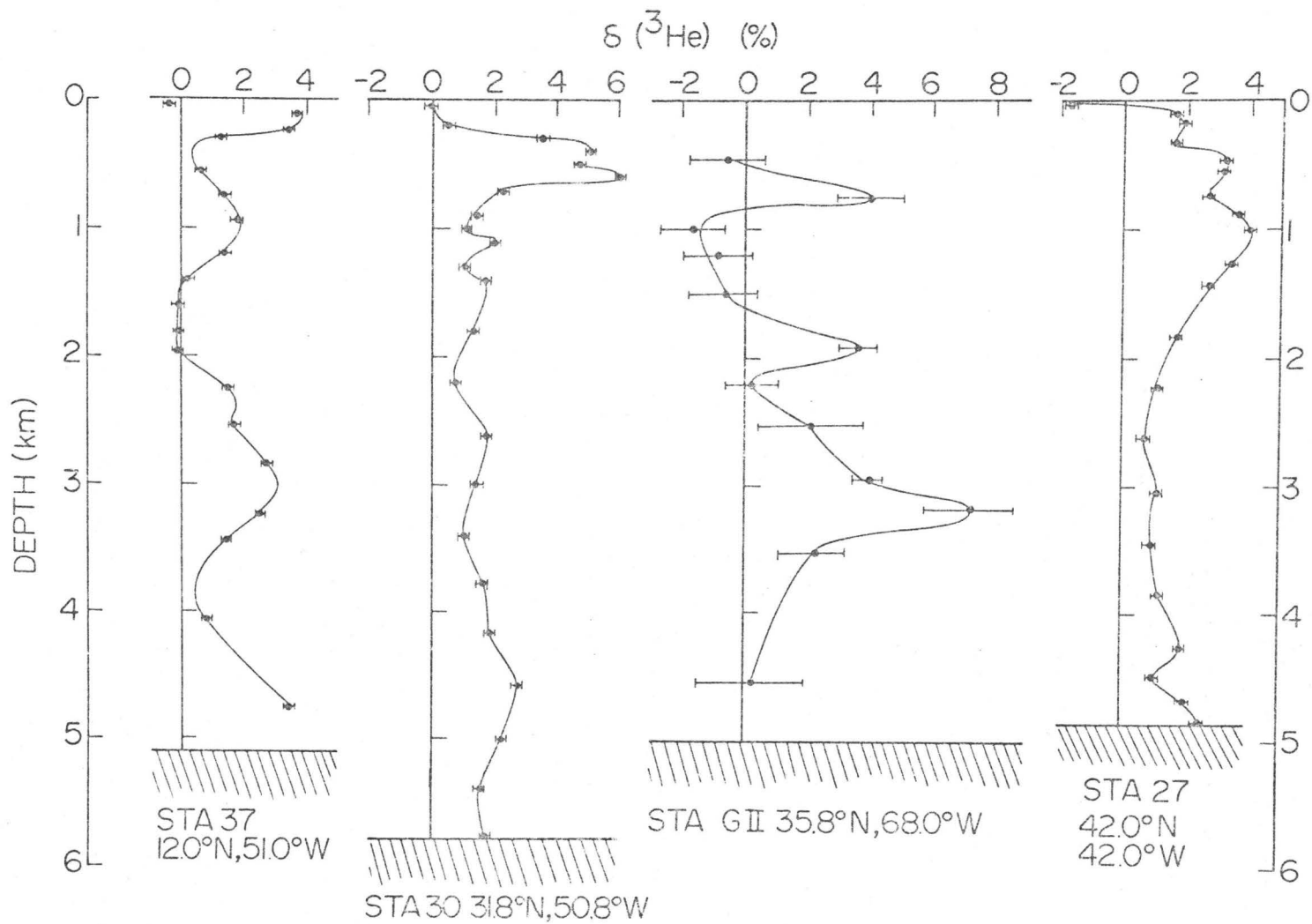


Fig 12b : Helium isotope ratio anomaly profiles in the Atlantic.

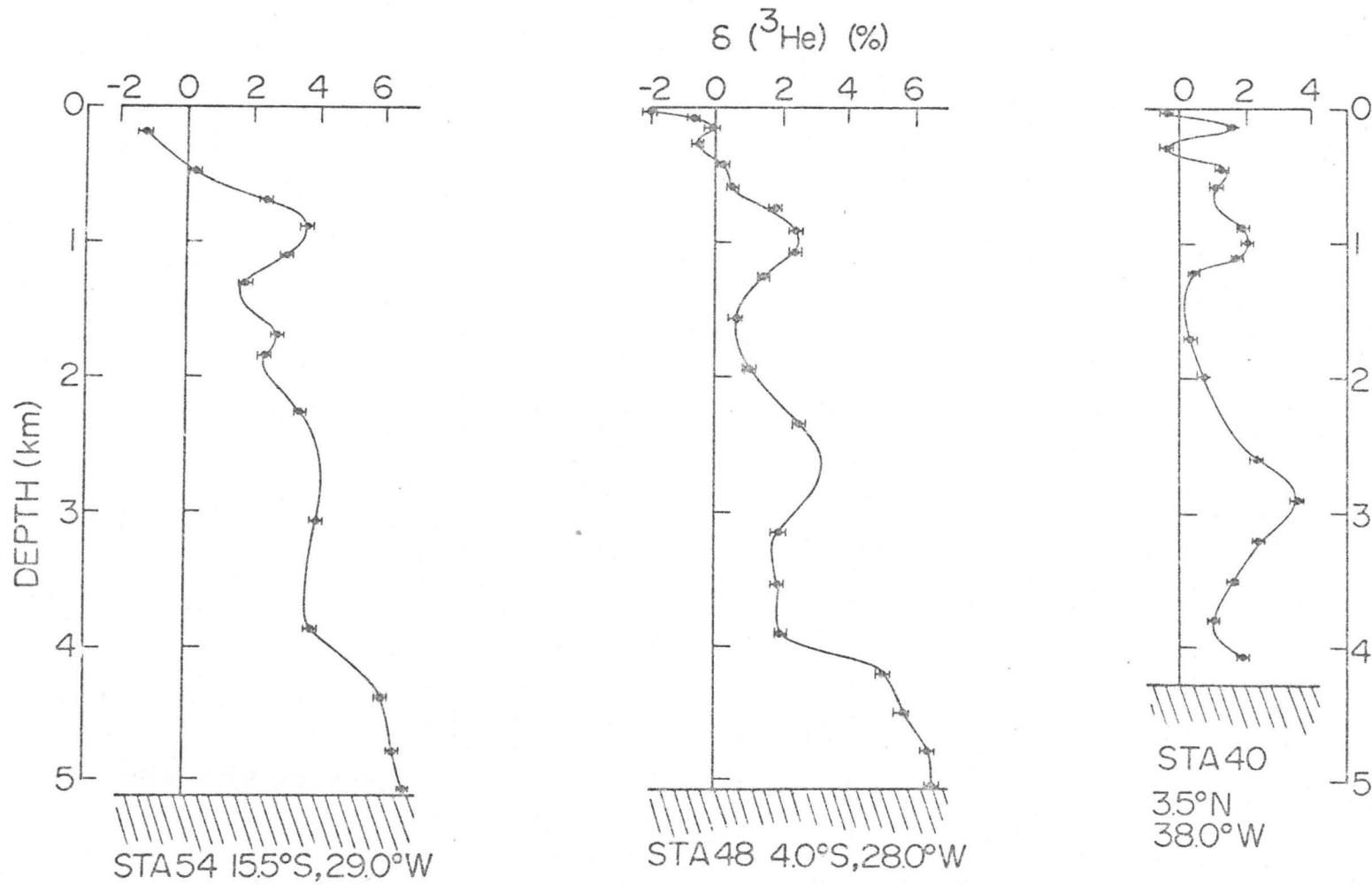


Fig 12c : Helium isotope ratio anomaly profiles in the Atlantic.

through a gap (the Gibb's Fracture Zone) in the Mid-Atlantic Ridge (Worthington and Volkmann, 1965; Lee and Ellett, 1967; Worthington and Wright, 1970: pl 29), but nonetheless above the sill depth imposed by this gap (see, Fleming et al., 1970). It is highly unlikely that this feature is due to in situ decay of tritium for two reasons. First, the measured tritium concentration (Östlund et al., 1974) would require an in situ decay time of 25 years and an initial tritium content of more than 4 T.U.. This is clearly in conflict with existing knowledge about the pre-nuclear era levels of tritium (Craig et al., 1970; Craig and Lal, 1961). Second, the tritium, and therefore the "tritiogenic"  $^3\text{He}$ , would be a core property of the (NEADW) water mass and, therefore, should extend to and be a maximum near the depth of the salinity maximum associated with this water mass.

The close correspondence of the  $\delta(^3\text{He})$  maximum with certain trace element maxima seems significant. This correspondence has been noted for the North Pacific (Jenkins et al., 1972; cf. Spencer et al., 1970; Clarke et al., 1970), for the GII station (Jenkins et al., 1972; Brewer et al., 1972) and at station 3 (Brewer, private communication). The trace element maxima have not been observed at those stations (5, 27, 30) where the  $\delta(^3\text{He})$  maximum has not been observed (Spencer, private communication). This is consistent with interpretations of Lister (1972) and Corliss (1971) as to the role of seawater in the transport of certain properties away

from the site of upwelling mantle material.

The above considerations, and the fact that the  $\delta(^3\text{He})$  maximum near 3000 m is not present north of  $51^\circ\text{N}$ , lends credence to the interpretation that primordial  $^3\text{He}$  is injected into the lower part of the water mass that flows through the Gibb's Fracture Zone.

It is possible, using a simple model, to study and parameterize the physical processes that control the evolution of this maximum after injection into the water column. Assuming a point source injection into an unbounded two-dimensional anisotropic medium, with horizontal and vertical eddy diffusion coefficients  $K$  and  $D$  independent of spatial coordinates  $x$  and  $z$  and time  $t$ , the ratio anomaly distribution may be described by

$$\delta(x, z, t) = \frac{\delta_0}{4\pi\sqrt{KDt}} e^{-\left(\frac{z-z_0}{z^*}\right)^2} e^{-\left(\frac{x-x_0}{x^*}\right)^2} \quad (8)$$

where  $z^* = 2\sqrt{Dt}$ ,  $x^* = 2\sqrt{Kt}$  and where  $\delta_0$  is the initial "strength" of the injection, which occurs at  $t = 0$ . The  $x$ - $z$  plane is perpendicular to the current flow direction, and advection is assumed to predominate over diffusion in the flow direction. Equation ( 8 ), derived in Appendix 1, depicts a "gaussian hill" in  $\delta$ - $x$ - $z$  space whose amplitude decreases as  $t^{-1}$  and whose mean widths increase as  $t^{1/2}$ . Isopleths of  $\delta$  in the  $x$ - $z$  plane will be ellipses.

The assumptions and shortcomings of this model are as follows:

(1) The model assumes a point source injection. If the injection occurs over a non-zero depth range the distribution will not evolve as a gaussian, but as a convolution of a gaussian with the initial distribution. The smaller the depth range, the more closely the convolution function will resemble a gaussian.

(2) The model assumes a diagonal diffusivity tensor. Off-diagonal terms in the diffusivity tensor will produce an apparent spatial dependence for the diagonal terms. Since the horizontal and vertical components of turbulence are to some extent coupled, the off-diagonal terms are non-zero, but too little is known at present to estimate the extent of the problem.

(3) It is likely that the eddy diffusivities are dependent on the spatial coordinates. Since, in terms of the Prandtl mixing length theory, the diffusivity depends on the horizontal and lateral velocity shears, and since these shears vary spatially, the diffusivities must vary.

(4) In addition, it is not at all certain that turbulent diffusion is truly Fickian; i.e., that the linearization of the conservation equations, et cetera are valid (Okubo, 1971; Neumann and Pierson, 1966).

(5) The medium is not unbounded. As the mean width

of the distribution increases, the distribution will begin to "feel" its bounds.

Of the above points, the third is perhaps the most serious, followed by the fifth. The limited amount of data does not permit a more sophisticated treatment, but it is felt that some quite useful information can be extracted, within the constraints of the model.

If the mean width in the vertical direction is determined at two locations (say, 1 and 2, 2 being downstream of 1) and assuming a mean lateral current velocity between the two points, an estimate of a mean  $D/v$  may be obtained according to

$$\frac{D}{v} = [(z_2^*)^2 - (z_1^*)^2] / 4\Delta d \quad (9)$$

as derived in Appendix 1. Using a non-linear least squares fit to the data by iterative minimization of chi-square, a gaussian plus a simple "background" function has been fitted to the maxima at five stations (3, GII, 37, 40 and 48). The resultant estimates of the parameters are given in Table 14, and Fig. 13 compares the calculated curves to the experimental points. It is evident from the reduced chi-square values given in Table 14 and from Fig. 13 that the model is a fair approximation to reality.

TABLE 14  $\frac{D}{v}$  CALCULATIONS FOR THE LDW

Station No.	Latitude	Depth $z_0$ (m)	Width $z^*$ (m)	Amplitude (%)	Area Under Curve** (km %)	Depth Range (m) from to	Background function used	Reduced Chi-square of fit	Distance from WBC† (km)	Distance from Last Sta. (km)	D/v (cm)
3	51°N	3380	231	10.1	4.1	2300 3900	linear	0.8	200		
GII	36°N	3190	276	7.1	3.5	2200 3500	constant	1.1	600	3300	0.2
37	12°N	3000	512	3.2	2.9	1600 3500	constant <sup>††</sup>	0.1	400	3200	1.4
40	4°N	2910	462	3.0	2.5	1700 3200	constant	1.0	800	1700	-0.8
48	4°S	2670	609	2.8	3.0	1600 3150	constant	NC*	700	1400	2.4

Average D/v = 0.8

\* Not calculable, zero degrees of freedom

\*\* Area under the fitted gaussian. See Appendix 1.

† WBC, the western boundary contour, is here defined as the 3000 m contour.

†† Plus a gaussian centred near the oxygen maximum (see text).

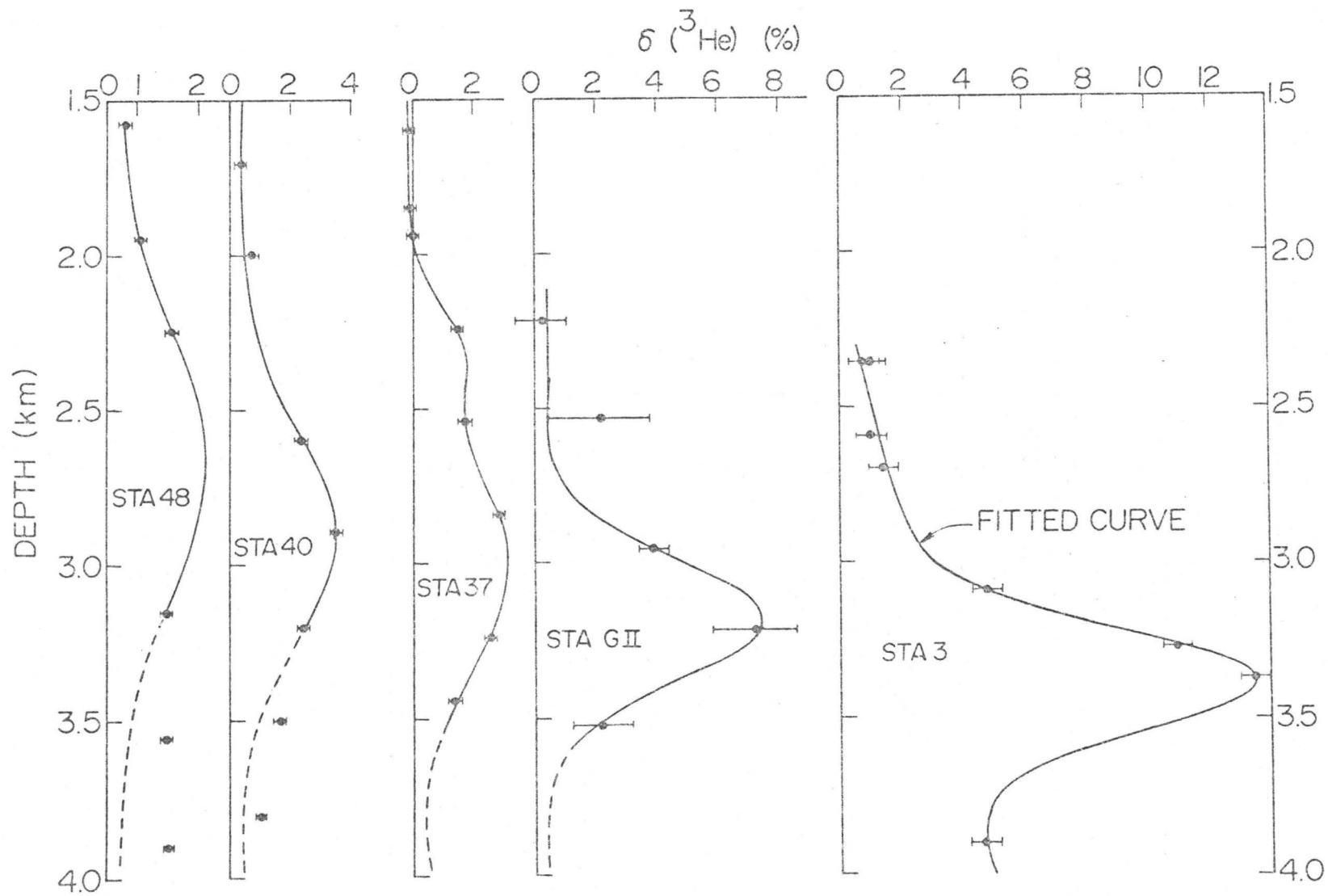


Fig 13 : A comparison of experimental results with calculated curves for the 3km maximum in the Atlantic.

As expected qualitatively, the amplitudes decrease smoothly southward due to vertical and lateral diffusive loss. There are, however, two distinct departures from the expected behaviour. First, between 4°N and 4°S there is an increase in the net excess  $^3\text{He}$  in the water column, as calculated from the area under the fitted curve. This may be explained by noting that the area calculation is unbounded; i.e.,

$$\text{Area} \equiv \int_{-\infty}^{\infty} \delta(z) dz$$

and that the apparent area increase is an artifact of the mean width increase. Naturally the real situation is not unbounded, thereby making the area calculation more meaningless as the mean width increases.

The second departure is a decrease in the mean width between stations 37 and 40, resulting in a negative value for  $D/v$ . Table 14 indicates that station 37 is closer to the Western Boundary than either station 40 or 48. It can be reasonably expected that the gradient Richardson number\*,

$$R_i \equiv g \frac{\frac{\partial \rho}{\partial z}}{\left(\frac{\partial v}{\partial z}\right)^2}$$

increases away from the current core due to decreasing

---

\*  $\rho$  is the potential density and  $g$  the acceleration due to gravity.

vertical velocity shears, resulting in a reduction of the vertical turbulence and turbulent diffusivity. This "reversal" therefore indicates that the diffusivity decreases more rapidly than the horizontal velocity with increasing distance from the current core.

It is apparent from Fig. 13 that the data of stations 40 and 48 show the effects of an upward flux of  $^3\text{He}$  from the AABW below. The depth range over which the least squares fit was performed necessarily did not include the bottom points at these stations as the model does not allow for such a flux. In addition, the fit at station 37 was obtained by assuming an additional gaussian centred at 2300 m. This "shoulder" is likely tritiogenic  $^3\text{He}$  associated with Labrador Sea Water (LSW), since it is at the depth of the oxygen maximum. This  $\delta(^3\text{He})$  maximum is also observed at the GEOSECS II station at a depth of 1900 m (Jenkins et al., 1972). To the south of station 37, the sampling did not permit correction for the LSW bump. The effect of the LSW tritiogenic contribution would be to inflate the mean width estimates and increase the chi-square of fit. Within the limits of the estimates, it is not likely that the former effect will be significant.

Aside from the reversal, the value of  $D/v$  increases downstream, a result not unexpected, due to decreasing velocities and increasing turbulence (Corrsin, 1961). In light of the limitations of the model, however, it is not

possible to ascertain whether this is a real trend or an artifact of one of the assumptions (e.g., no. 4). In an attempt to cancel any variations induced by varying distances from the current core, the values have been simply averaged to obtain

$$(D/v)_{\text{avg}} = 0.8 \text{ cm}$$

for the LDW. Note that this value is an average over the entire depth range of the NADW as well as over 55 degrees of latitude.

Table 15 gives a measure of the total excess  $^3\text{He}$  in the Deep Water column (1500 to 4000 m) obtained by crude graphical integration of the ratio anomaly profiles. For comparison, data is shown from an additional South Atlantic station in the Argentine basin (Jenkins et al., 1972)

TABLE 15

INTEGRATED EXCESS  $^3\text{He}$  IN THE SOUTH ATLANTIC

Station No.	Latitude	Integrated Excess $^3\text{He}$ (% km)
37	12 °N	6.3
40	3.5°N	7.2
48	4 °S	7.4
54	15.5°S	11.5
Argentine Basin	41.5°S	14.5

Despite lateral and vertical diffusive loss from the original primordial  $^3\text{He}$  maximum, the net  $^3\text{He}$  excess increases southward. This increase is likely due to a vertical turbulent diffusive flux upwards from the  $^3\text{He}$  rich AABW, and to back diffusion (opposite to the direction of flow, see Kuo and Veronis, 1970) of excess  $^3\text{He}$  from the Antarctic region.

The Antarctic Bottom Water is characterized by relatively high  $\delta(^3\text{He})$  values. It is separated from the overlying LDW by a frontal zone characterized by a potential temperature gradient maximum at 4000 m at stations 54 and 48. North of the equator, this sharp transitional zone does not occur in the western basin due to appreciable AABW flow into the eastern basin through the Romanche Fracture Zone (Neumann and Pierson, 1966; Craig, 1973). The AABW values of  $\delta(^3\text{He})$  are not inconsistent with this interpretation.

Using a simple flux balance calculation it is possible to estimate  $D/v$  for this frontal zone. It can be readily seen (after Defant, 1961) that

$$\frac{D}{v} = \frac{h(\frac{\partial C}{\partial y})}{(\frac{\partial C}{\partial z})}$$

where  $h$  is the height of the AABW reservoir,  $\partial C/\partial y$  is the average lateral concentration gradient and  $\partial C/\partial z$  is the concentration gradient across the front. Using the data of stations 54 and 48 one estimates  $h = 10^5$  cm,

$\partial C/\partial y = 3 \times 10^{-9} \text{ \% cm}^{-1}$  and  $\partial C/\partial z = 10^{-4} \text{ \% cm}^{-1}$ . The last value was chosen as the best estimate of the concentration gradient at station 48 where the sampling density was highest. This yields

$$\frac{D}{v} = 3 \text{ cm}$$

which compares well with the average value of 4 cm obtained from temperature and salinity (Defant, 1961).

At Intermediate Depths south of 12°N lies a ratio anomaly maximum. Figure 14 shows the tongue-like distribution of this maximum at about 1000 m. This maximum shoals upwards and decreases in intensity northward in a similar fashion to the salinity minimum that characterizes the Antarctic Intermediate Water (AAIW). However, this maximum lies somewhat below the AAIW core (200 m on the average), and corresponds roughly with an inflexion (local minimum) in the dissolved oxygen profile, a maximum in dissolved silicate and a potential temperature minimum. Mann et al. (1973) have traced these extrema back to the Antarctic Convergence where they rise toward the surface and suggest that they must be an advective feature. Broecker (1973) suggests that these features represent "older" Circumpolar Deep Water (CPDW) entrained underneath the

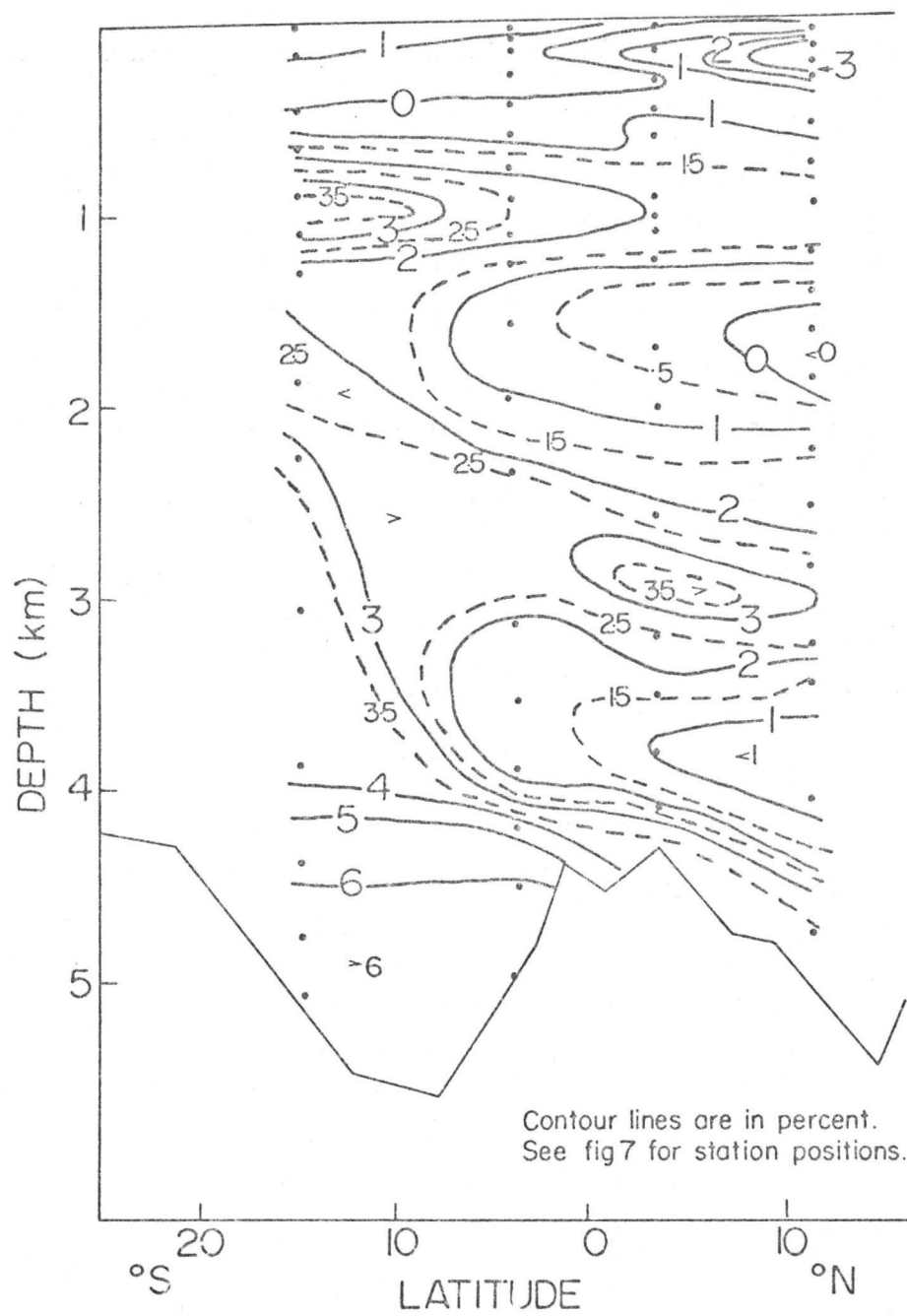


Fig 14 : The vertical distribution of  $\delta(^3\text{He})$  in the South Atlantic.

northward flowing AAIW\*. This latter interpretation implies that the excess  $^3\text{He}$  seen in this feature is primordial rather than tritiogenic. Assuming this to be the case it is possible (after Defant, 1961) to estimate  $D/v$  using

$$\frac{D}{v} = \frac{\frac{\partial C}{\partial y}}{\left(\frac{\partial^2 C}{\partial z^2}\right)^2} .$$

This is achieved by using the three values nearest the maximum in each of the four stations (37, 40, 48, and 54) to estimate the second vertical derivative, and the average lateral gradient in  $C$ . Table 16 summarizes these results. The estimated error in the  $D/v$  estimates is  $\pm 0.5$  cm. The  $D/v$  values exhibit a significant decrease downstream. Using a similar model, Defant (1961: Table 75, p. 177) calculated a value of  $\sim 2.4$  for  $D/v$  at this depth and latitude from salinity data. His data for this depth also shows a weak decrease in  $D/v$ , but not as pronounced as observed in the  $\delta(^3\text{He})$  results. Qualitatively, it would be expected that the Reynolds number of the flow would increase downstream (Corrsin, 1961). What is observed here is either a more rapid decrease in lateral velocity or the increasing effectiveness of lateral eddy diffusion. A model which

---

\* For the sake of convenience, this water mass will be referred to as the Circumpolar Intermediate Water (CPIW) after Broecker (1973).

TABLE 16  
 D/v CALCULATIONS FOR SOUTH ATLANTIC  
 INTERMEDIATE WATERS

Station No.	$\partial^2 C / \partial z^2$ (% km <sup>-2</sup> )	C (%)	$\Delta y$ (km)	$\partial C / \partial y$ (% km <sup>-1</sup> )	D/v (cm)
54	-38	3.6	1280	-7.8 10 <sup>-4</sup>	2.4
48	-27	2.6	1390	-4.3 10 <sup>-4</sup>	1.5
40	-30	2.0	1720	-1.2 10 <sup>-4</sup>	0.5
37	-19	1.8			

accounts for lateral eddy diffusivity (Appendix 1) gives

$$[D + (\frac{\partial^2 C}{\partial y^2}) / (\frac{\partial^2 C}{\partial z^2}) K] = (\frac{\partial C}{\partial y}) / (\frac{\partial^2 C}{\partial z^2}) \quad (11)$$

where K is the lateral diffusion coefficient. Since  $\partial^2 C / \partial y^2$  is positive and  $\partial^2 C / \partial z^2$  is negative, an estimate by the previous, simpler model will yield an underestimate of D/v. The effect of an increasing K would be a decreasing estimate of D/v by the first model, as is seen.

The presence of tritium at this depth would lead to in situ production of <sup>3</sup>He, thereby decreasing the lateral gradient and thus the estimate of D/v. However, there will be diffusive and decay loss of tritium downstream, resulting

in a decrease of the in situ production term and thus resulting in an apparent increase in D/v downstream. In order to explain the observed pattern by decay of tritium, the tritium concentration must increase downstream, despite diffusive and decay losses. Qualitatively this is in agreement with the observation of Brown (1970) and Taylor (1971) of the general decrease of tritium levels in precipitation since the early 1960's, but it is quantitatively unsound. To explain the excess  $^3\text{He}$  at 1000 m at station 54 ( $\delta(^3\text{He}) = 4.8\%$ ) one would require a tritium content of at least 10 T.U.\*, ignoring any diffusive and mixing loss of  $^3\text{He}$  or tritium. This is in clear disagreement with the expected (Dockins et al., 1973) and measured (Michel and Williams, 1973) tritium concentration in Sub-Antarctic Surface Waters. In addition, if the  $^3\text{He}$  were tritiogenic, a tritium maximum and a corresponding  $\delta(^3\text{He})$  maximum would be expected in the AAIW core where the salinity has been lowered by the high tritium surface precipitation. The evidence suggests, therefore, that this  $\delta(^3\text{He})$  maximum is a result of the entrainment of CPDW by the AAIW jet, as first suggested by Broecker (1973) from other considerations.

Figure 14 shows the vertical distribution of the  $\delta(^3\text{He})$  from 16°S to 12°N. It should be noted that the data

---

\* assuming a lateral advection velocity of 5 cm (see, Defant, 1961).

are not corrected for in storage decay of tritium; but the corrections are not likely to alter the general pattern. In addition, the contours are not defined unambiguously by the sampling (indicated by the dots in the diagram); but where there is ambiguity, additional hydrographic information has been used to draw the curve. Thus, the figure must be regarded as a preliminary representation of general trends, the details of which will likely change as more information is acquired.

Figure 14 clearly shows the intruding tongues of high  $\delta(^3\text{He})$  from the south at 1000 m and greater than 4000 m depths, and the LDW maximum from the north. At 100 m a shallow  $\delta(^3\text{He})$  maximum appears in the North, at about the same depth as the shallow salinity maximum characteristic of the Subtropical Underwater. It is likely that this shallow maximum is tritiogenic but since tritium information is presently unavailable at these locations, it is not possible to extract quantitative information.

(iii) Tritium-helium dating: concepts

Before discussing the "Tritium-Helium Ages" calculated for the North Atlantic stations, it would be advantageous to explore the characteristics, assumptions, and difficulties associated with this method of dating water masses.

A rather naïve approach is to suppose that a water parcel, after gas equilibration with the atmosphere, sinks below the surface at  $t = 0$ .  ${}^3\text{He}$  will then accumulate in the water parcel as a decay product of tritium ( ${}^3\text{H}$ ) which decays with a half life of 12.262 years. Measurement of the excess  ${}^3\text{He}$  attributed to in situ decay of the tritium, combined with determination of the amount of tritium yields an age

$$\tau = 17.69 \log_e \left[ 1 + \frac{N({}^3\text{He})}{N({}^3\text{H})} \right] \quad (12)$$

The expression is independent of the initial tritium concentration, and  $N({}^3\text{H})$  and  $N({}^3\text{He})$  are the number of tritium and excess  ${}^3\text{He}$  atoms respectively at the time of sampling. The value of  $N({}^3\text{He})$  may be determined by measurement of the concentration and isotope ratio of dissolved helium and subtraction of the "expected" helium from that amount. Since what is measured is the helium isotope ratio anomaly and the helium concentration, Eq. (12) is more aptly expressed as

$$\tau = 17.69 \log_e \left\{ 1 + 0.0542 \frac{\delta'({}^3\text{He})}{T} C(\text{He}) \times 10^5 \right\} \quad (13)$$

where  $T$  is the tritium concentration in T.U. and  $C(\text{He})$  is the helium concentration in cc STP  $\text{Kg}^{-1}$ . Eq. (13) is not strictly correct in that it does not account for the fact that the air-injected component of helium has  $\delta'({}^3\text{He}) \neq 0$ .

For typical values of  $\Delta\text{He}$  ( $< 10\%$ ) this correction will be of the order of 0.1% to the age. Since, in this present study the  $\delta'(^3\text{He})$  values are known only to 0.2%, and since this uncertainty represents an uncertainty in the age of greater than 2% ( $\delta'(^3\text{He}) < 10\%$ ), this consideration is not necessary here.

It is necessary, in the determination of the amount of  $^3\text{He}$  attributable to tritium decay to preclude or account for the presence of nonatmospheric helium. Specifically, one must be aware of the possible presence of primordial  $^3\text{He}$  and  $^4\text{He}$ , and radiogenic  $^4\text{He}$  from U and Th decay. Since the typical terrigenous flux ratios of ( $^3\text{He}/^4\text{He}$ ) are from five to ten times atmospheric (see Chapter 4), it is likely that the  $^3\text{He}$  component will be more important than the  $^4\text{He}$  component. In a study of the upper few hundred meters, and perhaps even the upper kilometer of the water column this is not likely to cause difficulties, but aside from the "safe" areas, a detailed three-dimensional study must be made to obtain meaningful results.

The model does not account for diffusive loss of tritium and  $^3\text{He}$  from the "water parcel". While there is no reason to assume that the turbulent diffusivities of both properties are exactly the same (Okubo, 1971; Neumann and Pierson, 1966), limited applications suggest that they are not dissimilar for other properties (Craig, 1969; Munk, 1966; Wyrski, 1962). Since the age depends on the ratio of the

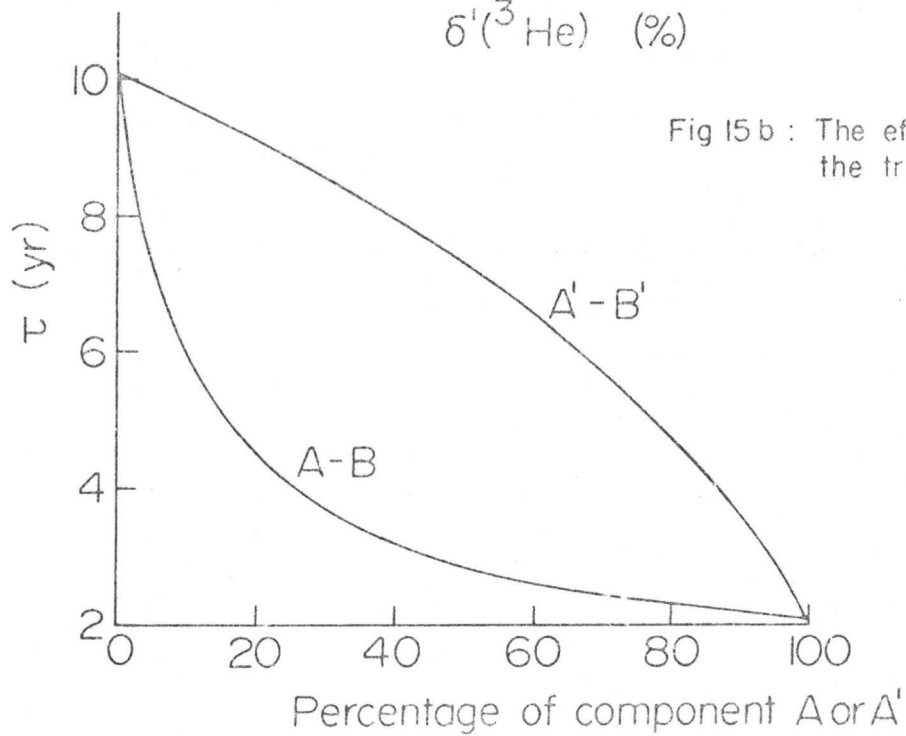
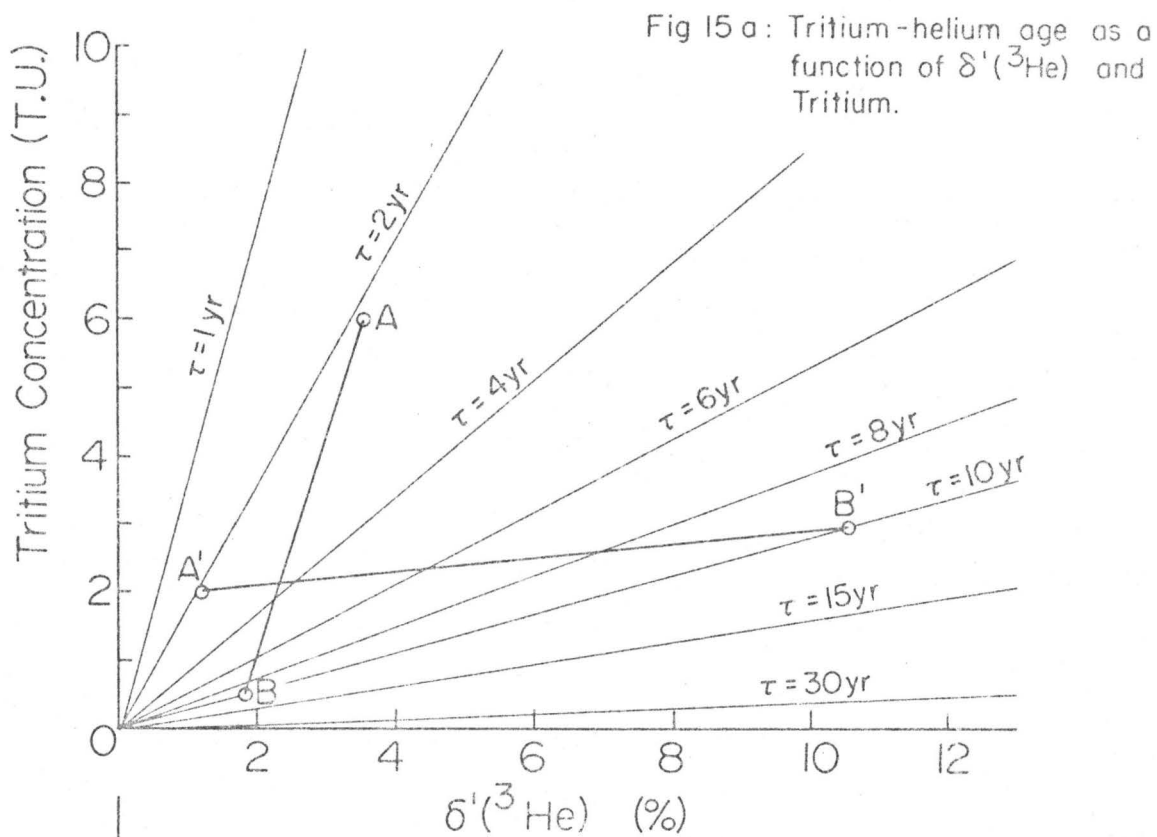
concentrations, diffusive loss to an environment where  $\delta'(^3\text{He}) = 0$  and  $T = 0$  should not alter the age, at least to the first order.

In addition, care must be taken in interpreting a T-He age in that it will be an "average age" due to mixing; an average which is weighted in favour of the higher tritium component. To illustrate this, let us study a simple, binary system. Figure 15a shows the T-He isochrons as a function of  $\delta'(^3\text{He})$  and  $T$ . The isochrons are calculated from Eq. (13) assuming an average helium concentration of  $4.0 \times 10^{-5}$  cc STP  $\text{Kg}^{-1}$ . The line A-B indicates a mixing subrange between water types A and B, characterized by tritium concentrations,  $\delta'(^3\text{He})$  and ages as given in Table 17.

TABLE 17

## AN ILLUSTRATION OF T-He AGE MIXING

	A	B	$\frac{1}{2}(A+B)$
T (T.U.)	6.0	0.5	3.25
$\delta'(^3\text{He})$ (%)	3.5	1.8	2.6
$\tau$ (y)	2.1	10.2	2.8



As can be seen from the Table 17, and from Fig. 15b, the mixing is not a linear process. A'-B' in Figs. 15a and 15b represents another case, this time with the older water having the higher tritium content. Again the non-linearity is present, but in the opposite sense. Even when the tritium concentrations are equal, the mixing curve is non-linear due to the logarithmic nature of the age function.

(iv) Tritium-helium age dating: results

Tritium-helium age profiles are given in Table 7 and Fig. 16. In every case the T-He ages increase with depth from near-zero surface values. In the northern-most stations there is also a tendency for the age to decrease near the bottom, intimating the presence of relatively "new" bottom water, likely from the Denmark Strait (Mann, 1969).

At station 11 (63.5°N) the upper 1000 m shows a complex interfingering of water masses indicated by age oscillations about a mean age-depth gradient of 1.5 y/km. At 1000 m lies a relatively well-documented age minimum overlying a sharp age-depth gradient. This minimum can be reasonably interpreted as an advective core. It corresponds to a potential temperature of 3.7°C, a salinity minimum of  $\sim 34.90\%$ , and a  $\sigma_\theta$  of 27.77, indicating that it is likely Labrador Sea Water (Lee and Ellett, 1967; Lazier, 1973). Assuming an "area of formation" where the 27.78  $\sigma_\theta$  horizon

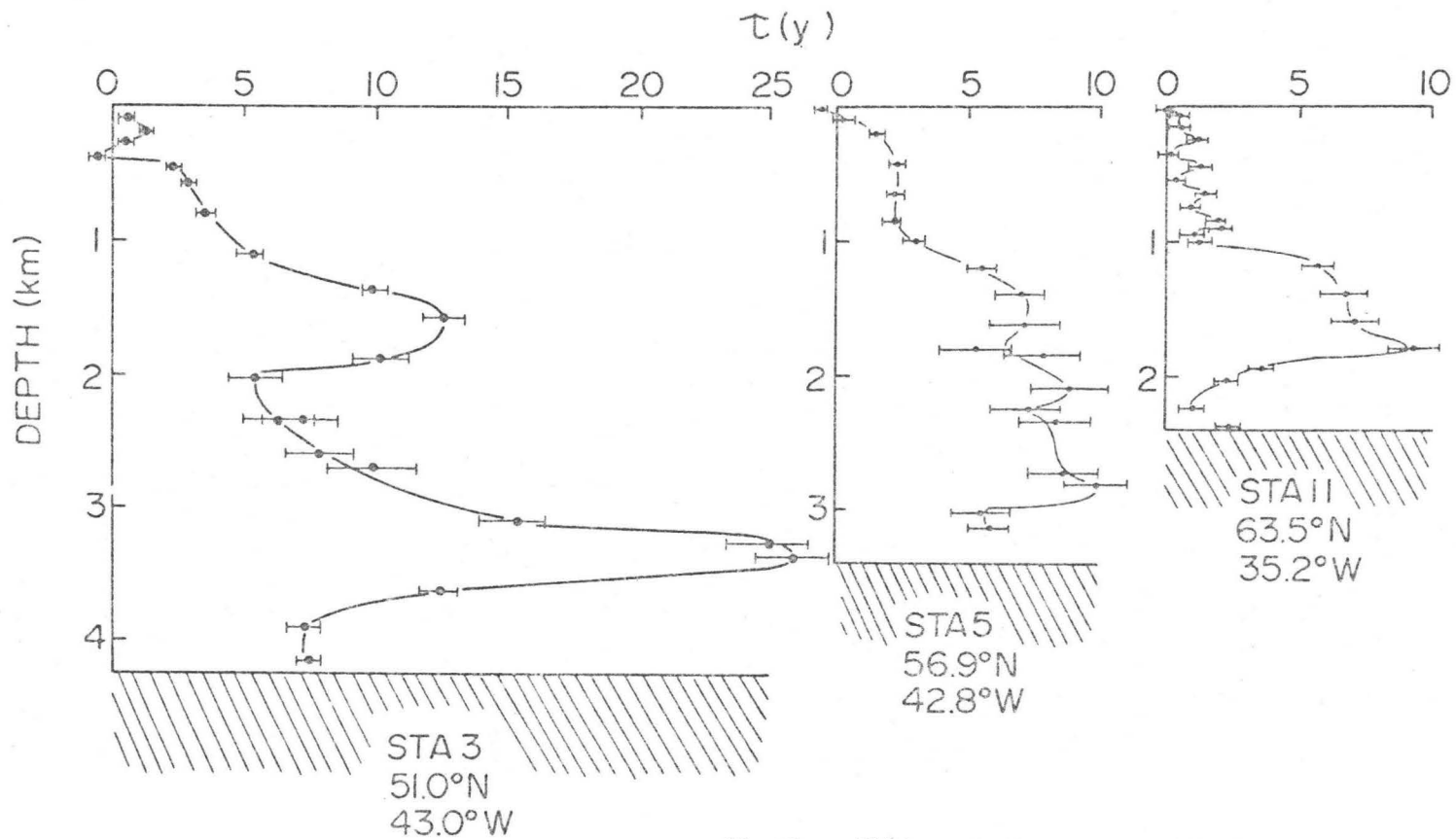


Fig 16a : Tritium-helium age profiles in the North Atlantic.

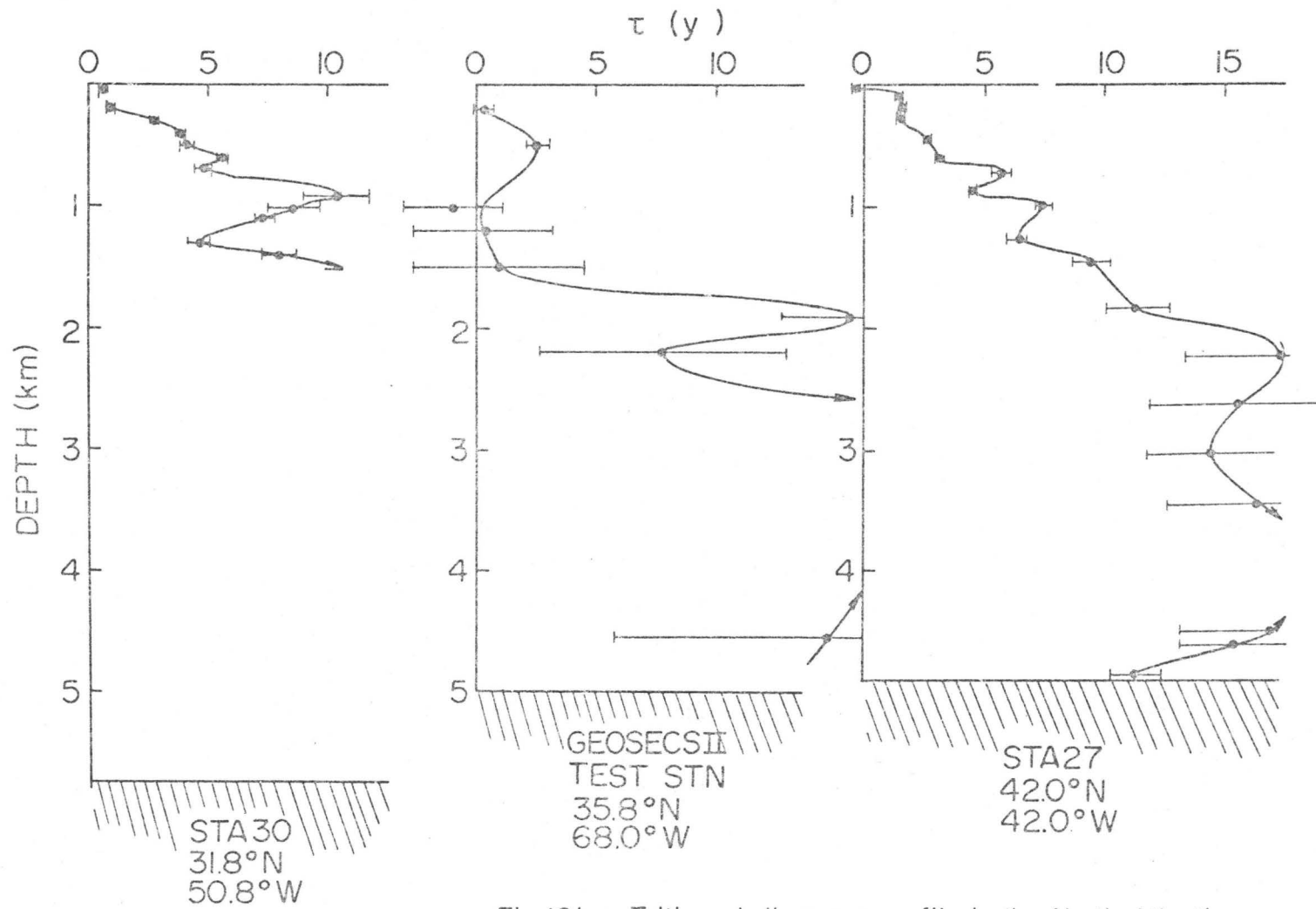


Fig 16b : Tritium-helium age profile in the North Atlantic

exhibits a potential temperature minimum (Lazier, 1973: near 58°N, 52°N) one can calculate a mean velocity of spreading of  $3 \text{ cm sec}^{-1}$ .

Below the LSW at station 11 the age increases to a maximum at 1800 m, corresponding to the salinity maximum associated with the NEADW that has penetrated the western basin through the Gibb's Fracture Zone (Lee and Ellett, 1967; Worthington and Wright, 1970). With the exception of the 1800 m sample the oxygen content and T-He age covary between 1200 and 2050 m. That this correlation is a result of mixing rather than in situ oxygen consumption is indicated by the fact that the T-He age does not correlate well with the apparent oxygen utilization\*. The age maximum at 1800 m may be partly due to primordial  $^3\text{He}$ .

Underlying the NEADW is an age minimum at 2200 m indicating the presence of new bottom water (NWABW after Lee and Ellett, 1967). What is remarkable is that the minimum lies above the depth of the salinity, silicate and potential temperature minima associated with this water mass (Mann, 1969, 1973; Grant, 1968). This perhaps suggests the presence of some primordial  $^3\text{He}$ , but it is still possible to set an upper limit to the age of this water at 1 y.

Station 5 (57°N) in the upper 1500 m, shows a much smoother  $\tau$  profile than station 11. The T-He age increases

---

\* The saturation anomaly of oxygen.

from a slightly negative value at the surface (to be discussed later) to an essentially isochronous layer of  $\sim 2$  y age from 500 m to 900 m. This layer is over 400 m thick and corresponds to a potential temperature of from 3.4 to 3.6°C and  $\sigma_\theta \sim 27.77$ . It is therefore likely that this represents the characteristic LSW. The implication of the 2 y age is that the mean velocity of spreading is  $1 \text{ cm sec}^{-1}$ . This conflicts somewhat with the value obtained for the LSW at station 11, and the question arises as to whether the difference is real (i.e., that the water has advected more rapidly to station 11, perhaps along the western boundary) or is an artifact of the dating method. Although it is possible that the  $\tau$  profile at station 5 may have been altered by mixing or by a diffusive flux from below, the thickness of the layer and the constancy of the age in the layer suggests that this is unlikely. In general one should suspect those results which are obtained in areas where there is a weak indication of a particular water type. It is more reasonable to suspect the LSW age at station 11 of having been lowered substantially by mixing and exchange with overlying younger waters.

In addition, the concept of a "straight-line spreading velocity" implies steady-state, continuous formation of the water type. Lazier (1973) has concluded that formation is seasonal, and it is likely, considering the thickness of the isochronous layer, that the "renewal" is not complete each

year. In fact, a mean residence time of 2 y is not unreasonable in that it assumes about 50% renewal every winter.

Between 1000 and 1500 m the T-He age increases from about 2 y to about 7 y, below which it increases more slowly to 10 y at 2800 m. This layer of older water (below 1500 m) is the intruding NEADW, as it corresponds to a salinity maximum (see, Worthington and Wright, 1970: pl. 27). Typical ages in this water mass are comparable or greater than those seen for the NEADW at station 11, indicating that the apparent ages are being eroded as a result of mixing with younger NWABW (underneath) and LSW (above).

Underlying the NEADW, separated by a relatively abrupt transition in the T-He ages lies the NWABW, with an apparent age of  $\sim 6$  y. It is clear that this represents an upper limit on the true age in that both mixing (with the older, overlying NEADW) and primordial  $^3\text{He}$  addition tends to increase the age.

At station 3 (51°N), at a depth of about 400 m lies a  $\tau$  minimum, indicating the presence of younger water. It corresponds with a salinity minimum, nutrient minimum and oxygen maximum, the last being in accord with the low value of  $\tau$ . The fact that this age is significantly negative is somewhat disturbing and deserves further comment.

It should be noted that all surface samples (shallower than 30 m) yield negative ages, a result that is unlikely if

the "zero point" of the age calculations were valid. This indicates that the helium solubility isotope fractionation factor determined by Weiss (1970) may be slightly in error. Recent measurements on freshwater samples from Lake Erie suggest that the factor is 0.982 (Clarke, private communication). However, at present the value of Weiss (op cit) has been used, with the provision that a redetermination may require a revision of the calculated ages. The uncertainties imposed by the assumptions inherent in the T-He method probably outweigh the error, so the main arguments will not be altered. However, for more detailed studies, a redetermination of the fractionation factor is mandatory.

Returning to the  $\tau$  data of station 3, the T-He age minimum is underlain by a relatively sharp increase to 2.3 y, followed by a more gradual increase to 5.2 y at 1100 m. At 1100 m there occurs a slight temperature and salinity maximum, probably corresponding to traces of the Mediterranean Water (MW). The age here represents a lower limit estimate in that the MW, in flowing across the Atlantic has suffered considerable mixing with both overlying and underlying water. It is a lower limit because the younger overlying water is bound to have more influence on the mixing age due to the higher tritium levels in shallower water. With this in mind it is possible to estimate an upper limit to the straight-line spreading velocity to be  $2 \text{ cm sec}^{-1}$ . This is in qualitative agreement with the estimate of  $2 \text{ cm sec}^{-1}$  by Defant (1961: p. 692) from salt balance calculations.

Below 1100 m the T-He age increases to a maximum of 12.5 y at 1600 m and then decreases to a minimum of 5.2 y at 2100 m. Below this minimum the age increases rapidly due to primordial  $^3\text{He}$  injection. Due to the upward flux of primordial  $^3\text{He}$ , the true minimum probably lies below the observed minimum, possibly at about 2500 m where the salinity maximum associated with the NEADW occurs. Since the history of the NEADW involves intense mixing (Steele et al., 1962) with overlying, younger, high tritium water, this age estimate represents neither an upper nor a lower limit to the true age.

The NWABW, characterized by decreasing silicate, temperature and salinity (Mann, 1969; Lee and Ellett, 1967) appears near the bottom with an age of  $\sim 7$  y. This age, as discussed for station 5 represents an upper limit to the true age, corresponding to a lower limit of  $\sim 1 \text{ cm sec}^{-1}$  to the spreading velocity.

Station 27 ( $42^\circ\text{N}$ ) exhibits a 200 m thick layer of 1.5 y water, the top of which corresponds to a salinity maximum at 102 m. Lying just below the seasonal thermocline, it is not likely that this is a remnant of the previous winter's surface water. It seems reasonable that this water is Subtropical Mode Water (after Warren, 1972; Masuzawa, 1969) that has advected from the south. Assuming an area of formation near  $35^\circ\text{N}$ ,  $60^\circ\text{W}$  (Warren, 1972) a mean spreading velocity of  $3.7 \text{ cm sec}^{-1}$  is obtained.

At 950 m lies a salinity and potential temperature maximum which may be attributed to MW. Using the measured age of 7.5 y for this depth, an upper limit to the spreading velocity of  $1.3 \text{ cm sec}^{-1}$  is obtained. As can be expected from the fact that this station shows stronger indications of the MW the T-He age is greater, resulting in a somewhat better estimate of the spreading velocity. The oscillatory nature of the  $\tau$  profile indicates the intrusion of relatively old water into the water column, the minima above and below being induced features similar to the observations of temperature and salinity above and below the MW core (See Katz, 1970).

Below the MW the T-He age increases to about 16 y and remains constant within experimental error between 2000 and 3500 m. Between 3500 and 4300 m the age exceeds 20 y. These ages are almost certainly not real, especially the largest ones, due to the probable primordial  $^3\text{He}$  contribution. At the bottom, the age decreases again. Relatively high silicate concentrations at these depths suggest an appreciable admixture of AABW in the bottom water of this station (Mann et al., 1973; Metcalf, 1969) so the T-He age ( $\sim 11$  y) is difficult to interpret.

At station 30 ( $32^\circ\text{N}$ ) the shallowest sample measured lies at the base of the seasonal thermocline, and has an age of 0.6 y. Since sampling was done in late summer, this age is consistent with formation in late winter. Below this depth the T-He age increases smoothly from 0.9 y at 200 m to 4 y at

400 m. This age range is associated with a nearly isothermal, isohaline 200 m thick layer called the Subtropical Mode Water (Warren, 1972; Masuzawa, 1969) or the "18° Water" (Worthington, 1959). Warren (op. cit.) observes that the characteristics of this water mass vary little despite meteorological fluctuations, and proposes that the water mass is only partly renewed annually and then only late in the winter. The age structure seen here is in good agreement with this interpretation, but in addition shows that this water mass is not totally mixed vertically. The mean residence time for this water mass is  $\sim 2.5$  y, which accounts for the insensitivity of the SMW to yearly meteorological fluctuations: the water characteristics must be the result of an almost three-year averaging process.

The T-He age increases below this layer to a maximum of 10.4 y at 900 m, where there is a weak silicate maximum. It is therefore likely that the age maximum is a result of the northward penetration of the intermediate depth, high  $\delta(^3\text{He})$  water from the South Atlantic. Below the silicate maximum at 1050 m lies a (local) salinity and temperature maximum characteristic of MW. Interpolation of the  $\tau$  profile reveals an age of 8.2 y, corresponding to a spreading velocity of  $1.6 \text{ cm sec}^{-1}$ , in good agreement with the values of 1.3 and  $2.0 \text{ cm sec}^{-1}$  obtained at stations 27 and 3.

The age minimum at 1300 m of 4.5 y is strongly suggestive of an advective core, but there are no corresponding extrema in any other properties, aside from a slight local minimum in salinity. Lacking further evidence, it is not possible to attribute a source to this feature, but it warrants further attention in future studies. Below the minimum the T-He age increases rapidly to a point where, below 1500 m, calculation is not possible due to low tritium levels.

The hydrography of the GEOSECS II station (36°N) has been discussed elsewhere (Spencer, 1972) and the tritium data used for the age calculations are from Roether and Münnich (1972). The SMW is here represented by the 200 and 500 m ages, which are in good qualitative agreement with the more precise values at station 30. At 1200 m the MW is represented by an age of  $0.4 \pm 2.8$  y, distinctly lower than the values obtained at stations 3, 27, and 30. The indications of MW at this station are very weak, and consist merely of "extra scatter" in the T-S relationship (Spencer, 1972). The age estimate ( $< 3.2$  y) is in agreement with the expected trend in age due to mixing with younger overlying water. The conclusion to be drawn here is that the age calculations in a badly eroded water mass should not be taken seriously.

The single point maximum in the  $\tau$  profile indicates an age of about 16 y for the LSW indicated by a silicate minimum at 1900 m depth (Spencer, 1972). However, a cursory examination of the  $\delta(^3\text{He})$  profile suggests that there may be an appreciable contribution of primordial  $^3\text{He}$  to this age. It is possible to visualize a 1% contribution to the  $\delta'(^3\text{He})$ , resulting in a corrected age of about 12 y. Below this depth lies a T-He age minimum which may correspond to the upper portion of the NEADW. Due to the probable influence of the upward flux of primordial  $^3\text{He}$  from the LDW, a crude upper limit may be  $7.8 \pm 5$  y for the age of this water mass.

(v) Summary of Atlantic results

The results of 194 He measurements show that the average excess helium relative to solubility ( $\Delta\text{He}$ ) is 5.4%, with North Atlantic and South Atlantic averages of  $4.9 \pm 0.2\%$  and  $6.3 \pm 0.2\%$  respectively. The difference between the South and North Atlantic averages is significant and may be attributed largely to the AABW which acts as a source of excess  $^4\text{He}$ .

Precise isotope dilution measurements of neon concentrations at four North Atlantic stations reveal that neon is on the average  $5.0 \pm .1\%$  supersaturated, with a slight tendency for increasing  $\Delta\text{Ne}$  with depth. The average surface  $\Delta\text{Ne}$  is 4.8%. Comparison of both  $\Delta\text{He}$  and  $\Delta\text{Ne}$  for

these four stations indicate that there may be a difference between the "central basin" stations (27 and 30) and the western boundary station (GII) in that the former show higher  $\Delta\text{Ne}$  values. This difference is probably due to more intense mixing in the central basin, which would tend to increase  $\Delta\text{He}$  and  $\Delta\text{Ne}$  values (see, Chapter 1).

An analysis of the variability of  $\Delta\text{He}$  and  $\Delta\text{Ne}$  values at all depths indicates that significant variations, of the order of 0.7%, occur within particular depth ranges, and that the variations in the upper 500 m are significantly larger than in the deeper water.

Helium isotopes have been measured at eleven stations in the Western Atlantic (see Fig. 7) between  $15.5^\circ\text{S}$  and  $63.5^\circ\text{N}$ , and two sources of nonatmospheric excess  $^3\text{He}$  can be discerned: a primordial component and a component produced by in situ decay of man-made tritium. The vertical and horizontal distribution of the primordial component has been studied in the Lower North Atlantic Deep Water (LDW), the Antarctic Bottom Water (AABW) and the Circumpolar Intermediate Water (CPIW) using simple models. The tritium component has been studied at the six North Atlantic stations and tritium-helium ages have been determined for the Labrador Sea Water (LSW), Mediterranean Water (MW), and the Subtropical Mode Water (SMW).

With the primordial component the LDW has been studied using a simplified Fickian-Diffusive Model. By fitting the 3 km  $\delta(^3\text{He})$  maximum to a gaussian at five stations (3, GII, 37, 40, and 48) a ratio of the vertical diffusivity to the current velocity ( $D/v$ ) has been obtained and is seen to vary from 0.2 cm in the north to 2.4 cm in the south with an average value of 0.8 cm. Using a box model flux-balance calculation for the AABW, a value of 3.0 cm was determined for  $D/v$ , in good agreement with the value obtained by previous workers from salinity and temperature considerations. A similar calculation, applied to the CPIW, yielded a value that decreased from 2.4 cm at  $\sim 10^\circ\text{S}$  to 0.5 cm at  $\sim 8^\circ\text{N}$ . The higher value is in agreement with other measurements and the decreasing trend is believed to be due to increasing lateral diffusivity.

## CHAPTER 4

### THE PACIFIC: RESULTS AND DISCUSSION

#### A. Results

The concentrations of helium, neon, krypton and xenon, together with relevant hydrographic data<sup>†</sup> are given in Table 18. Saturation anomalies are given for helium and neon relative to the solubility data of Weiss (1971) and are defined by

$$\Delta(\%) = \frac{C - C^*(\theta, S)}{C^*(\theta, S)} \times 100\% \quad (1)$$

where, as before, C is the measured concentration and  $C^*(\theta, S)$  is the solubility concentration at the potential temperature and salinity of the sample. Since no precise, reliable seawater solubility data have yet been published for krypton and xenon, saturation anomalies have not been given for these gases. The helium isotope ratio anomaly,  $\delta(^3\text{He})$ , has been defined previously (Eq. (3)). In addition, a quantity defined as the "Excess Helium Anomaly" is given, and as in the previous chapter, is defined by

---

<sup>†</sup> interpolated from hydrographic data from a different hydrocast at the same station.

TABLE 18

STATION 227		62.9°S × 150.0°W						(27/04/70)			
Depth (m)	Temp* (°C)	Salinity (‰)	Concentration (×10 <sup>-5</sup> cc(STP)/Kg)				ΔHe** (%)	ΔNe** (%)	δ( <sup>3</sup> He) (%)	Δ'He (%)	
			He	Ne	Kr	Xe					
50	-1.17	34.12	-	-	8.44	1.315	-	-	-1.4	-	
200	1.05	34.70	4.29	18.30	7.29	1.342	8.5	4.3	7.5	4.2	
500	1.12	34.73	4.60	19.02	7.85	1.314	-	8.5	7.2	-	
1000	0.76	34.72	4.79	20.31	8.96	1.359	20.9	15.6	7.6	5.3	
1500	0.45	34.71	4.68	20.33	-	-	18.1	15.3	7.7	2.8	
2000	0.31	34.71	4.49	19.95	9.33	1.389	13.1	12.9	7.5	0.2	
2500	0.01	34.70	4.26	19.35	9.08	1.388	7.1	9.3	7.4	-2.2	
3000	-0.08	34.71	4.32	19.82	8.56	1.345	8.5	11.8	7.3	-3.3	
3400	-0.10	34.71	4.24	20.07	9.14	1.384	6.7	13.2	6.9	-6.5	

STATION 230		49.9°S × 150.0°W						(01/05/70)			
Depth (m)	Temp* (°C)	Salinity (‰)	Concentration (×10 <sup>-5</sup> cc(STP)/Kg)				ΔHe (%)	ΔNe (%)	δ( <sup>3</sup> He) (%)	Δ'He (%)	
			He	Ne	Kr	Xe					
5	9.28	34.57	4.02	17.35	7.23	1.075	4.9	5.8	-0.1	-0.9	
50	9.45	34.54	3.97	16.91	7.79	1.059	3.4	3.2	-0.2	0.2	
500	7.13	34.42	-	17.73	8.05	1.124	-	6.2	-1.3	-	
1000	4.99	34.34	4.20	18.13	7.97	1.252	7.8	6.7	2.5	1.1	
1500	2.95	34.44	4.18	17.94	8.95	1.394	6.4	3.9	7.5	2.5	
2000	2.49	34.61	4.26	18.67	8.81	1.381	8.3	7.7	9.7	0.6	
2500	2.17	34.71	4.20	18.68	9.76	1.451	6.8	7.6	9.7	-0.8	
3000	1.83	34.74	4.27	18.97	-	-	8.6	8.9	9.5	-0.3	
3500	1.48	34.73	4.22	18.84	9.04	1.434	7.0	7.9	8.9	-0.9	
4000	1.19	34.72	-	19.02	9.44	1.559	-	8.6	9.3	-	

STATION 234		30.0°S × 150.0°W						(07/05/70)			
Depth (m)	Temp* (°C)	Salinity (‰)	Concentration (×10 <sup>-5</sup> cc(STP)/Kg)				ΔHe (%)	ΔNe (%)	δ( <sup>3</sup> He) (%)	Δ'He (%)	
			He	Ne	Kr	Xe					
5	21.12	34.57	3.80	15.57	5.10	0.795	2.3	3.6	0.7	-1.3	
50	21.34	34.54	3.89	15.70	6.01	0.803	4.9	4.5	-0.1	0.4	
500	7.99	34.49	-	17.96	8.66	1.127	-	8.4	-0.5	-	
1000	4.40	34.35	4.29	18.40	9.70	1.396	9.5	7.7	2.1	2.2	
1500	2.71	34.54	4.43	18.96	9.09	1.399	12.6	9.6	13.4	3.0	
2000	2.05	34.63	4.37	18.81	9.32	1.419	11.0	8.2	20.6	2.8	
2500	1.68	34.67	-	18.75	8.64	1.432	-	7.4	23.0	-	
3000	1.44	34.68	4.32	18.98	9.16	1.444	9.4	8.6	19.9	0.8	
3500	1.16	34.70	4.30	18.92	9.59	1.514	8.7	8.0	15.5	0.7	
4000	0.96	34.71	4.23	18.97	8.36	1.458	7.0	8.1	12.8	-1.1	

STATION 243		16.0°N × 150.1°W						(26/05/70)			
Depth (m)	Temp* (°C)	Salinity (‰)	Concentration (×10 <sup>-5</sup> cc(STP)/Kg)				ΔHe (%)	ΔNe (%)	δ( <sup>3</sup> He) (%)	Δ'He (%)	
			He	Ne	Kr	Xe					
5	25.12	34.64	3.65	14.58	5.03	0.710	-1.4	-1.0	2.4	-0.4	
50	24.96	34.61	3.90	15.33	4.99	0.729	5.3	4.0	3.9	1.3	
500	7.63	34.46	-	18.25	7.37	1.167	-	9.8	6.0	-	
1000	4.52	34.51	4.66	19.62	7.98	1.232	19.4	15.1	16.7	4.3	
1500	3.00	34.58	4.63	19.71	9.42	1.461	17.9	14.2	19.2	3.7	
2000	2.10	34.64	4.44	19.05	9.12	1.499	12.8	9.6	22.7	3.2	
2500	1.66	34.68	-	-	9.45	1.459	-	-	25.0	-	
3000	1.24	34.68	4.37	19.04	-	-	10.6	8.9	21.3	1.7	
4000	1.12	34.69	4.31	18.89	8.77	1.489	8.9	7.7	16.1	1.2	
4900	0.97	34.70	4.27	19.33	9.35	1.493	8.0	10.1	17.2	-2.1	

STATION 247		42.8°N × 149.9°W						(03/06/70)			
Depth (m)	Temp* (°C)	Salinity (‰)	Concentration (×10 <sup>-5</sup> cc(STP)/Kg)				ΔHe (%)	ΔNe (%)	δ( <sup>3</sup> He) (%)	Δ'He (%)	
			He	Ne	Kr	Xe					
50	9.62	33.25	4.51	18.51	7.31	1.178	16.9	12.5	5.7	4.4	
500	4.61	33.98	-	18.71	-	1.354	-	9.5	7.9	-	
1000	3.06	34.34	4.59	18.66	8.53	1.447	16.8	8.0	12.7	8.8	
1500	2.26	34.50	4.58	18.78	8.45	1.355	16.4	8.1	16.4	8.3	
2000	1.77	34.59	4.50	18.45	9.39	1.512	14.1	5.8	19.2	8.3	
2500	1.54	34.63	-	-	-	-	-	-	19.2	-	
3000	1.34	34.68	4.43	18.89	-	1.561	12.0	8.0	16.0	4.0	
4000	1.15	34.68	-	-	-	1.473	-	-	15.9	-	
5000	1.13	34.69	4.26	18.95	-	-	7.7	8.1	15.9	-0.4	

UNCERTAINTY											
		Concentration (×10 <sup>-5</sup> cc(STP)/Kg)				ΔHe		ΔNe		δ( <sup>3</sup> He)	
		He	Ne	Kr	Xe	(%)	(%)	(%)	(%)	(%)	
		0.01	0.05	0.02	0.003	0.4	0.4	0.2	0.6		

\* Potential Temperature

\*\* Relative to the solubilities of Weiss (1971)

$$\Delta'He \equiv \Delta He - \Delta Ne \quad .$$

The uncertainties in the concentrations given in Table 18 are the quadrature sum of the measurement and spike size errors, and the uncertainties quoted for the saturation anomalies (including  $\Delta'He$ ) include the solubility uncertainties. It should be noted, however, that especially with the saturation anomalies the greater part of the uncertainty is systematic (the spike size uncertainty) or a smooth function of temperature and therefore depth (the solubility uncertainty). This means that the data will sometimes appear smoother than the errors would merit if they were totally random.

Profiles (plots versus depth) of  $\delta(^3He)$ ,  $\Delta He$  and  $\Delta Ne$ , Xe and Kr concentrations, and  $\Delta'He$  are given in Figures 17 through 20.

## B. Discussion

The discussion is divided into two parts. The first consists of a detailed step-by-step examination of each station with the specific intent of relating the data to what is already "known" about the hydrographic structure. The second part is an overview of the general trends of the data in the Pacific, and extends the discussion to data

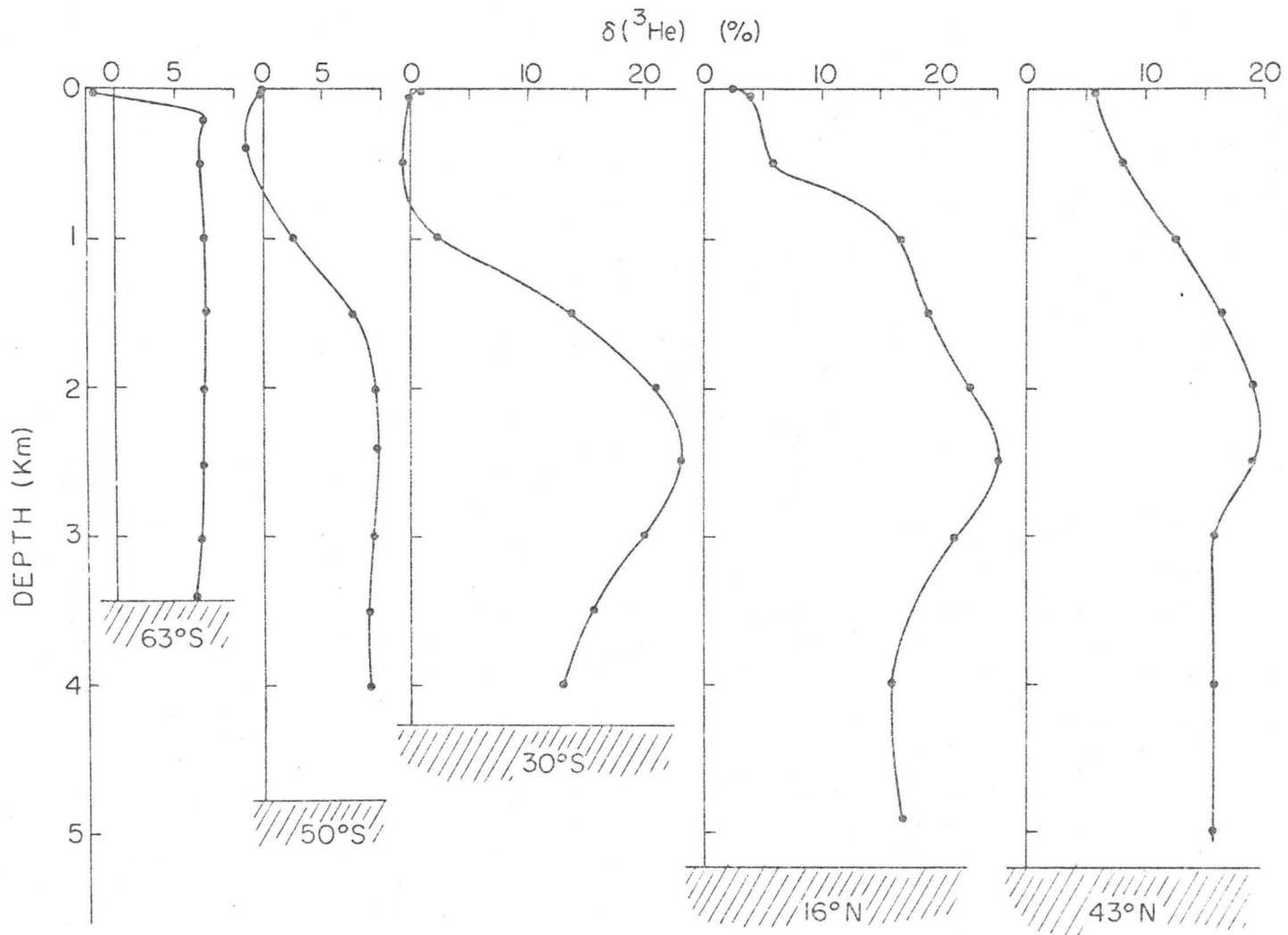


FIGURE 17: Helium Isotope Ratio Anomaly Profiles along 150°W

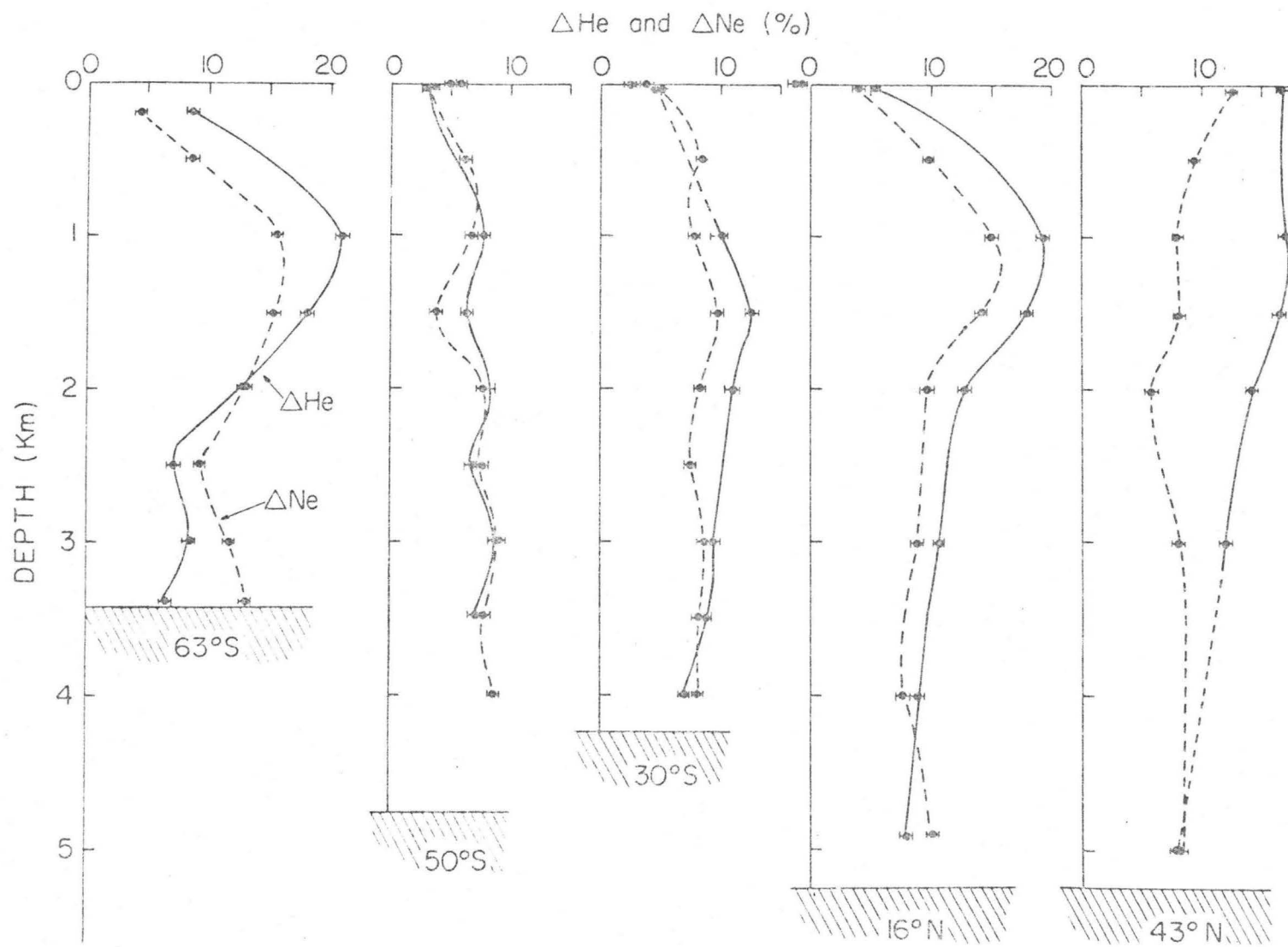


FIGURE 18: Helium and Neon Saturation Anomaly Profiles along 150°W

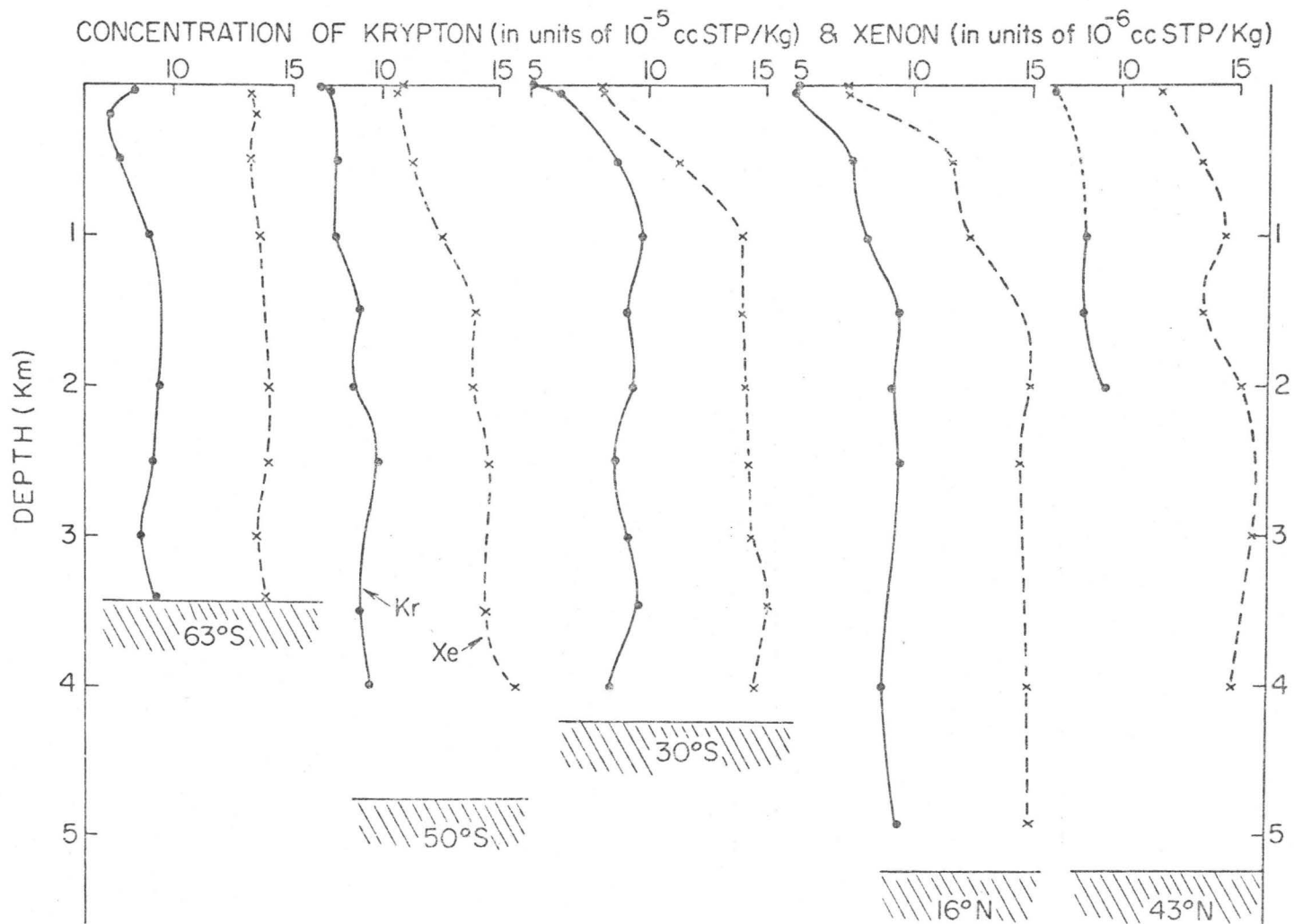


FIGURE 19: Krypton and Xenon Concentration Profiles along 150° W

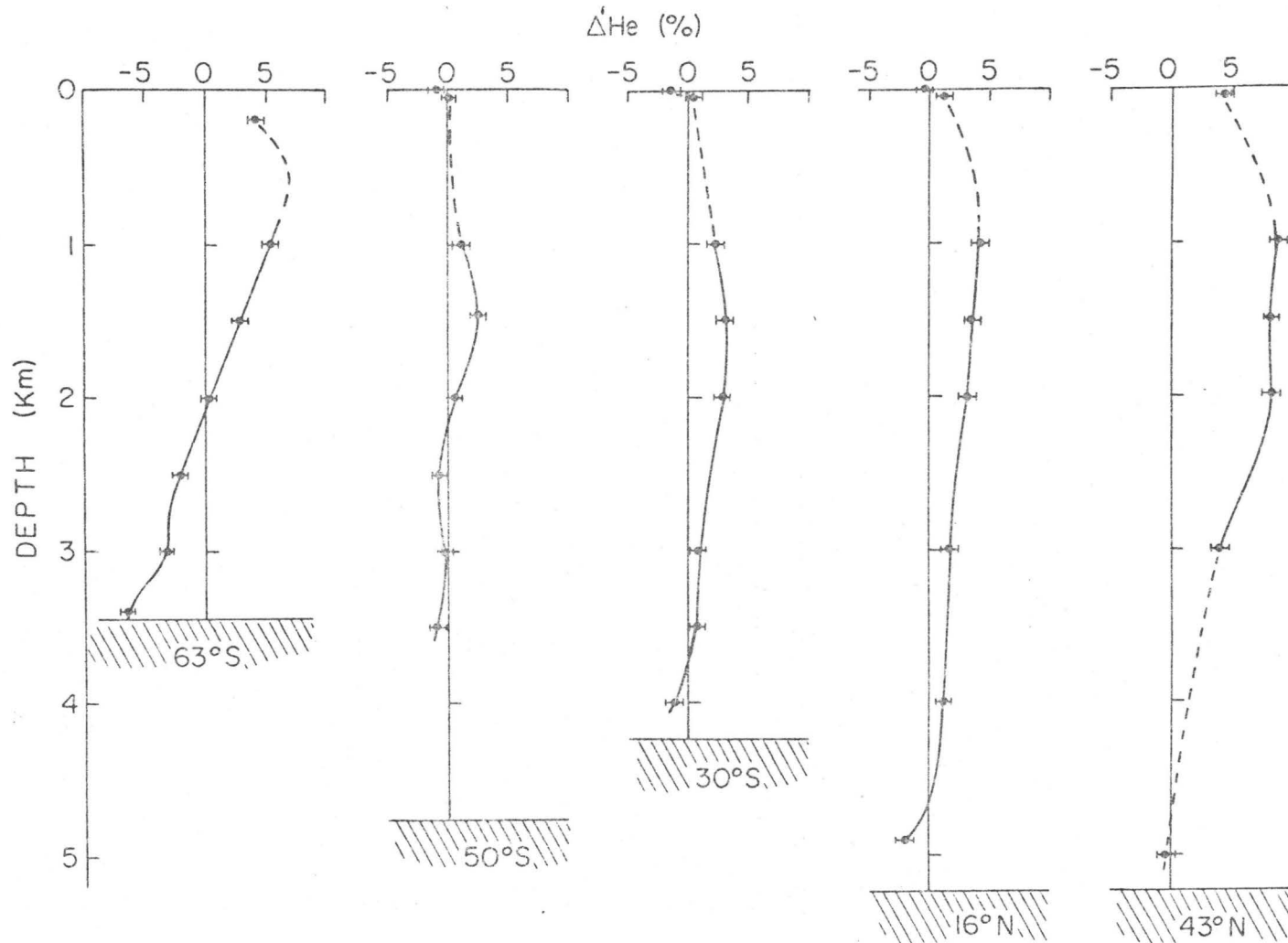


FIGURE 20: Excess Helium Profiles Along 150° W

measured by others.

1. The Data in Relation to Hydrographic Structure

(i) Station 227: 62.9°S × 150.0°W

This station was situated to the north-west of the Ross Sea, on the Antarctic side of the Circumpolar Current (see Callahan, 1972: Fig. 3,6). Hydrographically the station is dominated by the presence of the Circumpolar Deep Water (CPDW) at a depth of 300 to 400 m, characterized by a salinity and temperature maximum and dissolved oxygen minimum (Gordon, 1971a, 1971c; Callahan, 1972). Above this, separated from the Deep Water by an abrupt halocline, is a cold, thin, less saline mixed layer. Below the CPDW the temperature decreases to the bottom, but the oxygen and salinity reach a deep maximum at 3000 m, indicating the presence of bottom water found in the Ross Sea (Gordon, 1971a, 1972). The bottom water is separated from the overlying deep water by a salinity minimum and inflection in the potential temperature profile at 2500 m.

The ratio anomaly  $\delta(^3\text{He})$  (Fig. 17) shows a sharp transition across the halocline, indicating minimal exchange processes across this surface. This is reasonable, as the sharp density gradient inhibits turbulent exchange. Above the halocline the  $\delta(^3\text{He})$  is -1.4%, within errors of the solubility equilibrium isotope effect of  $-1.2 \pm 0.2\%$  measured by Weiss (1970), indicating that the tritium content

of the water at the time of sampling must have been less than 0.2 T.U. since the sample was stored for two years prior to extraction. Below the halocline the  $\delta(^3\text{He})$  is 7.5%, decreasing to 7.2% in the core of the CPDW and increasing to a maximum of 7.7% at 1500 m. Below 1500 m the ratio anomaly decreases to 6.9% at the bottom. This last effect is likely due to mixing with Ross Sea Bottom Water (RSBW) which is probably relatively free of excess  $^3\text{He}$ .

The saturation anomaly curves ( $\Delta\text{He}$  and  $\Delta\text{Ne}$ , Fig. 18) exhibit pronounced maxima between 1000 and 1500 m, likely corresponding to the  $\delta(^3\text{He})$  maximum at 1500 m. At the transition point between the RSBW and the CPDW (2500 m) both anomalies reach minima, and begin to increase below this depth. The  $\Delta\text{He}$  curve reaches a maximum at the RSBW core.

The Kr and Xe concentrations (Fig. 19) are anticorrelated near the CPDW core, the Kr concentration reaching a minimum while the Xe reaches a maximum. The behaviour of the Xe is somewhat surprising in that a minimum would be expected due to the temperature maximum. Below this both gases reach maximum concentrations around 1500 m, somewhat below the  $\Delta\text{He}$ ,  $\Delta\text{Ne}$  maxima, but because the temperature decreases (and thus the solubility increases) below the CPDW core, it can be reasonably expected that the corresponding saturation anomaly maxima would lie above the concentration maxima, and likely near the depth of the  $\Delta\text{He}$ ,  $\Delta\text{Ne}$  maxima. This is further supported by the fact that the

Xe maximum lies below the Kr maximum. Both concentration curves exhibit minima in the RSBW core at 3000 m.

The Excess Helium Anomaly  $\Delta^{\prime}\text{He}$  (Fig. 20) is a linear function of depth and salinity between 1000 and 2500 m. The highest value (at 1000 m) is 5.3% and the lowest value on the linear portion of the curve is - 2.2%. The linearity is not surprising as these depths lie on a linear portion of the  $\theta$  - S curve. The interval thus defined is therefore a "mixing subrange" between the CPDW and RSBW water types. The core of the RSBW is marked by a local maximum in the  $\Delta^{\prime}\text{He}$  profile.

(ii) Station 230: 49.9°S × 150.0°W

This station is located just north of the Circumpolar Current core (see Callahan, 1972), and lies in a transition zone between the Antarctic and South Pacific Oceans. The potential temperature - salinity relation correspondingly indicates the complicated juxtaposition of water masses with few, if any, regions of linearity.

Since it is situated north of the Polar Front Zone (Gordon, 1971b), this station exhibits the salinity minimum characteristic of the Antarctic Intermediate Water (Reid, 1965, 1973) at 1000 m. Below the Intermediate Water (AAIW) core the dissolved oxygen content decreases to a broad, deep minimum at 2500 m. This is a widespread characteristic of the South Pacific (Wyrтки, 1962; Reid, 1965, 1973; Warren,

1973: esp. pl. 3) but it is not known whether this is a true advective core (see, for example, the views of Craig, 1969, 1971a, 1971b; Suess and Goldberg, 1971; Reid, 1973; Warren, 1973). Around 3200 to 3400 m the salinity reaches a maximum of  $\sim 34.74$  ‰, indicating the influence of the deep Western Boundary Current (Warren, 1973: esp. pl. 2). Below this the salinity and temperature decrease to the bottom. The oxygen, however, reaches a maximum at 4500 m, corresponding to a break in the  $\theta$  -S relation and thus perhaps representing bottom water flow.

The ratio anomaly profile is shown in Fig. 17. The surface value of  $-0.1\%$  and the subsurface (50 m) value of  $-0.2\%$  are somewhat above the isotopic solubility equilibrium value of  $-1.3\%$  for water of this temperature (Weiss, 1970c), due to in situ and in storage decay of tritium. If a zero residence time were assumed for the surface sample, this would indicate a tritium concentration of about 2 T.U. at the time of sampling. The lower subsurface  $\delta(^3\text{He})$  is a result of decreasing tritium concentrations with depth. Below the thermocline the  $\delta(^3\text{He})$  reaches a minimum of  $-1.3\%$  at 500 m and increases to a broad maximum of  $9.7\%$  at 2000 to 2500 m, corresponding to the oxygen minimum. This maximum is likely the result of transport<sup>†</sup> of excess  $^3\text{He}$  from regions of larger

---

<sup>†</sup> The term "transport" is used here so as not to distinguish the mechanism. It should be taken to mean either mixing, advection, diffusion or any combination of the three.

$\delta(^3\text{He})$ , probably from the north. If a ratio anomaly of 7.2% were taken as characteristic of the CPDW (as in the Antarctic Profile), and  $\delta(^3\text{He}) = 25\%$  as characteristic of PDW (Pacific Deep Water), the water at 2000 to 2500 m may be regarded as a mixture of 14% PDW and 86% CPDW.

The deep Western Boundary Current manifests itself in a slight, but significant ratio anomaly minimum. This suggests that the deep water entering the Pacific has a lower  $\delta(^3\text{He})$  than the deep water returning from the Pacific, which is consonant with injection of  $^3\text{He}$  into the Pacific Deep Water. Below the minimum the ratio anomaly begins to increase with depth, but the lack of a sample near the deep oxygen maximum hampers delineation of the possible bottom water advective core.

The  $\Delta\text{He}$ ,  $\Delta\text{Ne}$  profiles (Fig. 18) indicate the complicated interlayering of water masses in this station. Both anomalies reach a maximum at the AAIW core, being consistent with the observations of Craig et al. (1967) and Craig and Weiss (1971) of slight maxima of  $\Delta\text{Ar}$  in the same. Below this the curves exhibit slight maxima at 2000 and 3000 m, perhaps corresponding to the PDW and Western Boundary Current.

The Kr and Xe concentration profiles (Fig. 19) also indicate the complexity of the hydrography at this station, exhibiting maxima at 1500 and 2500 m and minima at 2000 and 3500 m. There is a general trend of increasing concentration with depth throughout the profile due to decreasing

temperature but a notable increase in the trend occurs at 3500 m for both gases. This is paralleled by a similar effect in the  $\Delta\text{Ne}$  trend, which hints that the bottom water here may have saturation anomaly maxima as a core property. This does not conflict with the observation of local minima in the Bottom Water core at  $63^\circ\text{S}$ , because the Bottom Water seen here is likely of a different origin (see Gordon, 1972).

As with the Antarctic profile, the  $\Delta^3\text{He}$  curve (Fig. 20) decreases to negative values below 2000 m; but, due to the complexity of the hydrography, exhibits much more structure. At the surface the  $\Delta^3\text{He}$  is near zero. Below the thermocline it increases to a maximum at 1500 m, decreases to a minimum at 2500 m and increases to a deep maximum at about 3200 m.

(iii) Station 234:  $30.0^\circ\text{S} \times 150.0^\circ\text{W}$

The presence of the AAIW is indicated at this station by a salinity minimum (Reid, 1965) centred at 850 m. Below the AAIW core the dissolved oxygen content decreases to the characteristic deep minimum at 2500 m. At about 2800 m lies a broad silicate maximum which can be seen (Warren, 1973: pl. 6) extending across the South Pacific at  $28^\circ\text{S}$  from the Western Boundary ( $\sim 180^\circ\text{W}$ ) to the western flank of the East Pacific Rise. Craig et al. (1972) consider this, at least in the western region, as a marker for their "Benthic Front", which is a frontal zone between

southward trending Pacific Deep Water above and northward flowing Bottom Water below. The Front is more properly associated with inflections in the  $\theta$ ,  $S$ , and  $\sigma_4$  profiles (ibid), but the bottle spacing, combined with the fact that the frontal zone is weakly developed in this area makes it difficult to precisely define the depth of the Front. From the available data it appears that the Front lies somewhere below 2500 m and above 3500 m. At 4000 m lies a salinity and oxygen maximum which are indicative of Bottom Water. There is a virtual silicate minimum at the ocean floor.

The surface sample  $\delta(^3\text{He})$  is 0.7%, somewhat higher than the surface sample at 50°S, for the same storage time. Assuming a zero residence time it is possible to estimate an upper limit of  $4.2 \pm 0.8$  T.U. for this sample. Below the surface the ratio anomaly decreases to - 0.5% at 500 m, and then increases through the Intermediate and Deep Water to a maximum of 23.0% at 2500 m. Below this it decreases smoothly to 12.8% at 4000 m. There is a notable convexity (negative curvature) both above and below the maximum. Examination of the  $\delta(^3\text{He})$ - $S$  relationship (Fig. 21) from below the core of the AAIW (> 1000 m) to the bottom reveals that the ratio anomaly is a linear function of salinity from 1500 m to 2500 m and from 2500 m to 4000 m, with the 2500 m depth acting as a common point for both relations. The linearity intimates that the ratio anomaly behaves as a conservative property in the framework of the one-dimensional

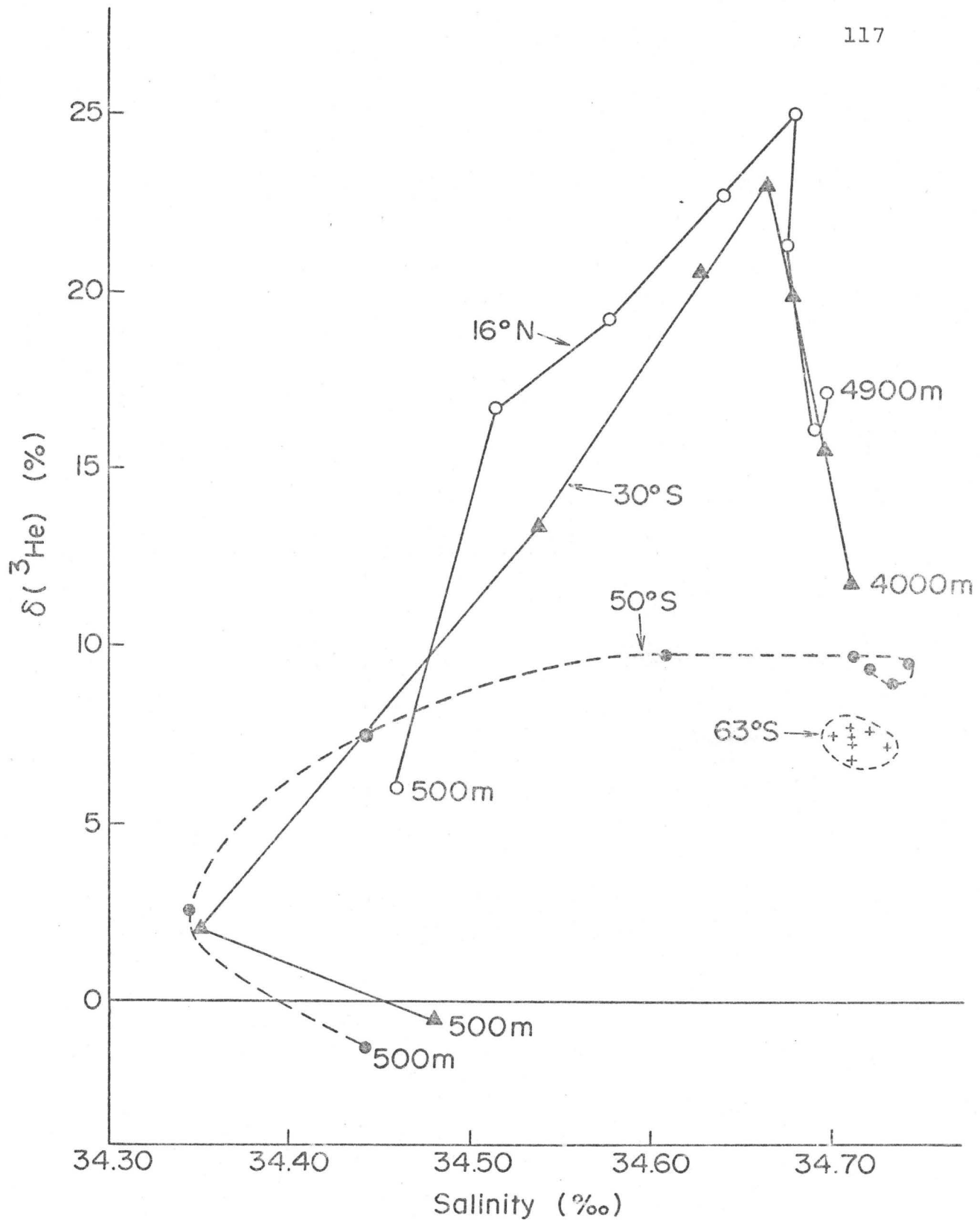


FIGURE 21:  $\delta(^3\text{He})$  vs Salinity for Deep Pacific Waters.

diffusive-advective model<sup>†</sup> (see, for example, Craig, 1969). The convexity, therefore, indicates a negative (upward) upwelling velocity<sup>†</sup>. This will be discussed in more detail later.

The  $\Delta\text{He}$ ,  $\Delta\text{Ne}$  profiles (Fig. 18) exhibit maxima not at the AAIW core but at 1500 m. It should be noted, however, that the saturation anomalies are larger in the AAIW core here than at 50°S. The "maximum" seen at 50°S is here masked by even larger saturation anomalies in the Deep Water: the average Deep Water  $\Delta\text{Ne}$  and  $\Delta\text{He}$  are 8.3 and 9.7% respectively, whereas at 50°S the corresponding values are 7.4 and 7.4%. Below the maximum at 1500 m the  $\Delta\text{Ne}$  approaches a minimum above the Front and then increases to an essentially constant value from 3000 to 4000 m. Below 1500 m the  $\Delta\text{He}$  curve decreases to a constant value from 3000 to 3500 m and then decreases further to 4000 m.

In the upper 1000 m of the water column the Kr and Xe concentrations (Fig. 19) increase rapidly with depth, as a result of decreasing temperatures and correspondingly increasing solubilities. The Kr concentration curve reaches a maximum in the AAIW core, while the Xe trend with depth decreases to a more gradual slope. Below this depth the Xe increases smoothly to 3000 m, and exhibits a maximum at 3500 m. The Kr profile shows more structure in the Deep Water, coming to a minimum at 2500 m as does the  $\Delta\text{Ne}$  profile, and exhibiting a maximum similar to the Xe profile at 3500 m.

---

<sup>†</sup> See Appendix 1.

The  $\Delta^3\text{He}$  increases from a slightly negative value at the surface to a broad maximum of  $\sim 3\%$  between 1500 and 2000 m. Below the Front it decreases to a constant value of  $\sim 0.8\%$  and in the Bottom Water core it decreases to  $-1.1\%$ .

(iv) Station 243:  $16.0^\circ\text{N} \times 150.1^\circ\text{W}$

The Arctic Intermediate Water (AIW), characterized by a thermosteric anomaly of 125  $\text{cl}/\text{ton}$  and a (local) salinity minimum (Reid, 1965) appears at this station at a depth of 500 m. Below it, at a depth of 1000 m lies a secondary oxygen minimum and pronounced nutrient maximum which are part of a large lens of low oxygen-high nutrient water occupying intermediate depths in the eastern North-Equatorial Pacific (Reid, 1965; Barkley, 1968). The consensus of opinion is that this is a result of in situ consumption balanced by poor lateral renewal due to the low geostrophic velocities in this region (Reid, 1965; Blanton and Patullo, 1970; Pytkowicz and Kester, 1966).

Below the AIW the salinity increases to a maximum at 2500 m, decreases to broad minimum at 3000 to 3500 m and exhibits two maxima at 4100 and 4900 m. This structure is not seen elsewhere, but Wong (1972) has found marginal evidence of zonal deep water masses in this area. This is supported by a slight but significant oxygen maximum at 4900 m, indicative of an advective core. Similar conclusions have been drawn by others (Reid, 1969; Duedall

and Coote, 1972; Edmond et al., 1971) and a summary is given by Johnson (1972) of what is known of bottom water flow in the area. The accepted view is that Bottom Water flows from the south around Samoa and the Manihiki Plateau and enters the Central and Eastern North Pacific through gaps in the Line Islands Ridge. The Bottom Water then flows anticlockwise around the end of the Hawaiian Ridge.

The presence of Bottom Water at this station suggests the possibility of a frontal zone, and Craig et al. (1972) using data from the SOUTHERN CROSS Expedition have traced the Front into the North Pacific. It is feasible, therefore, that the complicated deep salinity structure, combined with a silicate maximum at 2700 m may indicate that such a front occurs at this station.

The surface  $\delta(^3\text{He})$  value is 2.4%, indicative of a tritium content of 7.6 T.U. at the time of sampling. Using this tritium value for an estimate of the tritium concentration at 50 m yields a residence time of 9 months for a  $\delta(^3\text{He})$  of 3.9%. Below the thermocline the ratio anomaly increases to 6.0% at the AIW core, then increases more rapidly to 16.7% at 1000 m. From 1000 m to 2500 m the ratio anomaly increases more slowly to a mid-depth maximum of 25.0%. The 1000 m value of  $\delta(^3\text{He})$  appears as a "shoulder" on the curve, perhaps suggesting that the water at this level may have advected from an area of larger Deep Water  $\delta(^3\text{He})$  levels, but it is not possible, however, to draw firm

conclusions on the basis of one sample.

The  $\delta(^3\text{He})$ -S relation (Fig. 21) for this station accentuates the anomalously high  $\delta(^3\text{He})$  value at 1000 m. From 1500 m to the maximum the  $\delta(^3\text{He})$ -S curve is linear, again indicating applicability of the one-dimensional diffusive-advective model. Underneath the maximum the relation is markedly non-linear, with a reversal in trend at 4000 m.

Below the mid-depth maximum the ratio anomaly reaches a minimum of 16.1% at 4000 m, and then increases to 17.2% at 4900 m. The minimum at 4000 m is possibly a feature induced by flow of Bottom Water from an area of weaker mid-depth maxima (south and west of here). Craig et al. (1972) have noted a similar effect in silicate. The virtual maximum in  $\delta(^3\text{He})$  at 4900 m may be the result of primordial injection into the bottom water as it passes through gaps in the Line Islands Ridge. Examination of the  $\delta(^3\text{He})$ -S relationship (Fig. 21) indicates that it is not likely that such a  $\delta(^3\text{He})$ -S value could be attained by mixing.

The  $\Delta\text{He}$ ,  $\Delta\text{Ne}$  profiles (Fig. 18) go through large and distinct maxima at about 1000 m. This may, like the  $\delta(^3\text{He})$  indicate advection. Below the maximum both saturation anomalies decrease in a regular fashion. The  $\Delta\text{He}$  decreases to the bottom, while the  $\Delta\text{Ne}$  increases below 4000 m into the Bottom Water core.

The AIW shows up as a slight local maximum in both

Xe and Kr (Fig. 19) but this is likely an artifact of the temperature distribution: the temperature gradient (and thus the solubility gradient) tends to decrease with depth. The Kr curve reaches a maximum at 1500 to 2500 m while the Xe curve reaches a single maximum at 2000 m and increases smoothly to the bottom.

The  $\Delta^4\text{He}$  profile (Fig. 20) exhibits a broad, weak maximum of 4.3% at 1000 m, below which it decreases gradually to a value of 1.2% at 4000 m, and then decreases rapidly to - 2.2% in the Bottom Water core. The 1000 m sample is again weakly suggestive of advection.

(v) Station 247:  $42.8^\circ\text{N} \times 149.9^\circ\text{W}$

The AIW at this station is marked by a inflection in the salinity profile, whose nature makes it difficult to assign a precise depth. Therefore, the depth of the 125 cl/ton isanostere (450 m) is chosen (Reid, 1965). Below this surface the salinity increases in a smooth, regular fashion to the bottom. There occurs a pronounced oxygen minimum-nutrient maximum at 1250 m which may be attributed to the intermediate depth lens of low oxygen-high nutrient water encountered at the previous station (Reid, 1965). Below this the oxygen increases to a broad maximum centred at 4500 to 5000 m, suggesting the presence of Bottom Water flow. The oxygen distribution along  $150^\circ\text{W}$  (Duedall and Coote, 1972) is rather suggestive of some meridional flow

of Bottom Water from the south, but not without achievement of a certain degree of homogenization due to mixing, as indicated by the slope and divergence of the dissolved oxygen isopleths and the broadness of the maximum encountered at this station.

The uppermost  $\delta(^3\text{He})$  (at 50 m, Fig. 17) indicates an upper limit of 16 T.U. for the tritium concentration at the time of sampling. This was determined by assuming all the excess  $^3\text{He}$  (corresponding to  $\delta(^3\text{He}) = 5.7\%$ ) due to in storage decay of tritium. Below this the ratio anomaly increases smoothly through the Intermediate and Deep Waters to a rather broad mid-depth maximum of 19.2% at 2000 to 2500 m. By 3000 m the ratio anomaly has decreased to 16.0%, below which it is essentially constant to the bottom. The  $\delta(^3\text{He})$  indicates a remarkable degree of homogeneity in the bottom 2000 m of the profile, more so than the oxygen.

The 50 m values of  $\Delta\text{He}$  and  $\Delta\text{Ne}$  (Fig. 18) are extraordinarily high compared with the other helium and neon surface values. Bieri and Koide (1972) have reported the occasional occurrence of such anomalous values, but it is not known at this time what precisely is the cause (ibid). It should be noted that such large supersaturations in near surface waters are rare. The  $\Delta\text{He}$ , below the thermocline, is much larger relative to  $\Delta\text{Ne}$  than elsewhere. It does, however, tend to reflect the structure of the  $\Delta\text{Ne}$  profile.

The Xe profile (Fig. 19) exhibits a rather

pronounced minimum at 1500 m that is reflected in the Kr profile. Below 3000 m it decreases slightly to 4000 m.

The  $\Delta^4\text{He}$  curve (Fig. 20) is essentially constant between 1000 and 2000 m at a value of  $\sim 8.5\%$ , the largest levels encountered. Below this it decreases to  $4.0\%$  at 3000 m and  $- .4\%$  at 5000 m.

## 2. General Trends

### (i) Krypton and xenon concentrations

Efforts to extract significant information from krypton and xenon concentrations are hampered by lack of solubility data, but some general features are evident. Relative to the solubility data of König (1963), krypton and xenon are on the average 16 and 31% supersaturated in Pacific sea water. The saturation anomalies range from 2 to 36% for krypton and from 14 to 45% for xenon. In general, the anomalies of one gas tend to correlate with the other, with the lowest values being at the surface and the highest values in, but not restricted to, the Deep Waters.

To date there is no known mechanism that is capable of enriching the gases to such an extent. As pointed out in Chapter 1, injection of a reasonable amount of air ( $\approx 1$  ml/Kg) will result in only 1.6 and 0.9% enrichment for Kr and Xe. Mixing can account for no more than 5 and 6%, and moderate ( $\approx 2^\circ\text{C}$ ) temperature changes produce less than 5 and 8%

supersaturation.

Surface waters are on the average 6 and 23% supersaturated in krypton and xenon, and the Antarctic profile averages 9 and 20%. This suggests that a large part of the enrichment process must take place in situ in Pacific deep water. One possibility lies in the fact that the molecular diffusivity of heat is two orders of magnitude larger than that for gases. Turbulent exchange processes ultimately depend on molecular diffusion, suggesting that the eddy exchange coefficients may differ between properties (Neumann and Pierson, 1966). It may, therefore, be possible to have a downward flux of heat into the deep water without significant diffusion of gas upwards. This would resemble a temperature change after equilibration, and qualitatively reflect the observed pattern of gases.

The concentrations measured are in good general agreement with the krypton values of Bieri and Koide (1972) and the krypton and xenon values of Hintenberger et al. (1964). They are in disagreement with those of Mazor et al. (1964).

(ii) The saturation anomalies of helium and neon

With the exception of the anomalous values at 43°N, the  $\Delta\text{He}$  values for surface (5 m) and subsurface (50 m) samples vary between - 1.4 and + 5.3%, with a mean value of 3.2%. The corresponding values for  $\Delta\text{Ne}$  are - 1.0 and + 5.8%,

with a mean of 3.3%. There is no significant trend with latitude but there may be a tendency for the deeper samples to have slightly larger saturation anomalies. In all three pairs of samples  $\Delta\text{Ne}$  was greater than  $\Delta\text{He}$  at the surface and  $\Delta\text{He}$  was greater than  $\Delta\text{Ne}$  at 50 m.

Whereas the major ingassing mechanism appears to be air injection (Kanwisher, 1963; Atkinson, 1973) which tends to enrich helium relative to neon (Craig and Weiss, 1971), the degassing process, being ultimately diffusion limited (Kanwisher, 1963), will tend to deplete helium relative to neon, since the molecular diffusivity of helium is more than 30% greater than that of neon (Boerboom and Kleyn, 1969). The observed  $\Delta\text{He}$ - $\Delta\text{Ne}$  patterns, in a qualitative way, indicate that the former process (enrichment of helium relative to neon) predominates at 50 m while the latter (depletion of helium relative to neon) is dominant at 5 m. This is a gross oversimplification of the processes actually taking place, and a detailed, high sampling density, synoptic study of all rare gas concentrations in the mixed layer is needed to unravel the complexities. Bieri et al. (1968) and Bieri and Koide (1972) have taken the first steps, but an improvement in precision coupled with more reliable solubility data for Kr and Xe is required for more meaningful results.

Table 19 summarizes the general trends in the saturation anomalies in the data. The depth ranges chosen are as follows:

Intermediate	500	to	1000 m
Deep	1500	to	2500 m
Bottom	3000	to	bottom

and the values given are averages over the appropriate depth range. The boundary between the Deep and Bottom waters has been placed arbitrarily at 2750 m, just below the characteristic mid-depth ratio anomaly maximum.

In the Deep and Intermediate Waters, both saturation anomalies are larger and increase equatorward (see Table 19), with an asymmetry about the equator: larger corresponding values being in the North. This last effect is exemplified by the large saturation anomaly maxima at intermediate depths at 16°N. The trend may be related to the nature of Equatorial circulation at intermediate depths and perhaps to the advective-diffusive processes that "maintain" the lens of low oxygen-high nutrient water mentioned earlier, but the details of the mechanism are not clear.

The mean values for  $\Delta\text{He}$  and  $\Delta\text{Ne}$  in Intermediate Waters are on the average higher than those in the Deep and Bottom Waters, especially in the North Pacific, being qualitatively consistent with the observations of Craig et al. (1967). They attribute this phenomenon to subsurface mixing, but as

TABLE 19  
PACIFIC ANOMALY TRENDS

Anomaly	Depth Range	Station				Grand Average	Pacific Average
		50°S	30°S	16°N	43°N		
$\overline{\Delta\text{He}}$	Intermediate	7.8	9.9	19.4	16.8	13.5	—
	Deep	7.2	11.8	15.4	15.3	12.4	14.2
	Bottom	7.8	8.4	9.2	9.9	8.8	9.2
$\overline{\Delta\text{Ne}}$	Intermediate	6.5	8.1	12.5	8.7	9.0	—
	Deep	6.4	8.4	11.9	7.0	8.4	9.1
	Bottom	8.5	8.2	8.6	8.1	8.4	8.3
$\overline{\Delta^1\text{He}}$	Intermediate	1.1	2.2	4.3	8.8	4.1	—
	Deep	0.8	2.9	3.5	8.3	3.9	4.9
	Bottom	-0.6	0.1	0.3	1.8	0.4	0.7
$\overline{\Delta(^4\text{He})}$	Deep	0.1	2.0	2.1	7.7	3.0	3.9
	Bottom	-1.5	-0.8	-0.7	1.0	-0.5	-0.1
	Deep and Bottom	-0.7	0.6	0.7	4.4	1.3	1.9
$\overline{\delta(^3\text{He})}$	Intermediate*	2.5	0.8	6.0	7.9	—	—
	Deep	9.0	19.0	22.3	18.5	17.2	19.9
	Bottom	9.2	16.1	18.2	15.9	14.9	16.7
	Deep and Bottom	9.1	17.6	20.3	17.2	16.1	18.3
$\overline{\Delta(^3\text{He})}$	Deep	11.1	24.2	28.7	25.8	22.5	26.2
	Bottom	9.9	18.3	20.8	19.8	17.2	19.6
	Deep and Bottom	10.5	21.3	24.8	22.8	19.9	23.0

\* Single values interpolated at the depth of the salinity minimum.

pointed out in Chapter 1, the largest effect attributable to such a process is about 1% for neon and 0.8% for helium. It is tempting, therefore, to invoke air injection combined with a diffusive degassing process in addition to mixing to generate the observed supersaturations, but the effects must be peculiar to the Polar Front Zone as they are not seen regularly in surface layers.

Examination of the geostrophic flow for the AAIW (Reid, 1965: Fig. 23) shows that the 50°S station is "downstream" of the 30°S station; further supported by the fact that the associated salinity minimum is less intense at 50°S. The observed values of saturation anomaly are, therefore, not inconsistent with the interpretation of turbulent diffusive loss of  $\Delta$  through the thermocline. The pattern in the North Pacific cannot be readily explained in this manner, but the general asymmetry between the North and South Pacific may be related to the way in which the AIW is formed. Unlike the AAIW which is "formed" at the surface, the AIW is formed by diffusion processes through the thermocline (Reid, 1965).

In the Bottom Water, no particular trend is evident for  $\Delta\text{Ne}$ , but  $\Delta\text{He}$  increases regularly from south to north. This may be due either to injection from the crust or to turbulent diffusion from the overlying deep water. Fig. 22 shows a plot of  $\Delta\text{He}$  versus average salinity for Bottom Waters. If  $\Delta\text{He}$  were strictly conservative in the Deep and

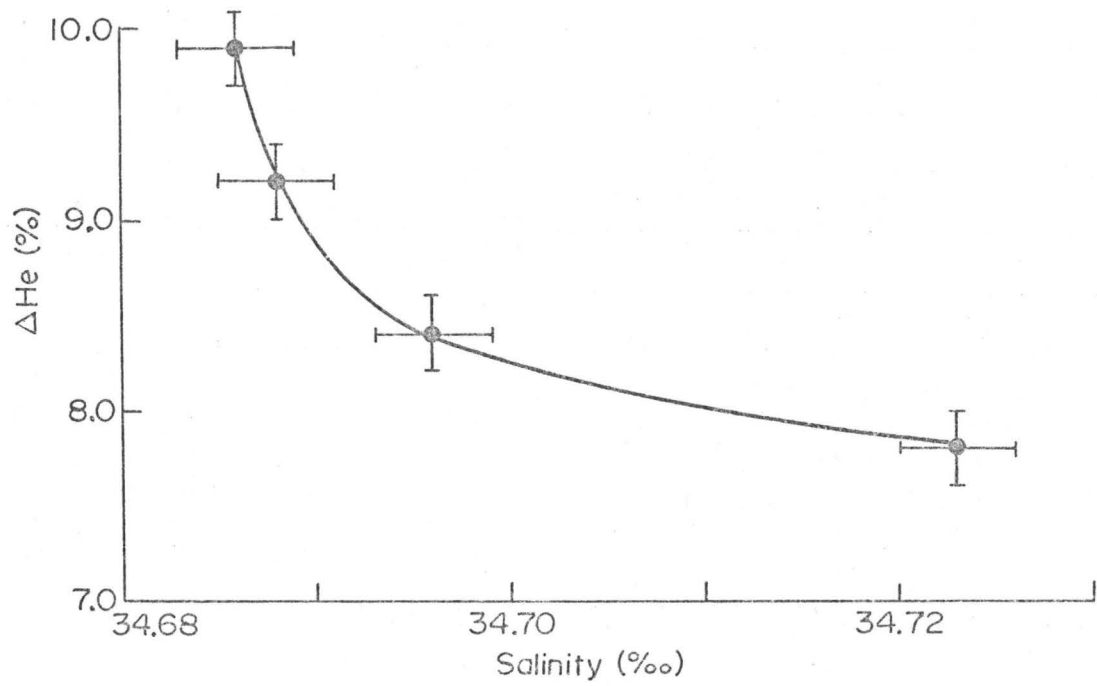
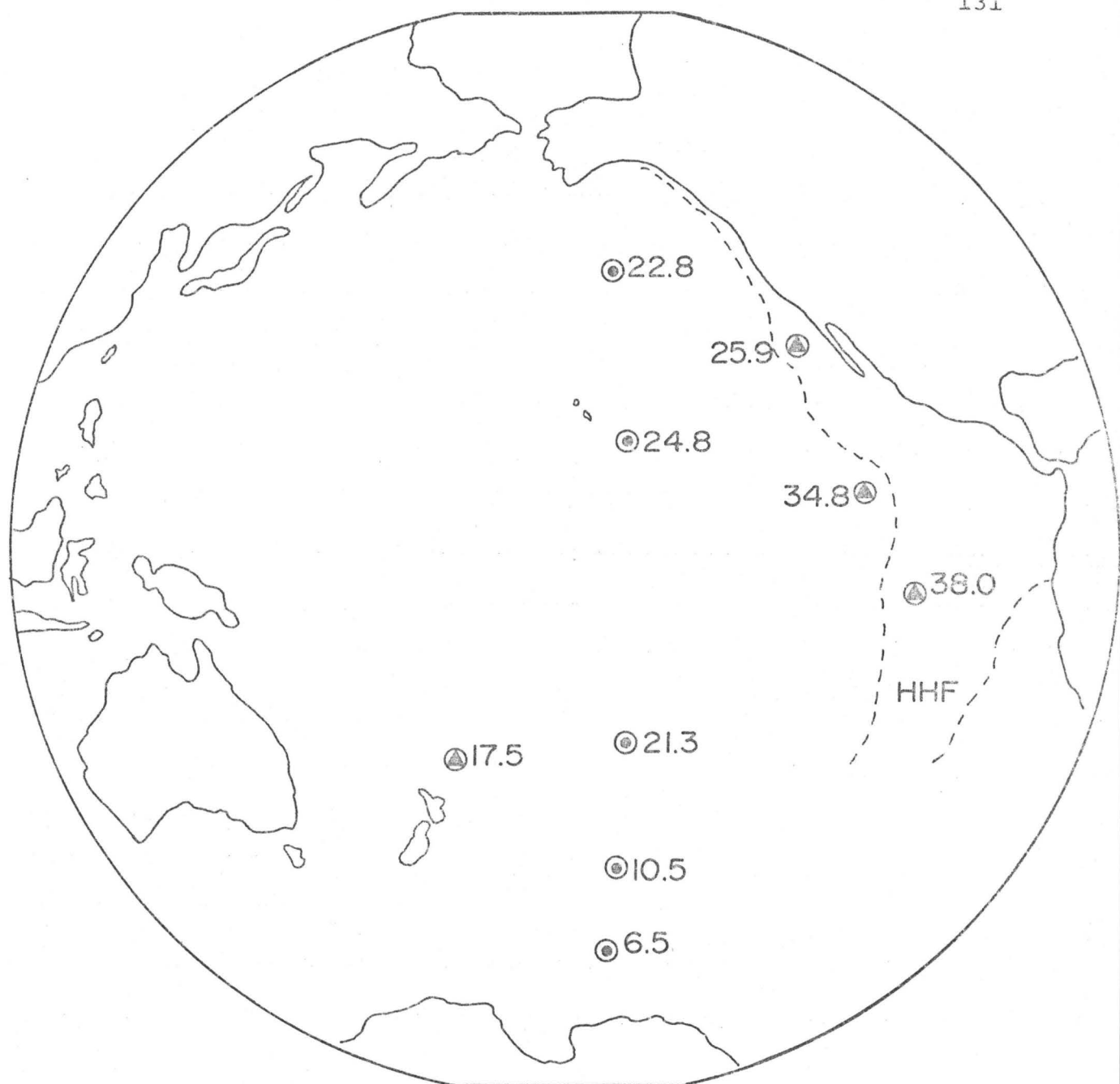


FIGURE 22:  $\Delta\text{He}$  vs Salinity for Pacific bottom waters.



Data sources :  
 This work ●  
 Beg (1971) ▲

Lambert's azimuthal  
 equal area projection  
 HHF = high heat flow

FIGURE 23: Pacific Deep and Bottom Water  $\Delta(^3\text{He})$

Bottom Waters, the  $\Delta\text{He-S}$  relation would be a straight line, whose slope is determined by the relative fluxes of salt upwards and  $\Delta\text{He}$  downward. The notable feature of the observed relationship is the positive curvature. This may be partly explained by the fact that the  $\Delta\text{He}$  content of the Deep Water, and therefore, the downward flux of  $\Delta\text{He}$  increases northward. It is possible, in principle, to distinguish between the two mechanisms by examining the  $\Delta\text{He-S}$  slope in the Bottom Water as a function of the overlying Deep Water  $\Delta\text{He}$  and  $S$ , but this would require more data than presently available.

The  $\Delta\text{He}$  distribution is summarized in Table 19. All depths exhibit the same trend of increasing northward, and generally  $\Delta\text{He}$  decreases with depth, clearly demarcating the Bottom Water. The Intermediate and Deep  $\Delta\text{He}$  values are similar, with the Intermediate Waters having slightly higher values. This tends to suggest that a large portion of the excess helium seen in the Deep Waters is due to diffusion of atmospheric helium anomaly from the overlying Intermediate Water.

Unfortunately, in light of the uncertainty in the magnitude and nature of the exchange properties between the Deep, Intermediate and Bottom Waters, it is not possible to construct a model sufficiently sophisticated enough to discriminate between the two types of helium on the basis of helium and neon saturation anomalies alone. However,

reasonable upper and lower limits can be set on the amount of non-atmospheric helium present. The most obvious upper limit is the difference between the Pacific Deep Water average  $\Delta^4\text{He}$  and the "input"  $\Delta^4\text{He}$  estimated as the average Bottom Water value at 50°S. This upper limit is 5.5%. A lower limit may be estimated by assuming all the excess neon in the Deep Water is due to air injection. This sets an effective upper limit on the excess atmospheric helium because, as far as is presently known, air injection is by far the most effective mechanism of enriching helium relative to neon (see Chapter 1). Using the Pacific Deep Water average  $\Delta^4\text{Ne}$  of 9.1%, and assuming an average Deep Water temperature of 2.5°C corresponding to an enrichment factor of 1.27, a maximum atmospheric component of 11.6% is obtained for  $\Delta^4\text{He}$ . The difference, 2.6%, is the lower limit. Taking a "middle of the road" approach, the best estimate of the non-atmospheric component of helium is, therefore,  $4 \pm 1.5\%$ . This is somewhat higher than, but not in conflict with, the estimates of Craig and Weiss (1971). In fact the difference may be attributed to the fact that the average is weighted toward the North Pacific, where the effects will be largest.

Using this intermediate approach, it is therefore possible to define the non-atmospheric excess  $^4\text{He}$  as

$$\Delta(^4\text{He}) \equiv \Delta\text{He} - \frac{1}{2} (f + 1)\Delta\text{Ne} + 0.3 \quad (14)$$

where  $f = \frac{\beta(\text{Ne})}{\beta(\text{He})}$ , the ratio of the bunsen solubility coefficients. This is an average of the two approaches:

$$\Delta(^4\text{He})_{\text{max}} = \Delta'\text{He} + 0.6$$

$$\Delta(^4\text{He})_{\text{min}} = \Delta\text{He} - f\Delta\text{Ne} .$$

It should be noted that the intermediate approach yields negative values for most of the Bottom Water due to the fact that it is a compromise. The upper limit approach assures no negative values for  $\Delta(^4\text{He})$ , but does not take into account the flux of "air injected"  $\Delta\text{He}$  from the Intermediate Waters. What is necessary is a model such as described by Bieri (1971) and Craig and Weiss (1971) that is capable of determining the atmospheric component of He, but the difficulty encountered with this approach is that the saturation anomalies of at least three other gases must be determined in addition to helium (Craig and Weiss, *ibid*). As well, the model has not been tested, so that an additional saturation anomaly must be measured. Additionally, there is some doubt as to the applicability of the model in that it ignores mixing processes; and a model which does, entails the necessity of knowing even more saturation anomalies.

## (iii) Helium isotope ratio anomalies and primordial helium

Table 19 gives the average trends in the helium data as well. The  $\Delta(^4\text{He})$  values are calculated from Eq. (14). The values given for the Intermediate Water  $\delta(^3\text{He})$  are single values interpolated from the ratio anomaly curve at the depth of the salinity minimum (the Intermediate Water core). All other values are averages over the particular depth ranges.

The  $\Delta(^3\text{He})$  values are the percentage excesses (relative to solubility) of  $^3\text{He}$  due to non-atmospheric sources. It is defined as

$$\Delta(^3\text{He}) = [\delta(^3\text{He}) + (1-\alpha) \times 10^2 + \frac{\Delta\text{He}}{100} \delta(^3\text{He}) + \Delta(^4\text{He})] / \alpha \quad (15)$$

where  $\Delta(^3\text{He})$  is in percent, and all symbols have been defined previously. A derivation may be found in Appendix 1.

The estimated precision of the  $\Delta(^4\text{He})$  and  $\Delta(^3\text{He})$  values is 0.6%, but the accuracy of the estimates is limited to 1.5% due to the uncertainty in the non-atmospheric component. It is likely that the relative uncertainties are smaller.

The AAIW core shows a larger ratio anomaly at 50°S than at 30°S. To place the relative values in perspective,

it is perhaps better to examine the ratio anomaly relative to air equilibrated water.

$$\delta'(^3\text{He}) \equiv \delta(^3\text{He}) + (1-\alpha) \times 100\% \quad (4)$$

where  $\alpha$  is the solubility isotope fractionation factor, equal to 0.988 in the temperature range of interest (Weiss, 1970c). This gives  $\delta'(^3\text{He})$  values of 3.7 and 2.0% for the 50°S and 30°S stations respectively, consistent with Reid's (1965, 1973) picture of anticyclonic geostrophic circulation for this water mass. Furthermore, Clarke et al. (1969) measured a value of 1.5% for  $\delta(^3\text{He})$  at the Intermediate Water core at 31°S, 177°W. This corresponds to a  $\delta'(^3\text{He})$  of 2.7%, again consistent with circulation. The buildup of  $^3\text{He}$  in these waters is a result of a turbulent flux of  $^3\text{He}$  from the Deep Water, partly balanced by loss upward through the thermocline, and partly balanced by horizontal advection and diffusion. In situ decay of tritium will also contribute to the excess  $^3\text{He}$ , as observed in the AAIW of the Atlantic (Chapter 3), but it is not possible without tritium data to estimate the size of the effect. In any case, consideration of all the mechanisms leads to the unavoidable conclusion that  $\delta(^3\text{He})$  increases downstream in the AAIW.

In the Deep and Bottom Waters the ratio anomaly increases toward the equator, with a superposed north-south asymmetry similar to the saturation anomalies: larger

corresponding values in the north.

The most striking feature of the vertical distribution of  $\delta(^3\text{He})$  (Fig. 17) is the characteristic mid-depth maximum first described by Clarke et al. (1969, 1970). The maximum intensifies and deepens toward the equator, apparently shoaling upward to the poles, and becoming broader near the eastern boundary (see, Clarke et al., 1970). The general depth trend of the maximum parallels the Benthic Front of Craig et al. (1972), suggesting that the extremum may be the result of high lateral diffusivity and transport along the Front. The  $\delta(^3\text{He})$ -S relations (Fig. 21) suggest a Z-diffusion subrange between the Intermediate Water and the break in the  $\delta(^3\text{He})$ -S curve at 30°S and 16°N; also supporting this idea. The major difficulty with this interpretation is that the depth of the maximum lies above the depth of the Frontal zone as determined by Craig et al. (1972).

At 30°S, the  $\delta(^3\text{He})$  maximum coincides with the deep oxygen minimum. Since  $\delta(^3\text{He})$  is a conservative property (away from sources of injection), this suggests that the oxygen minimum may well be an advective-diffusive rather than a local in situ consumptive feature. That is, the oxygen extremum may be generated by transport southward of low-oxygen water between the relatively oxygen-rich Intermediate and Bottom Waters. This has been suggested by Reid (1973) on the basis of the oxygen-nutrient distributions

and geostrophic calculations. This interpretation would be at variance with the models of Warren (1973) and Craig (1971b). It would be rather presumptuous at this point to draw firm conclusions as to the validity of either approach, but it would be appropriate to suggest that further measurements with closer sample spacing would allow a decision to be made.

It would be useful at this point to examine the horizontal distribution of excess  $^3\text{He}$  ( $\Delta(^3\text{He})$ ) in the Deep and Bottom Waters of the Pacific using all the available data. First, however, it should be noted that the  $\Delta\text{Ne}$  values of Beg (1971) appear to be systematically low. To illustrate this, his  $\Delta\text{Ne}$  values for the SCAN (East Pacific Rise) Expedition are compared with earlier data in the same area.

TABLE 20

 $\Delta\text{Ne}$  COMPARISONS

Data Source	Average $\Delta\text{Ne}$ , %
Beg (1971)	3.6
Bieri and Koide (1972)	6.9
Craig et al. (1967)	6.3
Bieri et al. (1966)	6.6

Examination of Table 20 shows Beg's  $\Delta\text{Ne}$  data to be 3.0% lower than the average of other authors. His  $\Delta\text{He}$  values are slightly, but not significantly, larger than those of Bieri and Koide (1972). The relevant  $\Delta(^4\text{He})$  and  $\Delta(^3\text{He})$  values have been recalculated using Beg's original  $\Delta\text{He}$  and  $\delta(^3\text{He})$  values and corrected  $\Delta\text{Ne}$  values (Table 21).

Figure 23 shows the horizontal distribution of Deep and Bottom  $\Delta(^3\text{He})$  in the Pacific. The values exhibit a remarkable maximum over the East Pacific Rise. The dashed line roughly delineates the area associated with shallow seismicity, high heat flow and negative free-air gravity anomaly (after Langseth and Von Herzen, 1970); characteristics associated with upwelling mantle material. Beg (1971) came to the conclusion that primordial  $^3\text{He}$  was being injected from the East Pacific Rise Crest, and the overall pattern of Fig. 23 is supportive. The excess  $^3\text{He}$  generally decreases radially from the ridge, with evidence of advection superposed on the trend. The stations at  $50^\circ\text{S}$  and  $63^\circ\text{S}$  show the influence of the Circumpolar current with lower values than predicted from a radial (from the EPR) trend. The station at  $31^\circ\text{S}$ ,  $177^\circ\text{W}$  also has a lower value, indicating the Western Boundary current.

Because of the size of the systematic uncertainties in the saturation anomaly data reported previously (Beg, 1971; Bieri and Koide, 1972) it is unwise to attempt to draw conclusions by comparing different data sets for  $\Delta(^4\text{He})$ . In

TABLE 21

 $\Delta(^4\text{He})$  AND  $\Delta(^3\text{He})$  AVERAGES FROM THE DATA OF BEG (1971)

		NOVA EXP.	GEOSECS I	SCAN EXP.	
		31°S×177°W	28.5°N×121.6°W	6.5°S×107°W*	8.5°N×113°W
$\Delta(^4\text{He})$	Deep	1.0	4.3	7.9	6.1
	Bottom	1.3	3.9	5.0	0
	Deep and Bottom	1.2	4.1	6.5	3.1
$\Delta(^3\text{He})$	Deep	23.0	28.6	41.0	37.5
	Bottom	12.0	23.2	34.9	30.0
	Deep and Bottom	17.5	25.9	38.0	34.8

\* Average of three stations.

addition, because of the oversimplified nature of the model calculation for  $\Delta(^4\text{He})$ , it is difficult to draw quantitative conclusions from even one data set. It is, however, possible to discern a general increasing trend northward as would be expected for a diffuse, non-localized injection of  $^4\text{He}$  into the Bottom Water. This does not preclude localized injection as is indicated for  $^3\text{He}$ , because the effects are so marginal (as explained in Chapter 1) and the model so crude that nothing definitive can be said.

Considering the uncertainties involved in estimating the  $\Delta(^4\text{He})$  component of excess helium in sea water, the attempt by Beg (1971) to correlate  $\Delta(^4\text{He})$  with  $\delta(^3\text{He})$  was premature. First, it would have been more meaningful to attempt a correlation between  $\Delta(^3\text{He})$  and  $\Delta(^4\text{He})$  as  $\delta(^3\text{He})$  is to some extent dependent on the presence of non atmospheric  $^4\text{He}$ . Second, he quotes a linear correlation coefficient and claims a high probability of correlation, whereas a more meaningful test of the correlation would have been a chi-square. In fact, the scatter from the straight line fit far exceeds the experimental uncertainty, indicating that the model is a poor fit to reality.

In a broad sense, one can expect a correlation independent of the details of origin and mode of injection simply by assuming that the excess helium is injected into Deep and Bottom Waters. This can be explained by noting that the surface waters will be in equilibrium with the

atmosphere, and thus have  $\Delta(^4\text{He})$  and  $\Delta(^3\text{He}) \sim 0$ . The Intermediate Waters will be in diffusive equilibrium with both Deep and Surface Waters, and thus will have intermediate values of  $\Delta(^3\text{He})$  and  $\Delta(^4\text{He})$ . It can be seen, therefore, that the correlation will be generated by diffusion and mixing between two end members: the Deep and Bottom Waters and the Surface Waters

(iv) The helium flux

It is possible to estimate the upward diffusive-advective flux of  $^3\text{He}$  at two locations in the Pacific ( $30^\circ\text{S}$  and  $16^\circ\text{N}$ ). The applicability of the one-dimensional advective-diffusive model has been satisfactorily demonstrated by the linear relationship between  $\delta(^3\text{He})$  and salinity in the Deep Water range at the two stations (see Fig. 21, and Appendix 1). The advective-diffusive flux can be calculated by first fitting the data to

$$C(Z) = C_1 + C_2 e^{-Z/Z^*} \quad (16)$$

over the diffusive subrange.  $Z^*$  is the characteristic length, defined as the ratio of the vertical turbulent diffusivity  $D$  to the upwelling velocity  $w$ . The upward flux can then be calculated from

$$F = w C_1 \quad (17)$$

(derived in Appendix 1). In a formal sense, Eq. (17) entirely resembles a box model flux calculation, but, as explained in Appendix 1, the turbulent diffusive flux is included in the value of  $C_1$ . The values obtained for the parameters in Eq. (16) at 30°S and 16°N are given in Table 22. Since there were only three points in the depth range, a chi-square is not calculable, but a trial and error determination of the sensitivity of the parameters to

TABLE 22

## ONE-DIMENSIONAL ADVECTIVE-DIFFUSIVE MODEL PARAMETERS

Station	Z*	C <sub>1</sub>	C <sub>2</sub>	C <sub>1</sub> <sup>†</sup>	Flux
	(km)	(%)	(%)	(ccSTPg <sup>-1</sup> )	(Oceanic) (atoms cm <sup>-2</sup> sec <sup>-1</sup> )
234 (30°S)	0.5	24.2	-10.8	1.6×10 <sup>-14</sup>	7.0
243 (16°N)	1.2	29.4	-10.2	2.0×10 <sup>-14</sup>	8.8

† corrected for  $\Delta(^4\text{He})$

the data uncertainties gives an estimated error of  $\pm 15\%$ .

$C_1$  was converted to cc STPg<sup>-1</sup> using average helium concentrations and  $\Delta(^4\text{He})$ 's over the depth range, and using a  $^3\text{He}/^4\text{He}$  ratio of  $1.4 \times 10^{-6}$  for atmospheric helium (Mamyrin et al., 1970). The flux was calculated using an average potential density of 1.03 and an upwelling velocity

of  $5 \pm 2 \text{ m y}^{-1}$  (the latter as determined by Craig, 1969; Kuo and Veronis, 1973). Since the  $^3\text{He}$  is coming predominantly from the Mid-Oceanic Ridges, the Oceanic fluxes are not representative of the earth average, so assuming no  $^3\text{He}$  flux through the continents, fluxes of 5.0 and 6.3 atoms  $\text{cm}^{-2} \text{ sec}^{-1}$  are obtained for  $30^\circ\text{S}$  and  $16^\circ\text{N}$ . Since these values are not significantly different, an average value of  $5.6 \pm 0.6 \text{ atoms cm}^{-2} \text{ sec}^{-1}$  is obtained. To this must be added an uncertainty of 40% in the upwelling velocity.

In light of the nature of the  $\Delta(^4\text{He})$  data, the optimum estimate of the  $^4\text{He}$  Oceanic flux may be obtained from a box model calculation to be  $(8 \pm 3) \times 10^5 \text{ atoms cm}^{-2} \text{ sec}^{-1}$ .

Since  $^4\text{He}$  must be subject to the same transport mechanisms as  $^3\text{He}$ , it is reasonable to upgrade this result by assuming the same characteristic length,  $Z^*$  etc. This yields an average Oceanic flux of  $(1.1 \pm .5) \times 10^6 \text{ atoms cm}^{-2} \text{ sec}^{-1}$ . This value is somewhat higher than that of Craig and Clarke (1971) corresponding to their smaller estimate of  $\Delta(^4\text{He})$ . It would be unwise to attempt to extrapolate this flux to continental crust as the larger concentrations of uranium and thorium lead to a significant contribution from radiogenic helium.

The  $^3\text{He}/^4\text{He}$  ratio of the Oceanic flux is, therefore,  $(7 \pm 2) \times 10^{-6}$ . Mamyrin et al. (1972) reported a ratio of

0.8 to  $1.4 \times 10^{-5}$  for  $^3\text{He}/^4\text{He}$  in volcanic gases, a value somewhat higher than, but not in complete disagreement with, the value determined here.

Fluxes of  $^4\text{He}$  estimated from helium distribution in sediments (Clarke et al., 1973; Barnes, 1974) are generally two orders of magnitude lower than the fluxes determined here. In situ U and Th decay in the sediments can account for only  $\lesssim 5 \times 10^3$  atoms  $\text{cm}^{-2} \text{sec}^{-1}$  (Barnes, 1974). A tholeiitic oceanic crust 6 km thick, assuming U and Th concentrations of 0.1 and 0.2 ppm (Tatsumoto et al., 1965) would result in a  $^4\text{He}$  flux of  $2.7 \times 10^4$  atoms  $\text{cm}^{-2} \text{sec}^{-1}$ . The bulk of the helium production, therefore, cannot take place in the crust, but must come from the mantle. In addition, the flux is not distributed uniformly, but must be localized, much as is the flux of  $^3\text{He}$ .

## APPENDIX 1

### VARIOUS MATHEMATICAL DERIVATIONS

#### A. Two-Dimensional Fickian Diffusion from a Point Source in an Anisotropic Medium

Using a pseudo-Lagrangian frame of reference such that the x-z plane (which is perpendicular to the current velocity) advects downstream with the current, the conservation equation for a property C is

$$D \frac{\partial^2 C}{\partial z^2} + K \frac{\partial^2 C}{\partial x^2} = \frac{\partial C}{\partial t} \quad . \quad (\text{A.1})$$

where D and K are the vertical and lateral eddy diffusion coefficients respectively and z and x are the vertical (positive downward) and horizontal (positive eastward) spatial coordinates. D and K are assumed independent of spatial coordinates. Applying the initial condition that  $C = C_0 \delta(x-x_0, z-z_0)$  at  $t = 0$  and applying the boundary conditions that  $C = 0$  at  $x, z = \pm\infty$ , the solution to Eq. (A.1) is

$$C(x, z, t) = \frac{C_0}{4\pi t \sqrt{KD}} e^{-\left(\frac{x-x_0}{x^*}\right)^2} e^{-\left(\frac{z-z_0}{z^*}\right)^2} \quad (\text{A.2})$$

where  $x^* = 2\sqrt{Kt}$  and  $z^* = 2\sqrt{Dt}$ .

Determination of  $z^*$  at two stations gives

$$(z_2^*)^2 - (z_1^*)^2 = 4D(t_2 - t_1) = \frac{4D}{v} (d_2 - d_1) = 4 \frac{D}{v} \Delta d$$

or

$$\frac{D}{v} = [(z_2^*)^2 - (z_1^*)^2] / 4\Delta d \quad (\text{A.4})$$

where  $\Delta d$  is the distance and  $v$  is the average lateral velocity between the two stations.

#### B. The Flux Balance Model

In a stationary tongue-like distribution of property the vertical diffusive flux must be balanced by the lateral advective flux, giving

$$D \frac{\partial^2 C}{\partial z^2} - v \frac{\partial C}{\partial y} = 0 \quad . \quad (\text{B.1})$$

This gives

$$\frac{D}{v} = \left( \frac{\partial C}{\partial y} \right) / \left( \frac{\partial^2 C}{\partial z^2} \right) \quad . \quad (\text{B.2})$$

For a box-model, consisting of two reservoirs separated by a boundary layer of thickness  $d$ , the vertical derivative may be estimated as

$$\frac{\partial^2 C}{\partial z^2} = \frac{\Delta C}{dh}$$

where  $\Delta C$  is the concentration difference between the two reservoirs and  $h$  is the thickness of the reservoir in which  $\frac{\partial C}{\partial y}$  has been determined.

### C. Tritium-Helium Age Calculation

Tritium decays to  ${}^3\text{He}$  with a half life of 12.26 y according to

$$N({}^3\text{H}) = N_0({}^3\text{H})e^{-\lambda\tau}$$

The daughter product  ${}^3\text{He}$  accumulates as

$$\begin{aligned} N({}^3\text{He}) &= N_0({}^3\text{H}) - N({}^3\text{H}) \\ &= N({}^3\text{H})(1 - e^{-\lambda\tau}) \end{aligned}$$

Solving for  $\tau$  yields

$$\tau = 17.69 \log\left\{1 + \frac{N({}^3\text{He})}{N({}^3\text{H})}\right\} \quad (\text{C.1})$$

$N({}^3\text{He})$  can be expressed in terms of

$\delta'({}^3\text{He}) = \delta({}^3\text{He}) + (1-\alpha) \times 100$ ,  $C(\text{He})$ , and  $N({}^3\text{H})$  in terms

of T.U., (1 T.U. =  $10^{-18}$  T/H) , so Eq. (C.1) becomes

$$\tau = 17.69 \log\left\{1 + 5.42 \frac{\delta'(^3\text{He})}{T} C(\text{He}) \times 10^3\right\} \quad (\text{C.2})$$

where  $C(\text{He})$  is the helium concentration in cc STP/Kg,  $\delta'(^3\text{He})$  is in ‰ and  $T$  is the tritium concentration in T.U.. An average potential density of  $1.026 \text{ g cm}^{-3}$  is assumed. The uncertainty of an age calculation is

$$\Delta\tau = \frac{17.69}{1 + 1.83 \frac{T}{\delta'(^3\text{He})C(\text{He})} \times 10^{-4}} .$$

#### D. The One-Dimensional Advective Diffusive Model

Defining the spatial coordinate  $z$ , the advection velocity  $w$  and the flux  $F$  all positive downward, the flux is given by

$$F = - \rho D \frac{\partial C}{\partial z} + w\rho C$$

for a stable conservative property, where  $D$  is the vertical eddy diffusion coefficient, where  $C$  is the property concentration in units  $\text{Kg}^{-1}$ , and  $\rho$  is the fluid density (assumed constant). From continuity

$$\frac{\partial C}{\partial t} = - \frac{\partial F}{\partial z} = D\rho \frac{\partial^2 C}{\partial z^2} - w\rho \frac{\partial C}{\partial z}$$

or

$$D \frac{\partial^2 C}{\partial z^2} - w \frac{\partial C}{\partial z} = 0 \quad (D.2)$$

in the steady state, Eq. (D.2) has the general solution

$$C = C_1 + C_2 e^{-z/z^*} \quad (D.3a)$$

where  $z^*$  is the characteristic or scale length, defined by

$$z^* \equiv \frac{D}{w} \quad (D.3b)$$

Substituting Eq. (D.3) into Eq. (D.1) yields

$$F = w\rho C_1 \quad (D.4)$$

This equation formally resembles the box-model calculation of the flux

$$F_B = w\rho \bar{C} \quad (D.5)$$

where  $\bar{C}$  is the mean concentration. The difference lies in that  $C_1$  includes a contribution from the eddy diffusion flux, i.e.,

$$F_{AD} = F_B + F_D$$

where  $F_{AD}$  is the advective-diffusive flux (D.4) and  $F_D$  is the "diffusive component" or the difference between the advective-diffusive estimate and the box-model estimate. To examine this relation further, one can calculate (D.5) in terms of (D.3) over the depth range  $0 \leq z \leq z_M$ :

$$\begin{aligned} F_B &= w\rho\bar{C} = \frac{w\rho}{z_M} \int_0^{z_M} (C_1 + C_2 e^{-z/z^*}) dz \\ &= \frac{w\rho}{z_M} [C_1 z_M + z^* C_2 (1 - e^{-z_M/z^*})] \\ &= w\rho C_1 + \frac{D\rho C_2}{z_M} (1 - e^{-z_M/z^*}) \end{aligned}$$

hence

$$F_D = - \frac{D\rho C_2}{z_M} (1 - e^{-z_M/z^*}) \quad . \quad (D.6)$$

Since  $C_2$  is negative for  $w < 0$  (upward advection), it can be seen that the advective-diffusive model yields a larger flux than the box-model.

For two stable conservative tracers with the same eddy diffusion coefficients, one has

$$\left. \begin{aligned} \psi &= \psi_1 + \psi_2 e^{-z/z^*} \\ C &= C_1 + C_2 e^{-z/z^*} \end{aligned} \right\} \quad \text{and} \quad \text{(D.7)}$$

where  $\psi$  and  $C$  are the tracer concentrations. Manipulation of (D.7) to eliminate the  $z$ -dependence yields

$$\psi = \psi_1 + \psi_2 \frac{C - C_1}{C_2}$$

which is the equation of a straight line. Equation (D.8) states that for two stable conservative tracers, one is a linear function of the other over the diffusive sub-range.

#### E. Derivation of the Non-Atmospheric $^3\text{He}$ Component

The concentration of  $^3\text{He}$  and  $^4\text{He}$  may be expressed as the sum of three components, namely the solubility, atmospheric<sup>†</sup> and non-atmospheric components. That is,

$$C(^4\text{He}) = C_0(^4\text{He}) + C_A(^4\text{He}) + C_{NA}(^4\text{He})$$

and

$$C(^3\text{He}) = C_0(^3\text{He}) + C_A(^3\text{He}) + C_{NA}(^3\text{He}) \quad .$$

---

†

assumed air-injected.

Now

$$\Delta(^3\text{He}) \equiv 100 \times \frac{C_{\text{NA}}(^3\text{He})}{C_0(^3\text{He})} \quad (\text{E.1})$$

where  $\Delta(^3\text{He})$  is the percentage non-atmospheric component of  $^3\text{He}$ . But

$$\begin{aligned} C_{\text{NA}}(^3\text{He}) &= R_{\text{NA}} C_{\text{NA}}(^4\text{He}) \\ &= R_{\text{NA}} C_0(^4\text{He}) \frac{\Delta(^4\text{He})}{100} \\ &= \frac{R_{\text{NA}}}{R_{\text{A}}} \frac{\Delta(^4\text{He})}{100} C_0(^3\text{He}) \end{aligned} \quad (\text{E.2})$$

where  $\Delta(^4\text{He})$  is the percentage non-atmospheric component of  $^4\text{He}$ ,  $R_{\text{NA}}$  is the isotopic ratio of the non-atmospheric helium, viz

$$R_{\text{NA}} = \frac{C_{\text{NA}}(^3\text{He})}{C_{\text{NA}}(^4\text{He})} ,$$

and  $R_{\text{A}}$  is the atmospheric isotope ratio. The measured isotopic ratio is the average isotopic ratio of the three components weighted according to concentration, that is

$$R = \frac{\alpha R_{\text{A}} C_0(^4\text{He}) + R_{\text{A}} C_{\text{A}}(^4\text{He}) + R_{\text{NA}} C_{\text{NA}}(^4\text{He})}{C_0(^4\text{He}) + C_{\text{A}}(^4\text{He}) + C_{\text{NA}}(^4\text{He})} \quad (\text{E.3})$$

where  $R_{\text{A}}$  is the isotopic concentration of atmospheric

helium and  $\alpha$  is the solubility isotope fractionation factor.

Using the definitions

$$C_{NA}({}^4\text{He}) = \frac{\Delta({}^4\text{He})}{100} C_0({}^4\text{He})$$

$$C_A({}^4\text{He}) = \frac{\Delta^A\text{He}}{100} C_0({}^4\text{He}) .$$

Equation (E.3) becomes

$$R = \frac{\alpha R_A + R_A \Delta^A\text{He}/100 + R_{NA} \Delta({}^4\text{He})/100}{1 + \Delta^A\text{He}/100 + \Delta({}^4\text{He})/100} \quad (\text{E.4})$$

Expressing the measured ratio in terms of  $R_A$  and the ratio anomaly yields

$$(1 + \delta({}^3\text{He})/100) R_A + \frac{(\alpha R_A + R_A \Delta^A\text{He}/100 + R_{NA} \Delta({}^4\text{He})/100)}{1 + \Delta^A\text{He}/100 + \Delta({}^4\text{He})/100} .$$

Rearrangement gives

$$\frac{\Delta({}^4\text{He})}{100} \frac{R_{NA}}{R_A} = [100 + \Delta^A\text{He} + \Delta({}^4\text{He})] [1 + \delta({}^3\text{He})/100] - 100\alpha - \Delta^A\text{He} . \quad (\text{E.5})$$

Substituting (E.5) and (E.2) into (E.1) and noting that

$\Delta\text{He} = \Delta^A\text{He} + \Delta({}^4\text{He})$  yields

$$\Delta(^3\text{He}) = [\delta(^3\text{He}) + (1-\alpha) \times 10^2 + \frac{\Delta\text{He}}{100} \delta(^3\text{He})$$

$$+ \Delta(^4\text{He})] / \alpha \quad .$$

(E.6)

## APPENDIX 2

### GLOSSARY

#### A. Symbols and Terms

- $\alpha$  The helium solubility isotope fractionation factor; i.e., the ratio of the solubilities of the two helium isotopes =  $\frac{\beta(^3\text{He})}{\beta(^4\text{He})}$
- $\beta$  The bunsen solubility or reciprocal Henry's Law coefficient
- C The concentration of a property
- D The vertical turbulent diffusion coefficient in  $\text{cm}^2 \text{sec}^{-1}$
- $\delta(^3\text{He})$  The helium isotope ratio anomaly (in percent) relative to air
- $\delta'(^3\text{He})$  The helium isotope ratio anomaly (in percent) relative to air-equilibrated water  
=  $\delta(^3\text{He}) + (1-\alpha) \times 100$

- $\Delta\text{He}$  The helium saturation anomaly (in percent). The excess helium relative to the solubility equilibrium concentration at the potential temperature and salinity of the sample
- $\Delta\text{Ne}$  The neon saturation anomaly (in percent)
- $\Delta'\text{He}$  The excess helium =  $\Delta\text{He} - \Delta\text{Ne}$
- $\Delta(^3\text{He})$  The percentage nonatmospheric excess  $^3\text{He}$
- $\Delta(^4\text{He})$  The percentage nonatmospheric excess  $^4\text{He}$
- $f$  The air-injection fractionation factor =  $\frac{\Delta\text{He}}{\Delta\text{Ne}}$  for pure air injection
- $F$  The flux of a property
- $K$  The horizontal turbulent diffusion coefficient in  $\text{cm}^2 \text{sec}^{-1}$
- $R_i$  The Richardson number
- $\rho$  The potential density. The density after the sample has been adiabatically raised to the sea-surface

- S        The salinity in per mil
- T        The tritium concentration in T.U. (1 T.U. =  $10^{-18}$  T/H)  
at time of sampling
- $\tau$        The tritium-helium age, as calculated from the  
tritium concentration and the excess  $^3\text{He}$
- $\theta$        The potential temperature. The temperature after the  
sample has been adiabatically raised to the sea-  
surface
- v        The lateral (current) velocity
- w        The vertical upwelling velocity
- $x^*$       The horizontal characteristic or scale length
- $z^*$       The vertical characteristic or scale length

Tritiogenic

Produced by the decay of tritium

B. Acronyms

AABW	Antarctic Bottom Water
AAIW	Antarctic Intermediate Water
AIW	Arctic Intermediate Water
CPDW	Circumpolar Deep Water
CPIW	Circumpolar Intermediate Water
GEOSECS	Geochemical Ocean Sections Survey
LDW	Lower North Atlantic Deep Water
LSW	Labrador Sea Water
MDW	Middle North Atlantic Deep Water
MW	Mediterranean Water
NADW	North Atlantic Deep Water
NEADW	North-East Atlantic Deep Water (Iceland-Scotland Overflow Water)

NWABW North-West Atlantic Bottom Water  
(Denmark Strait Overflow Water)

PDW Pacific Deep Water

RSBW Ross Sea Bottom Water

SMW Subtropical Mode Water  
(Eighteen Degree Water)

UDW Upper North Atlantic Deep Water

WBC Western Boundary Contour

WBUC Western Boundary Undercurrent

#### REFERENCES

- Altimose, V. O. (1961) Helium diffusion through glass.  
J. App. Phys. 32, 1309
- Atkinson, L. P. (1973) Effect of air bubble solution on air-sea gas exchange. J. Geophys. Res. 78, 962
- Barkley, R. A. (1968) Oceanographic atlas of the Pacific Ocean. Univ. Hawaii Press (Honolulu) 156, Fig.
- Beaver, E. M. (1973) An automatic ratio readout system for a double collection Mass Spectrometer. Mass Spectroscopy 21, 37
- Beg, M. A. (1971) Helium isotope oceanography. Ph.D. Thesis (unpublished) McMaster Univ., Canada. 118 pp.
- Benson, B. B. (1965) Some thoughts on gases dissolved in the oceans. Mar. Geochem. Proc. Symp. 91
- Bieri, R. H. (1971) Dissolved noble gases in marine waters. Earth Planet. Sci. Letters 10, 329
- Bieri, R. H., and Koide, M. (1972) Dissolved noble gases in the East Equatorial and Southeast Pacific. J. Geophys. Res. 77, 1667
- Bieri, R. H., Koide, M., and Goldberg, E. D. (1964) Noble gases in seawater. Science 146, 1035
- Bieri, R. H., Koide, M., and Goldberg, E. D. (1966) The noble gas contents of Pacific seawater. J. Geophys. Res. 71, 5243

- Bieri, R. H., Koide, M., and Goldberg, E. D. (1967)  
Geophysical implications of the excess helium found  
in Pacific waters. *J. Geophys. Res.* 72, 2497
- Bieri, R. H., Koide, M., and Goldberg, E. D. (1968) Noble  
gas contents of marine waters. *Earth Planet. Sci.*  
*Letters* 4, 329
- Blanton, J. and Pattullo, J. G. (1970) The subsurface  
boundary between Subarctic Pacific Water and  
Pacific Equatorial Water in the transition zone off  
Southern California. *Limn. Oceanogr.* 15, 606
- Boerboom, A. J. H. and Kleyn, G. (1969) Diffusion  
coefficients of noble gases in water. *J. Chem.*  
*Phys.* 50, 1086
- Brewer, P. G., Spencer, D. W., and Robertson, D. E. (1972)  
Trace element profiles from the GEOSECS II Test  
Station in the Sargasso Sea. *Earth Planet. Sci.*  
*Letters* 16, 111
- Broecker, W. S. (1973) The 27.55 sigma-theta horizon in the  
Atlantic Ocean. (unpublished report) Columbia  
Univ. (New York)
- Callahan, J. E. (1972) The structure and circulation of  
deep water in the Antarctic. *Deep-Sea Res.* 19, 563
- Clarke, W. B., Beg, M. A., and Craig, H. (1969) Excess <sup>3</sup>He  
in the sea: evidence for terrestrial primordial  
helium. *Earth Planet. Sci. Letters* 6, 213

- Clarke, W. B., Beg, M. A., and Craig, H. (1970) Excess  $^3\text{He}$  at the North Pacific GEOSECS Station. J. Geophys. Res. 75, 7676
- Clarke, W. B., Horowitz, R. M., and Broecker, W. S. (1973) Interstitial water studies, Leg 15 - Inert gases. In "Initial reports of the Deep Sea Drilling Project", Vol. XX (Heezen, B.C. et al., Ed.) 777
- Corliss, J. B. (1971) The origin of metal bearing submarine hydrothermal solutions. J. Geophys. Res. 76, 8128
- Corsin, S. (1961) Turbulent flow. Amer. Scientist 49, 300
- Craig, H. (1969) Abyssal carbon and radiocarbon in the Pacific, J. Geophys. Res. 74, 5491
- Craig, H. (1971a) Son of abyssal carbon. J. Geophys. Res. 76, 5133 (Reply to Suess and Goldberg, 1971)
- Craig, H. (1971b) The deep metabolism: oxygen consumption in abyssal ocean water. J. Geophys. Res. 76, 5078
- Craig, H. (1973) Leg Report. GEOSECS Atlantic Leg V, (unpublished manuscript)
- Craig, H., Chung, Y., and Fiadero, M. (1972) A benthic front in the South Pacific. Earth Planet. Sci. Letters 16, 50
- Craig, H., and Clarke, W. B. (1970) Oceanic  $^3\text{He}$ : contribution from cosmogenic tritium. Earth Planet. Sci. Letters 9, 45
- Craig, H., and Lal, D. (1961) The production rate of natural tritium. Tellus XIII, 85

- Craig, H., and Weiss, R. F. (1971) Dissolved gas saturation anomalies and excess helium in the ocean. *Earth Planet. Sci. Letters* 10, 289
- Craig, H., Weiss, R. F., and Clarke, W. B. (1967) Dissolved gases in the Equatorial and South Pacific Oceans. *J. Geophys. Res.* 72, 6165
- Defant, A. (1961) *Physical oceanography*, Vol. 1. Pergamon Press (New York) 729 pp.
- Dockins, K. O., Bainbridge, A. E., Houtermans, J. C., and Suess, H. E. (1967) Tritium in the mixed layer of the North Pacific Ocean. In "Radioactive dating and methods of low level counting", IAEA (Vienna) 744 pp.
- Duedall, I. W., and Coote, A. R. (1972) Oxygen distribution in the Pacific Ocean. *J. Geophys. Res.* 77, 2201
- Edmond, J. M., Chung, Y., and Sclater, J. G. (1971) Pacific bottom water: penetration East around Hawaii. *J. Geophys. Res.* 76, 8089
- Eittrheim, S., and Ewing, M. (1972) Suspended particulate matter in the deep waters of the North American Basin. In "Studies in physical oceanography", Vol. 2 (Gordon, A. L., Ed.) Gordon and Breach (New York) 232 pp.
- Eriksson, E. (1965) An account of the major pulses of tritium and their effects in the atmosphere. *Tellus* XVII, 118

- Fairhall, A. W. (1969) Concerning the source of excess  $^3\text{He}$  in the sea. *Earth Planet. Sci. Letters* 7, 249
- Fleming, H. S., Cherkis, N. Z., and Heirtzler, J. R. (1970) The Gibbs Fracture Zone: a double fracture zone at  $52^{\circ}30'N$  in the Atlantic Ocean. *Mar. Geophys. Res.* 1, 37
- Girdler, R. W. (1966) Statistical analysis of terrestrial heat flow and seismicity of the Pacific Ocean. In "The crust and upper mantle of the Pacific area", (Kropof, L. et al., Ed.) A.G.U. Geophys. Mono. Ser. No. 12, 35
- Gordon, A. L. (1971a) Oceanography of Antarctic Waters. In "Antarctic Oceanology" (Reid, J. L., Ed.) Amer. Geophys. Union, 169
- Gordon, A. L. (1971b) Antarctic polar front zone. In "Antarctic Oceanology", (Reid, J. L., Ed.) Amer. Geophys. Union, 205
- Gordon, A. L. (1971c) Recent physical oceanographic studies of Antarctic waters. In "Research in the Antarctic", (Quam, L. O., Ed.)
- Gordon, A. L. (1972) Spreading of Antarctic bottom waters II. In "Studies in physical oceanography", Vol. 2 (Gordon, A. L., Ed.) Gordon and Breach (New York) 232 pp.
- Grant, A. B. (1968) Atlas of oceanographic sections. Report A.O.L. 68-5. Bedford, Canada

- Hintenberger, H., König, H., Schultz, L., and Suess, H. E.  
(1964) Krypton and xenon in the oceans. Z.  
Naturforschg. 19a, 1227
- Jenkins, W. J., Beg, M. A., Clarke, W. B., Wangersky, P. J.,  
and Craig, H. (1972) Excess  $^3\text{He}$  in the Atlantic  
Ocean. Earth Planet. Sci. Letters 16, 122
- Johnson, D. A. (1972) Eastward-flowing bottom currents along  
the Clipperton Fracture Zone. Deep-Sea Res. 19, 253
- Kamwisher, J. (1963) On the exchange of gases between the  
atmosphere and the sea. Deep-Sea Res. 10, 195
- Katz, E. J. (1970) Diffusion of the core of Mediterranean  
Water above the Mid-Atlantic Ridge Crest. Deep-Sea  
Res. 17, 611
- König, H. (1963) Über die Löslichkeit der Edelgase in  
Meerwasser. Z. Naturforschg. 18a, 363
- König, H., Wänke, H., Bien, G. S., Rakestraw, N. W., and  
Suess, H. E. (1964) Helium, neon and argon in the  
Oceans. Deep-Sea Res. 11, 243
- Kuo, H. H., and Veronis, G. (1970) Distribution of tracers  
in the deep oceans of the world. Deep-Sea Res. 17,  
29
- Kuo, H. H., and Veronis, G. (1973) The use of oxygen as a  
test for an abyssal circulation model. Deep-Sea Res.  
20, 871

- Langseth, M. G., and von Herzen, R. P. (1970) Heat flow the floor of the world oceans. In "The Sea", Vol. 4, Pt. 1 (Maxwell, A. E., Ed.)
- Lazier, J. R. N. (1973) The renewal of Labrador Sea Water. Deep-Sea Res. 20, 341
- Lee, A., and Ellet, D. (1967) On the water masses of the Northwest Atlantic Ocean. Deep-Sea Res. 14, 183
- Lister, C. R. B. (1972) On the thermal balance of a mid-ocean ridge. Geophys. J. R. astr. Soc. 26, 515
- Mamyrin, B. A., Anufriev, G. S., Kamensky, I. L., and Tolstyklm, I. N. (1970) Determination of the isotopic composition of helium in the atmosphere. Geochem. Int. 7, 498
- Mamyrin, B. A., Tolstyklm, I. N., Anufriev, G. S., and Kamensky, I. L. (1972) Helium isotopic composition in the thermal springs of Iceland. Geokhimiya 11, 1396
- Mann, C. R. (1969) Temperature and salinity characteristics of the Denmark Strait overflow. Deep-Sea Res. Supp. to 16, 125
- Mann, C. R., Coote, A. R., and Garner, D. M. (1973) The meridional distribution of silicate in the Western Atlantic Ocean. Deep-Sea Res. 20, 791
- Masuzawa, J. (1969) Subtropical Mode Water. Deep-Sea 16, 463

- Major, E., Wasserburg, G. J., and Craig, H. (1964) Rare gases in Pacific Ocean water. *Deep-Sea Res.* 11, 929
- McCoy, F. W., Jr. (1968) Bottom currents in the Western Atlantic Ocean between the Lesser Antilles and the Mid-Atlantic Ridge. *Deep-Sea Res.* 15, 179
- Medwin, H. (1970) In situ acoustic measurements of bubble population in coastal ocean waters. *J. Geophys. Res.* 75, 599
- Metcalf, W. G. (1969) Dissolved silicate in the deep North Atlantic. *Deep-Sea Res. Supp. to* 16, 139
- Michel, R., and Williams, P. M. (1973) Bomb-produced tritium in the Antarctic Ocean. *Earth Planet. Sci. Letters* 20, 381
- Munk, W. H. (1966) Abyssal recipes. *Deep-Sea Res.* 13, 707
- Neumann, G., and Pierson, W. J. (1966) Principles of physical oceanography. Prentice-Hall (Englewood Cliffs, New Jersey) 545 pp.
- NORPAC Committee (1960) Oceanic observations of the Pacific: 1955. NORPAC atlas. Univ. Calif (Berkeley) 120 pp.
- Norton, F. J. (1959) Gas permeation through the vacuum envelope. In "Trans. A.V.S. Natl. Vac. Symp." (1961) 8
- Östlund, H. G., Dorsey, G., and Rooth, C. (1974) North Atlantic GEOSECS radiocarbon and tritium data. Submitted to *Earth Planet. Sci. Letters* for publication

- Okubo, A. (1971) Horizontal and vertical mixing in the sea.  
In "Impingement of man on the oceans", (Hood, D., Ed.)  
Wiley-Interscience (New York)
- Pytkowicz, R. M., and Kester, D. R. (1966) Oxygen and  
phosphate as indicators for the deep intermediate  
waters in the north-east Pacific Ocean. Deep-Sea  
Res. 13, 373
- Reed, R. K. (1969) Deep water properties and flow in the  
Central North Pacific. J. Mar. Res. 27, 24
- Reid, J. L. (1965) Intermediate waters of the Pacific Ocean,  
The Johns Hopkins Oceanographic Studies, No. 2, The  
Johns Hopkins Press (Baltimore) 85 pp.
- Reid, J. L. (1973) TransPacific hydrographic sections at  
Lats. 43°S and 28°S: the SCORPIO Expedition III.  
Upper water and a note on southward flow at mid-  
depth. Deep-Sea Res. 20, 39
- Roether, W., and Münnich, K. O. (1972) Tritium profile at  
the Atlantic 1970 GEOSECS test cruise station.  
Earth Planet. Sci. Letters 16, 127
- Spencer, D. W. (1972) GEOSECS II, the 1970 North Atlantic  
Station: hydrographic features, oxygen and  
nutrients. Earth Planet. Sci. Letters 16, 91
- Spencer, D. W., Robertson, D. E., Turekian, K. K., and  
Folsom, T. R. (1970) Trace element calibrations and  
profiles at the GEOSECS Test Station in the North-  
east Pacific Ocean. J. Geophys. Res. 75, 7688

- Steele, J. H., Barrett, J. R., and Worthington, L. V. (1962) Deep currents south of Iceland. *Deep-Sea Res.* 9, 465
- Suess, H. E., and Goldberg, E. D. (1971) Comments on paper by Craig, H., "Abyssal carbon and radiocarbon in the Pacific". *J. Geophys. Res.* 76, 5131
- Swallow, J. C., and Worthington, L. V. (1969) Deep currents in the Labrador Sea. *Deep-Sea Res.* 16, 77
- Tatsumoto, M., Hedge, C. E., and Eugel, A. E. J. (1965) Potassium, rubidium, strontium, thorium, uranium, and the ratio of  $^{87}\text{Sr}/^{86}\text{Sr}$  in oceanic tholeiitic basalt. *Science* 150, 886
- Taylor, C. B. (1971) Influence of 1968 French thermonuclear tests on tritium fallout in the Southern Hemisphere. *Earth Planet. Sci. Letters* 10, 196
- Warren, B. A. (1972) The insensitivity of Subtropical Mode Water characteristics to meteorological fluctuations. *Deep-Sea Res.* 19, 1
- Warren, B. A. (1973) TransPacific hydrographic sections at Lats. 43°S and 28°S: the SCORPIO Expedition II. Deep water. *Deep-Sea Res.* 20, 9
- Weiss, R. F. (1968) Piggyback sampler for dissolved gas studies on sealed water samples. *Deep-Sea Res.* 15, 695

- Weiss, R. F. (1970a) Dissolved gases and total inorganic carbon in seawater: distribution, solubilities, and shipboard gas chromatography. Ph.D. Thesis (unpublished) Univ. Calif. (San Diego) 130 pp.
- Weiss, R. F. (1970b) The solubility of nitrogen, oxygen and argon in water and seawater. Deep-Sea Res. 17, 721
- Weiss, R. F. (1970c) Helium isotope effect in solution in water and seawater. Science 168, 247.
- Weiss, R. F. (1971) The solubility of helium and neon in water and seawater. J. Chem. Engg. Data 16, 235
- Wong, C. S. (1972) Deep zonal water masses in the Equatorial Pacific Ocean inferred from anomalous oceanographic properties. J. Geophys. Res. 77, 7196
- Worthington, L. V. (1959) The 18° water in the Sargasse Sea. Deep-Sea Res. 5, 297
- Worthington, L. V., and Volkmann, G. H. (1965) The volume transport of the Norwegian Sea Overflow Water in the North Atlantic Ocean. Deep-Sea Res. 12, 667
- Worthington, L. V., and Wright, W. R. (1970) North Atlantic oceanographic atlas, Woods Hole Oceanographic Inst. Atlas Series No. 2
- Wyrтки, K. (1962) The oxygen minima in relation to oceanic circulation. Deep-Sea Res. 9, 11.